Karlsruher Institut für Technologie

Pushing the Boundaries of Impedance and Nonlinearity in Superconducting Quantum Circuits Based on Granular Aluminum

Zur Erlangung des akademischen Grades einer

Doktorin der Naturwissenschaften (Dr. rer. nat.)

von der KIT-Fakultät für Physik des
Karlsruher Instituts für Technologie (KIT)

angenommene

Dissertation

von

M. Sc. Mahya Khorramshahi

Tag der mündlichen Prüfung:
25. Juli 2025

Referent:	Prof. Dr. Ioan Pop
Korreferentin:	Dr. habil. Claire Marrache-Kikuchi (University Paris Saclay, France)

Abstract

Superconducting circuits based on high kinetic inductance materials are promising candidates for future quantum technologies, owing to their magnetic field resilience, low microwave losses, and lithographic scalability. In this thesis, we explore the properties of granular aluminum (grAl) resonators in two distinct geometries, using the nonlinear kinetic inductance of grAl for applications in superconducting quantum circuits.

In the first part, we present compact meandered ring resonators fabricated using a single-step lift-off process. By optimizing film resistivity and geometry, we achieve superinductors with characteristic impedances exceeding 100 kΩ, corresponding to total inductance of several microhenries. These high-impedance devices exhibit internal quality factors on the order of 10^5 in the single-photon regime and frequency noise spectral densities as low as 200–1000 Hz/$\sqrt{\text{Hz}}$ at 10 Hz. These high-impedance resonators with large zero-point voltage fluctuations are suitable for coupling to molecular qubits, small electric dipoles, and spins in quantum dots, for studying quantum phase slips, and for implementing protected qubit designs.

In the second part, we investigate DC-tunable resonators based on a $3\lambda/4$ fractal geometry that allows direct current injection for in-situ tuning of the resonance frequency. We achieve frequency tunability up to 4.5% before reaching the critical current, and extract characteristic currents I^* ranging from 109 to 414 μA for resonators with sheet inductances between 41 and 92 pH/□. The nonlinear inductance is analyzed using theoretical models based on Ginzburg-Landau, Mattis-Bardeen-BCS, and a 1D Josephson junction array model. Noise and quality factor measurements indicate internal quality factors around 10^4, demonstrating the suitability of these resonators for use in broadband phase shifters, three-wave mixing parametric amplifiers, and other devices requiring tunable nonlinearity and frequency control.

This work establishes granular aluminum as a material for realizing high-impedance and frequency-tunable superconducting circuits, offering new opportunities for advanced applications in quantum information processing and hybrid quantum technologies.

Acknowledgements

Looking back on this journey, I feel deeply grateful for the many amazing people I had the chance to meet, work with, and learn from, and for all the experiences that shaped me along the way.

I would like to express my gratitude to my supervisor, Ioan Pop, for his motivating enthusiasm for science and for giving me the opportunity to become part of such an exciting field. Working in quantum technology exposed me to a remarkably diverse range of skills and perspectives, and this has been one of the most rewarding aspects of my PhD. I am also thankful for your support in polishing papers and preparing presentations.

I would also like to thank Thomas Reisinger for his feedback and for introducing me to different experimental techniques and tools.

One of the most memorable experiences of my PhD was the internship I spent at Low Noise Factory (LNF) in Gothenburg. For this, I am especially grateful to my supervisors there for their positive and encouraging attitude, the excellent collaboration, and the time we spent working together in the lab. David Niepce, I especially appreciate the long experimental days we shared, your generosity with your time, and your constant willingness to discuss ideas, results, and problems. Your kindness, patience, and calm way of approaching things were truly inspiring to me. Sumedh Mahashabde, thank you for sharing the office with me and for the many conversations we had throughout different stages of analysis and research. I learned a great deal from our exchanges, not only scientifically, but also from your thoughtful perspective on life more broadly. My sincere thanks also go to the entire LNF team for making me feel so welcome from the very beginning. Although I spent only a limited time with you, you always gave me the feeling that I was truly part of the group. I look back very fondly on the warm atmosphere, the shared lunches, and the grill gathering.

I gratefully acknowledge the support of the European Union's Horizon 2020 research and innovation programme QUSTEC under the Marie Sklodowska-Curie grant agreement, which provided the funding for my PhD. I also thank the wonderful people I met through this programme and during the summer schools and scientific events that accompanied this journey. In particular, I would like to mention Carlo Ciaccia, who joined our group for a short internship and brought a warm and positive spirit to the group, Ritika Dhundhwal, with whom I shared an office and many interesting conversations and moments, and Safa Lamia Ahmed, who was a very good friend to me from the very beginning.

I owe special thanks to Martin Spiecker. You were like a brother to many of us in the group. I have always admired your sharp mind, hard work, and genuine enthusiasm. What impressed me most was the creative way you approached problems and inspired me to search for solutions with a more flexible mindset. Beyond science, you were also inspiring in many aspects of life, including music and learning the piano.

I am deeply grateful to Patrick Paluch, one of those people every group is lucky to have. You are inspiring, humble, and truly easy to work with. It was always possible to come to you with any question, and I never hesitated to do so. I especially appreciated not only our many scientific discussions, but also your kindness and the way your presence could lift the mood during difficult times. I will always remember you as someone with a truly golden heart.

I would also like to thank Nicolas Gosling, Simon Geisert, Ameya Nambisan, Mitchell Field, and Nicolas Zapata for the good years of collaboration, friendship, and the respect they showed me. My thanks also go to Denis Bénâtre for helping with coding-related challenges, and to Dennis Rieger for his thoughtful advice. I am also grateful to Appu Sunil for being the best gym buddy ever, to Mario De Lucia for the collaboration on optical absorption in granular aluminum, and to the wider Black Forest Quantum group, including Patrick Winkel, Francesco Valenti, Mathieu Féchant, Simon Günzler, Sören Ihssen, Janic Beck, Philipp Lenhard, and Paul Kugler, for the interesting discussions and the inspiring atmosphere.

I would also like to thank Silvia Diewald and Simone Dehm for accompanying me through the long and winding path of fabrication, and Lukas Radtke, the cleanroom angel, for his reliable help in the cleanroom. Whenever something was missing, not working properly, or unexpectedly produced an error, you always seemed to appear at exactly the right moment and helped solve the issue with ease. I would also like to thank Martin Limbach for introducing me to the workshop devices at INT and for his help with technical matters.

Finally, I would like to express my deepest gratitude to my parents. No words can fully capture how much your endless love, trust, and support have meant to me over the years, and I feel incredibly lucky to have you by my side. You always believed in me, encouraged me, and taught me to stay strong and to move forward with integrity. To my brothers, thank you for always being there for me. Whenever I felt tired, overwhelmed, or far from home, you made time for me no matter where you were or how busy life was. After every long conversation with you, I somehow found myself again and could continue with renewed strength. Your warmth, humor, and steady support carried me through more moments than you probably know.

Contents

List of Publications

[1] **M. Khorramshahi**, M. Spiecker, P. Paluch, S. Geisert, N. Gosling, N. Zapata, L. Brauch, C. Kübel, S. Dehm, R. Krupke, W. Wernsdorfer, I. M. Pop, and T. Reisinger, "High Impedance Granular Aluminum Ring Resonators", Phys. Rev. Appl. **24**, 024066 (2025).

[2] M. De Lucia, **M. Khorramshahi**, T. Reisinger, I. M. Pop, and G. Ulbricht, "Measurement of Optical Absorption in Granular Aluminum Thin Films at Room Temperature", Appl. Phys. B **131**, 157 (2025).

List of Figures

List of Tables

1 Introduction

This chapter introduces the foundational concepts and key components of superconducting quantum circuits. Starting from lumped-element LC resonators, we outline their quantum behavior as harmonic oscillators, including discrete energy quantization, characteristic impedance, and quality factors. We then introduce the Josephson junction (JJ) as a nonlinear, non-dissipative circuit element, discussing its key physical properties and role in enabling superconducting qubits. The chapter concludes with an overview of kinetic inductance and its circuit implications, with particular attention to granular aluminum (grAl) as a high-inductance superconducting material used throughout this work.

1.1 Motivation for Quantum Circuit Engineering

Since ancient times, humans have been fascinated by the workings of the universe. Whether staring at the stars or trying to understand the structure of atoms, we have tried to uncover the fundamental laws that describe the natural world. This philosophical curiosity sparked a scientific revolution in the 20th century, the development of quantum mechanics. Emerging in response to experimental results that conflicted with classical explanations, quantum mechanics introduced a fundamentally new way to understand nature at the microscopic scale, where classical intuition breaks down. Now, as we step into the era of the second quantum revolution, we are not just observing quantum phenomena; we are beginning to control them. This control opens up a wide array of technological possibilities, especially in areas like quantum sensing, quantum simulation, and quantum computing, fields that promise to change modern science, industry, and information processing.

To put this new understanding of quantum mechanics into practice, scientists have developed technologies that make use of quantum mechanics' most important features, like superposition and entanglement. One of the most foundational elements of these technologies is the quantum bit, or qubit, which acts as the basic unit of quantum information.

Unlike a classical bit, which exists in one of two definite states (0 or 1), a qubit can occupy a coherent superposition of both states, described by

$$|\Psi\rangle = \alpha|0\rangle + \beta|1\rangle, \quad \text{with} \quad |\alpha|^2 + |\beta|^2 = 1, \tag{1.1}$$

where α and β are complex probability amplitudes. This superposition enables quantum systems to encode and process information in ways that classical systems cannot.

When multiple qubits are involved, entanglement becomes possible. An entangled state looks as follows

$$|\Psi\rangle = \frac{1}{\sqrt{2}}(|00\ldots0\rangle + |11\ldots1\rangle) \tag{1.2}$$

This phenomenon gives rise to a Hilbert space that grows exponentially with the number of qubits, forming the basis for powerful quantum algorithms with no classical counterparts.

However, this power comes with some challenges. Qubits must maintain coherence over time, get manipulated with high fidelity, and be read out accurately, all while being isolated from environmental noise. To address these demands, the DiVincenzo criteria [3] define the essential features a quantum system must fulfill for scalable quantum computation: initialization, long coherence times, universal gate sets, reliable readout, and connection between qubits.

As the number of qubits increases, so does the susceptibility to errors, requiring robust quantum error correction techniques. These protocols use redundancy to encode logical qubits using several physical qubits, effectively preserving quantum information over longer timescales.

Various physical systems are used to implement qubits, each offering distinct advantages in terms of coherence, control, and scalability. These include microscopic systems such as trapped ions [4–6], nitrogen-vacancy centers in diamond [7], individual electron spins in semiconductors [8–10], and molecular spin systems [11–13]. On the other hand, macroscopic systems like superconducting circuits [14–18] are widely favored for their lithographic scalability and compatibility with microwave control techniques. These circuits are typically well-controlled, large-scale structures with gate and measurement fidelities that approach the thresholds required for quantum error correction.

Superconductors are particularly well suited for quantum computing applications due to their unique electrical and magnetic properties. When cooled below a material-specific

critical temperature T_c, superconductors enter a phase characterized by zero electrical resistance and the expulsion of magnetic fields from their interior, a phenomenon known as the Meissner effect.

These macroscopic quantum behaviors originate from the formation of Cooper pairs, which are pairs of bound electrons that move in a collective, phase-coherent state without energy dissipation. This coherent state allows the flow of steady currents and the quantization of magnetic flux in discrete multiples of the flux quantum, $\Phi_0 = h/2e$, where h is Planck's constant and e is the elementary charge. A key feature of the superconducting state is the emergence of an energy gap Δ in the spectrum. This gap protects the superconductor from excitations smaller than Δ [19, 20]. The internal magnetic field within a superconductor decays exponentially from the surface, following $B(x) = B_0 \exp(-x/\lambda_L)$, where λ_L is the London penetration depth. These properties provide the fundamental physical basis for a wide range of superconducting quantum devices.

To make superconducting circuits practical for quantum computing, engineers have developed strategies to mitigate noise and energy loss, such as cooling devices to millikelvin temperatures, applying magnetic and infrared shielding. These innovations have enabled superconducting qubits to approach the fidelity thresholds required for quantum error correction, making them strong candidates for scalable quantum processors. However, despite this progress, superconducting circuits continue to face key challenges. Energy losses from material defects, quasiparticles, and environmental noise still impose significant limits on qubit coherence and overall system performance.

There is a growing focus on building hybrid quantum systems that bring together different types of quantum hardware. The goal is to make use of each system's strengths while reducing its weaknesses. Although improving single platforms is still important, combining them offers a more flexible and powerful approach to advancing quantum technology. In this work, we focus on building high-impedance circuit elements, which have large zero-point voltage fluctuations. This enables stronger coupling to systems with small electric dipole moments, making our approach especially valuable for hybrid quantum applications. Additionally, using high-impedance components allows for the design of qubits that are less sensitive to flux noise, offering an advantage over conventional qubit architectures. We will explain this work in detail in Chapter 2.

Achieving a high signal-to-noise ratio (SNR) is essential in quantum measurement setups, as it directly improves readout fidelity and speed. While Josephson parametric amplifiers (JPAs) can operate near the quantum limit of added noise, they are limited by narrow bandwidth, small power dynamic range, and design complexity. As we will discuss the details in Chapter 3, we investigate the tunability of granular aluminum, a high-kinetic

inductance material. Thanks to its lithography compatibility and current-dependent kinetic inductance, grAl is a promising material for implementing traveling wave parametric amplifiers (TWPAs) and phase shifters. A grAl-based TWPA can potentially offer higher bandwidth and larger power dynamic range compared to Josephson junction-based designs, making it an attractive platform for quantum-limited amplifiers.

1.2 Superconducting Quantum Circuits

Superconducting quantum circuits are designed electrical systems that exhibit quantum mechanical properties even at macroscopic scales. These systems are built from circuits that include both linear elements, such as inductors and capacitors, and nonlinear elements, most commonly Josephson junctions. The classical properties of the circuits can be precisely modeled using finite element methods (FEM). We can fabricate them using common approaches such as thin-film deposition and lithographic techniques for patterning, enabling control over device parameters and reproducibility across circuits.

What makes superconducting quantum circuits notable is that they use flux and charge as quantum variables. These are observable macroscopic quantities, yet they are quantized and follow the laws of quantum mechanics. This allows superconducting circuits, though made from billions of atoms, to reliably store and manipulate coherent quantum states, enabling a leading platform for quantum information processing.

These circuits can be viewed from multiple perspectives [21].

- The solid-state physics viewpoint: they describe the collective motion of Cooper pairs in a superconducting condensate.
- An electrical engineering perspective: they reduce to effective circuit models from Kirchhoff's laws and a small set of quantum degrees of freedom.
- A quantum optics view: they resemble microwave cavities with discrete photonic modes.

Superconducting quantum circuits enable accurate simulation of a wide variety of quantum systems. By adjusting the circuit layout and the way components are designed and coupled, they facilitate exploring diverse physical behaviors under controlled conditions.

1.2.1 The Harmonic Oscillator

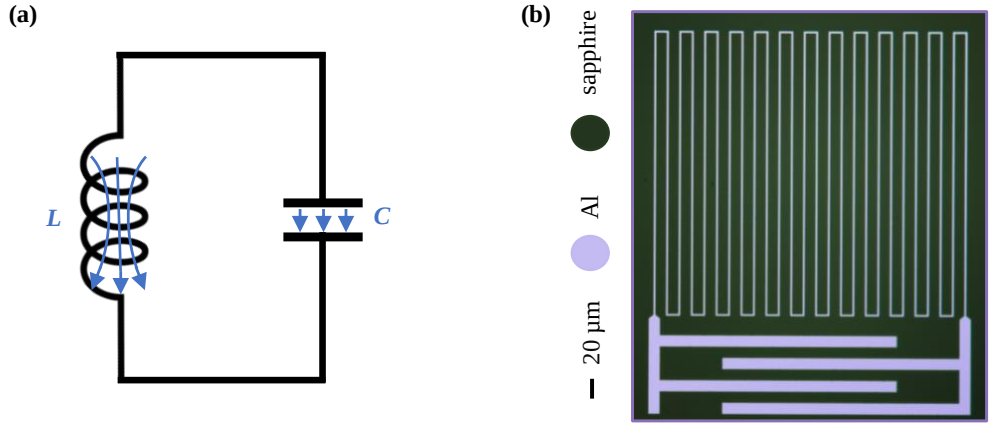

Figure 1.1: Lumped-Element Superconducting Resonator. (a) Schematic of the lumped-element LC resonator circuit, which shows an idealized circuit representation, highlighting the magnetic flux threading the inductor and electric field between the capacitor plates. The resonance occurs at the natural frequency $\omega_0 = 1/\sqrt{LC}$. (b) False-color optical microscopy image of a fabricated aluminum resonator on a sapphire substrate. The structure is defined using a single-step electron-beam lithography and lift-off process. The inductor is implemented as a meandered wire (top part), while the capacitor consists of an interdigitated structure (bottom part). This resonator with a simple fabrication approach provides a convenient platform for characterizing resonators and comparing loss mechanisms across different fabrication methods or measurement environments.

Resonators are important components in quantum circuits, being used as energy storage elements, filters, coupling buses, and quantum memories. They are designed to support standing wave patterns at specific resonant frequencies, where energy oscillates between electric and magnetic fields. At these resonant points, the stored electric energy in a capacitor equals the magnetic energy in an inductor. This angular frequency ω_0 of the resonance is given by

$$\omega_0 = \frac{1}{\sqrt{LC}}. \tag{1.3}$$

A basic LC circuit (see Fig. 1.1(a)), consisting of an inductor L and a capacitor C, behaves as a harmonic oscillator. When quantized, this system exhibits discrete energy levels

$$E_n = \hbar\omega_0 \left(n + \frac{1}{2}\right), \quad n = 0, 1, 2, \ldots \tag{1.4}$$

These evenly spaced levels define the Fock space and enable the resonator to store energy or help with qubit interactions [22].

In the quantum regime, classical variables like voltage and current become operators. The node flux $\hat{\Phi}$ and node charge $\hat{Q}$ are conjugate variables and obey the canonical commutation relation [23, 24]

$$[\hat{\Phi}, \hat{Q}] = i\hbar. \tag{1.5}$$

Using Faraday's law, the voltage is defined as the time derivative of flux

$$V(t) = \frac{d\Phi}{dt} = \dot{\Phi}. \tag{1.6}$$

The quantum Hamiltonian of the LC oscillator is

$$\hat{H} = \frac{\hat{Q}^2}{2C} + \frac{\hat{\Phi}^2}{2L}. \tag{1.7}$$

We can also write the Hamiltonian in terms of raising ($\hat{a}^\dagger$) and lowering ($\hat{a}$) operators

$$\hat{H} = \hbar\omega_0 \left(\hat{a}^\dagger \hat{a} + \frac{1}{2}\right), \tag{1.8}$$

where,

$$\hat{a} = \frac{1}{\sqrt{2\hbar Z}}\hat{\Phi} + i\sqrt{\frac{Z}{2\hbar}}\hat{Q}, \quad \hat{a}^\dagger = \frac{1}{\sqrt{2\hbar Z}}\hat{\Phi} - i\sqrt{\frac{Z}{2\hbar}}\hat{Q}, \tag{1.9}$$

and

$$Z = \sqrt{\frac{L}{C}} \tag{1.10}$$

is the characteristic impedance of the resonator. These operators satisfy the commutation relation

$$[\hat{a}, \hat{a}^\dagger] = 1. \tag{1.11}$$

The operators for flux and charge can be written as

$$\hat{\Phi} = \Phi_{\mathrm{ZPF}}(\hat{a} + \hat{a}^{\dagger}), \quad \hat{Q} = -iQ_{\mathrm{ZPF}}(\hat{a} - \hat{a}^{\dagger}), \tag{1.12}$$

with zero-point fluctuations

$$\Phi_{\mathrm{ZPF}} = \sqrt{\frac{\hbar Z}{2}}, \quad Q_{\mathrm{ZPF}} = \sqrt{\frac{\hbar}{2Z}}. \tag{1.13}$$

These quantify the vacuum uncertainties of the system's ground state

$$\langle 0|\hat{\Phi}^2|0\rangle = \Phi_{\mathrm{ZPF}}^2, \quad \langle 0|\hat{Q}^2|0\rangle = Q_{\mathrm{ZPF}}^2. \tag{1.14}$$

To characterize how efficiently a resonator stores energy relative to its losses, we use the quality factor Q, a key parameter that determines resonator performance in both classical and quantum systems

$$Q = \omega_0 \cdot \frac{\text{Average Stored Energy}}{\text{Average Power Loss}}. \tag{1.15}$$

In an ideal, lossless quantum system, energy would be preserved indefinitely, and the quality factor would be infinite. However, real resonators experience dissipation from both internal and external sources. The internal quality factor Q_{i} accounts for intrinsic losses such as dielectric, conductive, and radiative losses, while the external (or coupling) quality factor Q_{c} captures losses due to coupling to measurement lines or other circuit components. The total or loaded quality factor Q_{l} is given by [25, 26]

$$\frac{1}{Q_{\mathrm{l}}} = \frac{1}{Q_{\mathrm{i}}} + \frac{1}{Q_{\mathrm{c}}}. \tag{1.16}$$

The coupling regimes can be distinguished:

- Overcoupled ($Q_{\mathrm{c}} < Q_{\mathrm{i}}$): Fast energy transfer, typically desirable for readout applications.
- Undercoupled ($Q_{\mathrm{c}} > Q_{\mathrm{i}}$): Lower energy leakage, optimal for energy storage, coherence.
- Critically coupled ($Q_{\mathrm{c}} = Q_{\mathrm{i}}$).

In the context of our devices, Q_{i} is especially important, as it limits coherence and determines the suitability for quantum applications. We therefore extract and analyze Q_{i} for our resonators in the next chapters.

1.2.2 The Josephson Junction

The Josephson junction (JJ) is a fundamental component in superconducting quantum circuits, as a non-dissipative, nonlinear element, introduced by Brian Josephson in 1962 [27]. A JJ consists of two superconductors separated by a weak link, which allows for the tunneling of Cooper pairs without resistance. The nature of this weak link defines the type of JJ [28–39] (all types are shown in Fig. 1.2):

- S-I-S (Superconductor–Insulator–Superconductor): where the current tunnels through a thin insulating layer.
- S-c-S (Superconductor–Constriction–Superconductor): where the weak link is a narrow constriction in a continuous superconducting material.
- S-N-S (Superconductor–Normal metal–Superconductor): where a normal metal barrier shows induced superconductivity through the proximity effect.
- S-I-N-I-S (Superconductor–Insulator–Normal metal–Insulator–Superconductor): where a normal metal island is tunnel-coupled to superconductors through insulating barriers; commonly used in thermometry.
- S-F-S (Superconductor–Ferromagnet–Superconductor): where a thin ferromagnetic layer sits between two superconductors; these junctions can exhibit π-phase shifts.

In all these configurations, current flows through the junction due to a phase difference ϕ between the wavefunctions of the two superconductors. This gives rise to the DC Josephson effect, described by [28, 40, 41]

$$I = I_c \sin(\phi), \tag{1.17}$$

where I_c is the critical current, the maximum supercurrent that can pass through the junction without a voltage drop. Having a voltage drop V across the junction leads to a time-varying phase according to the second Josephson relation [28]

$$\frac{d\phi}{dt} = \frac{2eV}{\hbar}, \tag{1.18}$$

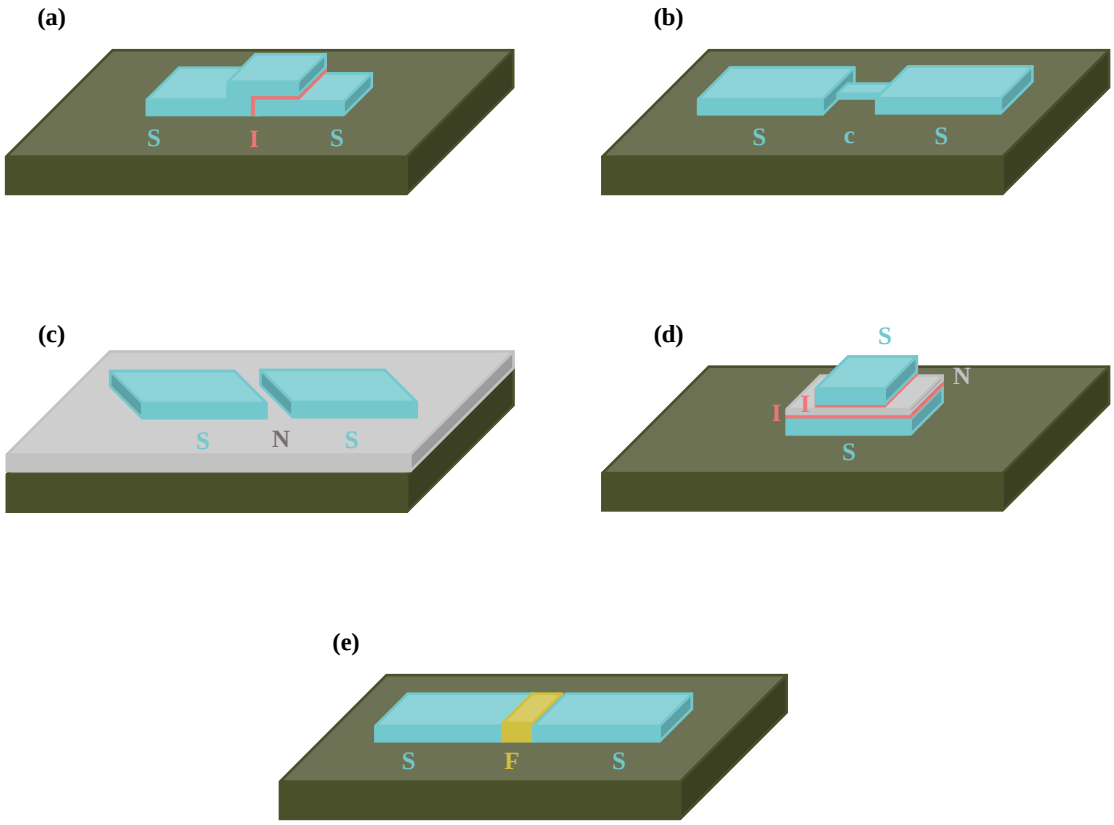

Figure 1.2: Types of Josephson Junctions. (a) Schematic of a Superconductor–Insulator–Superconductor (SIS) junction, where tunneling occurs through a thin insulating barrier, a widely used configuration in superconducting qubits. (b) Superconductor–Constriction–Superconductor (ScS) junction, in which a narrow geometric constriction serves as the weak link. (c) Superconductor–Normal metal–Superconductor (SNS) junction that uses proximity-induced superconductivity in the normal-metal region to mediate Cooper pair tunneling. (d) Superconductor–Insulator–Normal metal–Insulator–Superconductor (SINIS) junction, a double-barrier structure commonly used in low-temperature thermometry. (e) Superconductor–Ferromagnet–Superconductor (SFS) junction, which can introduce π-phase shifts used in memory and quantum logic applications. All configurations support non-dissipative Cooper pair transport, but differ in their microscopic mechanisms and fabrication techniques, offering distinct functionalities in superconducting quantum circuits.

where $2e$ is the charge of a Cooper pair and $\hbar$ is the reduced Planck constant. As a result, an AC supercurrent with frequency

$$\nu = \frac{2eV}{h} \tag{1.19}$$

flows across the junction.

The Josephson Potential

Beyond their unique tunneling behavior, Josephson junctions introduce nonlinear, dissipationless inductance to quantum circuits, a property that enables the transformation of harmonic circuits into artificial atoms [42]. The Josephson energy potential is [28, 43]

$$E = -E_{\mathrm{J}} \cos(\phi), \tag{1.20}$$

where $E_{\mathrm{J}} = \hbar I_{\mathrm{c}}/(2e)$ is the Josephson energy. For small phase variations $\phi \ll 1$, the potential can be expanded as

$$E \approx -E_{\mathrm{J}} + \frac{E_{\mathrm{J}}}{2}\phi^2 - \frac{E_{\mathrm{J}}}{24}\phi^4 + O(\phi^6). \tag{1.21}$$

The quadratic term corresponds to a linear inductor with Josephson inductance

$$L_{\mathrm{J}} = \frac{\Phi_0}{2\pi I_{\mathrm{c}}}, \tag{1.22}$$

where $\Phi_0 = h/2e$ is the magnetic flux quantum. The presence of the quartic and higher-order terms is the signature of anharmonicity in the Josephson potential, making the Josephson junction a source of nonlinearity in superconducting circuits even in the case of small excitations. Unlike harmonic oscillators (e.g., LC circuits with a linear inductor L), for which energy levels are equally spaced (see previous section), the cosine-shaped Josephson potential results in unevenly spaced energy levels. This spectral structure allows for isolated two-level systems, or qubits, where transitions between the two energy levels can be selectively controlled.

Phase Dynamics and the RCSJ Model

The RCSJ model is a widely used equivalent circuit to describe the realistic behavior of a biased Josephson junction. It models the JJ as a parallel combination of an ideal Josephson element, a resistor R, and a capacitor C [44, 45]. In Chapter 3, we use this model to describe the relation between kinetic inductance and bias current in granular aluminum, which can be modeled as a one-dimensional array of Josephson junctions. The differential equation for the phase ϕ is

$$C\left(\frac{\Phi_0}{2\pi}\right)\frac{d^2\phi}{dt^2} + \left(\frac{1}{R}\right)\left(\frac{\Phi_0}{2\pi}\right)\frac{d\phi}{dt} + I_{\mathrm{c}} \sin(\phi) = I, \tag{1.23}$$

where the second-order term represents inertial effects (like mass in mechanics), the first-order term accounts for damping (similar to friction), and I is the applied current.

This equation is analogous to the motion of a particle in a tilted washboard potential

$$U(\phi) = -E_{\mathrm{J}} \left[\cos(\phi) + \frac{I}{I_{\mathrm{c}}} \phi \right], \tag{1.24}$$

where the phase behaves like the position of a particle. In this analogy, the cosine term gives the periodic, washboard shape, while the linear term $\left(\frac{I}{I_{\mathrm{c}}}\right) \phi$ introduces a tilt, representing the effect of the applied current. A higher bias current increases the tilt, making it easier for the phase particle to escape potential wells. Depending on the current bias and damping, the particle either oscillates in a potential well (zero-voltage state) or slides downhill (finite-voltage state).

Damping Regimes in Josephson Dynamics

The quality factor $Q = \omega_p / \omega_{RC}$, where $\omega_p = \sqrt{2\pi I_c / (\Phi_0 C)}$ and $\omega_{RC} = 1/RC$, determines the damping behavior:

- Overdamped junctions ($Q < 1$) [46]: The phase particle has little inertia and is quickly trapped in a potential minimum when the bias current drops below I_{c}. Voltage returns to zero immediately, and no hysteresis in the current–voltage (I–V) characteristics is observed.
- Underdamped junctions ($Q > 1$) [47]: The phase retains momentum and can overshoot potential minima. This dynamic leads to hysteresis in the I–V curve. The return current I_{R} (when voltage goes to zero) is lower than the switching current I_{sw}, at which the junction switches to the voltage state.

The choice of damping regime depends on the intended application [48–52]. Underdamped junctions are preferred in qubits, quantum sensing, and low-energy photon detection [53]. Overdamped junctions are used in quantum metrology [54] when non-hysteretic behavior is required.

1.3 High Impedance Resonators

In electrical circuits, the impedance Z represents the frequency-dependent opposition to AC flow. It is given by

$$Z = R + iX, \tag{1.25}$$

where R is the resistance (real part, dissipates energy as heat) and X is the reactance (imaginary part, stores energy in electric or magnetic fields).

There are two types of reactance:

Capacitive reactance (X_C)

$$X_C = -\frac{1}{\omega C} \tag{1.26}$$

decreases with increasing frequency.

Inductive reactance (X_L)

$$X_L = \omega L \tag{1.27}$$

increases with frequency.

So, in a circuit with an inductor and a capacitor, the total impedance is

$$Z = R + i\left(\omega L - \frac{1}{\omega C}\right). \tag{1.28}$$

In circuits with high characteristic impedance Z_C, zero-point voltage fluctuations are enhanced [55, 56],

$$V_\mathrm{ZPF} \propto \sqrt{Z_\mathrm{C}}, \tag{1.29}$$

enabling coupling of superconducting microwave devices to other solid-state excitations, e.g., phonons via direct piezoelectric coupling [57] or parametric electromechanical interactions [58], or molecular qubits [59]. At the high end of Z_C, inductors with zero DC resistance and impedance exceeding the resistance quantum,

$$Z_\mathrm{C} > R_\mathrm{Q} = \frac{h}{(2e)^2} \approx 6.45\,\mathrm{k\Omega}, \tag{1.30}$$

are known as superinductors [60, 61]. They enable the realization of protected qubit architectures, such as fluxonium [62–68] and $0-\pi$ qubits [69–71], by delocalizing the wavefunction and mitigating flux noise. The high inductive reactance of superinductors is also essential for studying flux-tunneling-induced phase slips, facilitating the observation of dual Shapiro steps [72–74].

Long Josephson junction arrays are a widely used option for achieving high impedance with low loss [60, 61], and their impedance can exceed hundreds of kΩ when suspended in vacuum [75, 76]. However, these arrays—particularly in suspended configurations—are complex to fabricate and introduce unwanted nonlinearity [77]. Alternatively, geometric inductors optimized into suspended spiral shapes offer high linearity but remain challenging to fabricate [78, 79].

An ideal superinductor technology would combine low dissipation, straightforward fabrication, and compatibility across diverse operational environments, including high magnetic fields, as required in spin [56], Andreev [80], or nanowire qubit devices [81–83].

Disordered superconductors are a promising platform for realizing compact, high-impedance resonators, as discussed next.

1.4 Disordered Superconductors

Disordered superconductors can be realized by disturbing perfect crystalline structures through the introduction of defects such as vacancies, dislocations, impurities, and other irregularities. These imperfections break lattice periodicity and enhance electron scattering rates, thereby changing transport properties.

Disordered materials such as NbN [77, 84, 85], TiN [86–88], NbTiN [89–91], InO [92, 93], and granular aluminum [64, 94–97] have high kinetic inductance and are discussed in detail in the following section. These materials enter the local dirty limit regime of superconductors [98]

$$l \ll \xi_0 \ll \lambda_L, \tag{1.31}$$

where l is the electron mean free path, ξ_0 the Bardeen–Cooper–Schrieffer (BCS) coherence length, and λ_L the London penetration depth.

As disorder increases and the Ioffe-Regel condition [99] is approached, defined by the criterion $k_F \ell \approx 1$, where k_F is the Fermi wavevector and ℓ the mean free path—electronic states begin to localize, signaling the onset of a metal-insulator transition.

Another threshold was discovered by Dynes [100], showing that superconductivity in thin films breaks when the sheet resistance exceeds $\approx 30\,\mathrm{k\Omega}$.

Considering these limits and knowing the microscopic structures of disordered superconductors, one can refine the fabrication process to maximize kinetic inductance while maintaining superconducting behavior, enabling high-impedance device architectures.

1.5 Kinetic Inductance

Kinetic inductance comes from the inertia of charge carriers. Unlike geometric inductance, which results from magnetic fields generated by current loops, kinetic inductance originates from the kinetic energy stored in the motion of the superconducting charge carriers themselves.

To describe kinetic inductance, several theoretical models can be used. The Drude model explains conductivity in normal metals. The two-fluid model adds superconducting behavior by combining normal and superfluid carriers. The Mattis-Bardeen theory gives a full quantum description, especially useful for disordered superconductors at low temperatures. The London theory connects inductance to magnetic field penetration.

1.5.1 Drude and Two-Fluid Models

The kinetic inductance can be derived by analyzing the inductive component of the material's complex conductivity.

Drude Model: A Starting Point for Normal Metals

The Drude model [101] describes electrical transport in normal metals by treating electrons as a classical gas of non-interacting particles that respond to an applied electric field E. Electrons accelerate under the field but are randomly scattered after an average time τ. As a result, they gain an average momentum in the direction of the field.

The frequency-dependent complex conductivity is

$$\sigma(\omega) = \frac{ne^2\tau}{m_\mathrm{e}(1 + i\omega\tau)}, \tag{1.32}$$

where n, e, m_e and ω describe the electron density, the elementary charge, the electron mass, and the angular frequency, respectively.

Splitting this into real and imaginary parts leads to

$$\sigma_1 = \frac{ne^2\tau}{m_e(1+\omega^2\tau^2)}, \quad \sigma_2 = \frac{ne^2\omega\tau^2}{m_e(1+\omega^2\tau^2)}. \tag{1.33}$$

Here, σ_1 accounts for resistive losses, while σ_2 corresponds to the inductive (reactive) response. In normal metals, σ_2 is typically small, especially at microwave frequencies, and thus kinetic inductance is usually negligible.

Two-Fluid Model: Extending to Superconductors [102, 103]

Below the critical temperature, the two-fluid model assumes that conduction electrons divide into two populations:

- Superconducting electrons n_s, electrons forming Cooper pairs, which move without resistance.
- Normal electrons n_n (quasiparticles), which still experience scattering.

The total complex conductivity is the sum of both contributions

$$\sigma(\omega) = \sigma_s(\omega) + \sigma_n(\omega). \tag{1.34}$$

The normal part follows the Drude form. For the superconducting part, since Cooper pairs do not scatter, we take the limit $\tau \to \infty$ in the Drude expression. This leads to

$$\sigma_s = -i\frac{n_s e^2}{\omega m_e}, \tag{1.35}$$

this purely imaginary conductivity corresponds to an inductive response associated with kinetic inductance, as it shows the system stores energy in the motion of the superconducting carriers.

We can relate this to the kinetic inductance

$$L_k = \frac{m_e}{n_s e^2} \cdot \frac{l}{A}, \tag{1.36}$$

where l is the length and A the cross-sectional area of the superconductor. Note that for a superconductor, n_s depends on temperature and current.

Temperature Dependence

In the historical two-fluid model, the temperature dependence of the superfluid fraction, where $n = n_s + n_n$ is the total conduction-electron density, is given by

$$\frac{n_s}{n} = 1 - \left(\frac{T}{T_c}\right)^4 . \tag{1.37}$$

This means n_s decreases with rising temperature, increasing the kinetic inductance. However, in the modern view based on BCS theory, the temperature dependence is determined by the superconducting energy gap. As the temperature approaches zero, the density of normal electrons vanishes exponentially.

The Drude model covers basic transport physics in normal metals but does not include quantum effects or superconductivity. In addition, the two-fluid model adds the superconducting response and provides a simple framework to derive kinetic inductance. However, both models are limited. They ignore microscopic mechanisms giving rise to superconductivity. They do not account for the energy gap, coherence length, or non-local interactions. To accurately describe real superconductors, especially at low temperatures and in disordered systems, a quantum mechanical model such as the Mattis-Bardeen theory is required.

1.5.2 Mattis-Bardeen Formalism

To go beyond semi-classical descriptions, the Mattis-Bardeen formalism [104] offers a quantum mechanical model based on BCS theory. It provides a precise way to calculate the frequency-dependent complex conductivity of superconductors

$$\sigma(\omega) = \sigma_1(\omega) - i\sigma_2(\omega), \tag{1.38}$$

where the real part σ_1 corresponds to dissipative losses from quasiparticles, and the imaginary part σ_2 relates to the inductive (non-dissipative) response, i.e., kinetic inductance.

The conductivity is normalized to the normal-state conductivity σ_n, and expressed through energy integrals involving the superconducting energy gap Δ and Fermi-Dirac distribution $f(E)$

$$\frac{\sigma_1}{\sigma_n} = \frac{2}{\hbar\omega}\int_{\Delta}^{\infty}[f(E)-f(E+\hbar\omega)]\frac{E^2+\Delta^2+\hbar\omega E}{\sqrt{E^2-\Delta^2}\sqrt{(E+\hbar\omega)^2-\Delta^2}}\,dE + \frac{1}{\hbar\omega}\int_{\Delta-\hbar\omega}^{-\Delta}[1-2f(E+\hbar\omega)]\frac{E^2+\Delta^2+\hbar\omega E}{\sqrt{E^2-\Delta^2}\sqrt{(E+\hbar\omega)^2-\Delta^2}}\,dE \tag{1.39}$$

$$\frac{\sigma_2}{\sigma_n} = \frac{1}{\hbar\omega}\int_{\Delta-\hbar\omega,-\Delta}^{\Delta}[1-2f(E+\hbar\omega)]\frac{E^2+\Delta^2+\hbar\omega E}{\sqrt{\Delta^2-E^2}\sqrt{(E+\hbar\omega)^2-\Delta^2}}\,dE. \tag{1.40}$$

Low-Temperature Limit and Kinetic Inductance

At low temperatures and low frequencies ($\hbar\omega \ll 2\Delta$), the imaginary conductivity can be approximated by

$$\frac{\sigma_2}{\sigma_n} = \frac{\pi\Delta}{\hbar\omega}\tanh\left(\frac{\Delta}{2k_BT}\right). \tag{1.41}$$

This leads to the expression for kinetic inductance

$$L_k = \frac{l}{A}\cdot\frac{\rho\hbar}{\pi\Delta}\cdot\frac{1}{\tanh(\Delta/2k_BT)}. \tag{1.42}$$

In the limit $T \to 0$

$$L_k = \frac{\hbar}{\pi\Delta_0}R_n. \tag{1.43}$$

This equation is particularly relevant to the central aim of this thesis, maximizing inductance in superconducting resonators. It shows that in disordered superconductors, where the normal-state resistance R_n is large, the kinetic inductance can be significantly enhanced.

1.5.3 London Theory

While the Drude and two-fluid models offer useful approximations and the Mattis-Bardeen formalism provides a detailed quantum mechanical framework, it is sometimes desirable to use a simpler yet physically insightful model, the London theory, to capture the macroscopic electrodynamics of superconductivity.

The London Equations

The London model supplements Maxwell's equations to describe the behavior of electric and magnetic fields in superconductors. It introduces two core equations [105]:

$$\frac{\partial \vec{j}_\mathrm{s}}{\partial t} = \frac{n_\mathrm{s} e^2}{m_\mathrm{e}} \vec{E} \quad \text{(first London equation)} \tag{1.44}$$

$$\nabla \times \vec{j}_\mathrm{s} = -\frac{n_\mathrm{s} e^2}{m_\mathrm{e}} \vec{B} \quad \text{(second London equation)} \tag{1.45}$$

The first London equation implies a frictionless response of the supercurrent to an electric field, while the second describes the magnetic field screening in the superconductor (Meissner effect). From these, one can define the London penetration depth [28]

$$\lambda_L = \sqrt{\frac{m_\mathrm{e}}{\mu_0 n_\mathrm{s} e^2}}. \tag{1.46}$$

This is the characteristic length scale over which magnetic fields decay inside the superconductor.

Deriving Kinetic Inductance from London Theory

We can derive the expression for kinetic inductance by starting from the first London equation. For a uniform supercurrent density j_s, we get

$$\vec{E} = \frac{m_\mathrm{e}}{n_\mathrm{s} e^2} \frac{d\vec{j}_\mathrm{s}}{dt}, \tag{1.47}$$

assuming the total current is $I = j_\mathrm{s} A$ and the voltage drop is $V = El$, we obtain

$$V = \frac{m_\mathrm{e}}{n_\mathrm{s} e^2} \cdot \frac{l}{A} \cdot \frac{dI}{dt} \tag{1.48}$$

Comparing this with $V = L_\mathrm{k} \frac{dI}{dt}$, we identify the kinetic inductance as

$$L_\mathrm{k} = \frac{m_\mathrm{e}}{n_\mathrm{s} e^2} \cdot \frac{l}{A}, \tag{1.49}$$

using the definition of λ_L, we substitute

$$\frac{m_\mathrm{e}}{n_\mathrm{s} e^2} = \mu_0 \lambda_L^2 \tag{1.50}$$

This yields the widely used form

$$L_\mathrm{k} = \mu_0 \lambda_L^2 \cdot \frac{l}{A}. \tag{1.51}$$

This shows that kinetic inductance is determined by the superconductor's geometry and the London penetration depth. It increases with length l, increases with weaker superfluid density (larger λ_L), and decreases with larger cross-sectional area A.

1.6 Granular Aluminum

Granular aluminum is a disordered superconductor that can be a strong candidate for making superinductors, thanks to the high kinetic inductance that can be achieved with it. In this material, the Al metallic grains are separated by oxide barriers (Fig. 1.3(a), the image is provided by L. Brauch and C. Kübel), which can effectively be modeled as a 3D network of Josephson junctions [106] (Fig. 1.3(b)). The fabrication of grAl films involves evaporating pure Al in a controlled oxygen atmosphere. Two critical parameters determine the microstructure and electronic properties of the resulting film: the partial pressure of oxygen in the deposition chamber and the evaporation rate of Al. Adjusting these parameters allows for tuning of the film's normal-state resistivity. As oxygen pressure increases, the oxide barriers between grains thicken on average, leading to weaker intergrain coupling and higher resistivity.

For $\rho > 100\ \mu\Omega \cdot$ cm, the Al grains are typically around 3 ± 1 nm in diameter. However, the grain size is not constant and can vary depending on the substrate temperature during the deposition process. Lower substrate temperatures, such as those achieved by cooling with liquid nitrogen, result in smaller Al grains. The critical temperature is also influenced by the substrate temperature during deposition. Films evaporated onto cold substrates, typically at or below 100 K, have been shown to reach critical temperatures of $T_\mathrm{c} \geq 3$ K [107]. In contrast, films deposited at room temperature exhibit a lower T_c, generally around 2.2 K. Although both T_c values are still larger than that of pure Al films ($T_\mathrm{c} \sim 1.4$ K).

A notable feature of grAl is the dome-shaped dependence of the critical temperature on the normal-state resistivity. The peak typically occurs in the range of $\rho = 100$ to $1000\ \mu\Omega \cdot$ cm [108]. Ref. [97] demonstrated that grAl-based resonators made with ~ 90 nm

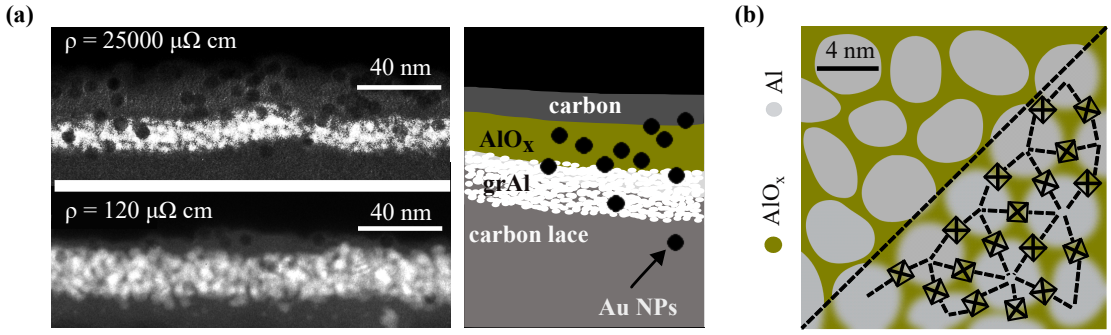

Figure 1.3: Granular Aluminum. (a) Energy-filtered transmission electron microscopy images of high-resistivity grAl (top, ≈ 25 000 μΩ cm) and low-resistivity grAl (bottom, ≈ 120 μΩ cm). The energy filter at 15 eV highlights the aluminum volume plasmon. The viewing angle is tilted by 72° to the deposition direction for both images. The right-hand schematic is there to aid interpretation of the images. The grAl was deposited on carbon laces visible at the bottom of the films. The dark particles are gold nanoparticles (Au NPs) introduced as fiducial markers for tracking the sample during rotation in tomography experiments. (b) Schematic of granular aluminum, illustrating aluminum grains (gray) encircled by aluminum oxide barriers. This microscopic configuration forms an effective array of Josephson junctions, which gives high kinetic inductance and tunable nonlinearity.

thick films can achieve exceptionally low loss, with internal quality factors reaching 10^6 in the single-photon regime, highlighting the material's suitability for quantum circuits when optimized in the appropriate resistivity range.

Circuit quantum electrodynamics (cQED) can be used to describe the quantum behavior of granular aluminum devices, assuming that the zero-point phase fluctuations between adjacent grains are small, allowing the system to be treated as weakly nonlinear. These assumptions lead to a Hamiltonian describing the nonlinear behavior of grAl-based resonant systems:

$$\frac{\hat{H}}{\hbar} = \sum_{n=1} \left(\omega_n + K_{nn}\hat{a}_n^\dagger \hat{a}_n\right) \hat{a}_n^\dagger \hat{a}_n + \sum_{n,m=1;\, n\neq m} \frac{K_{nm}}{2} \hat{a}_n^\dagger \hat{a}_n \hat{a}_m^\dagger \hat{a}_m, \tag{1.52}$$

where: ω_n are mode frequencies, K_{nn} are self-Kerr coefficients (frequency shift per photon in mode n), K_{nm} are cross-Kerr coefficients (interaction between different modes), $\hat{a}_n$, $\hat{a}_n^\dagger$ are bosonic lowering and raising operators, and $\hat{a}_n^\dagger \hat{a}_n = \hat{N}_n$ is photon number operator.

The nonlinearity of a strip of granular aluminum can be described using a simplified model that treats the structure as a one-dimensional (1D) array of effective Josephson junctions. The strip is divided into superconducting sections of length a, width w, and thickness t, so that each section has volume awt. The total number of junctions is $N = \ell/a$, where ℓ is

the total strip length. By solving the equations of motion and expanding the Josephson potential to third order, the self-Kerr and cross-Kerr coefficients for the fundamental mode are derived as [106]

$$K_{1n} = C\pi e a \frac{\omega_1 \omega_n}{j_c V_{\mathrm{grAl}}}, \quad \text{with } n \geq 1. \tag{1.53}$$

The self-Kerr coefficient K_{11} scales inversely with the volume V_{grAl} of the element through which the current passes, and the critical current density j_c. Thus, at fixed frequency and material parameters, shrinking the volume of the grAl element directly enhances nonlinearity. This principle allows one to tailor K_{11} for various applications:

- Superinductors [64, 95] & microwave kinetic inductance detectors (MKIDs) [109]: require minimal nonlinearity ($K_{11} \sim 10 - 100\,\mathrm{Hz}$)
- Parametric amplifiers [110–113] & converters: operate in the kHz range of Kerr nonlinearity
- Transmon qubits [114]: benefit from large nonlinearities ($K_{11} \sim 10 - 100\,\mathrm{MHz}$)

The kinetic inductance L_{k} of a superconducting strip of width w and length ℓ is given by

$$L_{\mathrm{k}} = L_{\mathrm{k}}^{\square} \frac{\ell}{w} = \frac{\hbar R_{\mathrm{n}}^{\square}}{C k_{\mathrm{B}} T_{\mathrm{c}} \pi} \cdot \frac{\ell}{w}, \tag{1.54}$$

where $L_{\mathrm{k}}^{\square}$ is the kinetic inductance per square, k_{B} is the Boltzmann constant, T_{c} is the superconducting critical temperature, and $R_{\mathrm{n}}^{\square}$ is the normal-state sheet resistance. The superconducting gap is linked to the critical temperature by $\Delta(0) = C k_{\mathrm{B}} T_{\mathrm{c}}$, with $C = 1.76$ for grAl resistivity below 2 mΩ·cm and up to $C \approx 2.1$ for the high-resistivity range.

High and tunable kinetic inductance, combined with internal quality factors up to 10^6 in the single-photon regime, makes grAl a good material for applications requiring high impedance and minimal loss. Its nonlinearity can be tuned through geometry and resistivity, allowing integration into both linear and nonlinear quantum devices. Moreover, its resilience against magnetic fields, with $Q_{\mathrm{i}} > 10^5$ maintained under in-plane fields up to 1 T [115], makes it a good candidate to be used for hybrid quantum systems and other circuits that need to be operated in a magnetic field. These attributes make grAl a good candidate for use in superinductors, kinetic inductance detectors, parametric amplifiers, and superconducting qubits.

2 High Impedance Ring Resonators

In this chapter, we present the main results, including the design, simulation, fabrication, and characterization of high-impedance granular aluminum (grAl) ring resonators. The large kinetic inductance of grAl is utilized to implement ring superinductors with meandered traces, achieving impedance levels well above 100 kΩ in the 4–8 GHz range. These resonators are integrated into a coplanar waveguide (CPW) architecture, optimizing coupling and enabling efficient experimental characterization. This chapter concludes with a characterization of resonators' performance. The results reveal quality factors exceeding 10^5 in the single-photon regime, nonlinearity on the order of tens of Hz, and frequency noise spectral densities ranging from 10^2 to 10^3 Hz/$\sqrt{\text{Hz}}$ at 10 Hz.

2.1 Introduction

Superconducting circuits with high characteristic impedance Z_C enhance zero-point voltage fluctuations ($V_{ZPF} \propto \sqrt{Z_C}$) [55, 56], enabling strong coupling to various quantum systems with small electric dipoles. When the impedance exceeds the resistance quantum $R_Q = h/(2e)^2 \approx 6.45$ kΩ, these circuit elements are referred to as superinductors [60, 61]. Superinductors play a key role in implementing noise-protected qubits [62–71], thanks to their reduced sensitivity to flux noise. Moreover, their large inductive reactance facilitates the study of quantum phase slips and flux tunneling phenomena [72–74].

Compared to long Josephson junction arrays, disordered superconductors are more fabrication-friendly and can be densely patterned using standard lithographic techniques, while offering high kinetic inductance that dominates the total inductive response.

Several disordered superconductors have demonstrated $Z_C > 1$ kΩ and internal quality factors $Q_i > 10^5$ in the single-photon regime, including NbN [77, 84, 85], TiN [86–88], NbTiN [89–91], NbAlN [116], and granular aluminum (grAl) [64, 94–97]. These materials also offer tunable self-Kerr nonlinearities: from 10 Hz to 10^5 Hz for NbN [77, 112] and

TiN [117], and from 10^{-2} Hz up to 10^{6} Hz for grAl [106, 114]. Notably, a recent comparative study [118] between NbN and grAl shows: while NbN excels in magnetic-field resilience, making it suitable for hybrid circuit QED platforms, grAl is better optimized for low-field applications requiring ultra-high impedance and strong nonlinearity.

This chapter focuses on the implementation and characterization of grAl-based resonators and their application in pushing the frontiers of high-impedance superconducting quantum circuits. We begin with an overview of the design and simulation of meandered grAl resonators, followed by a discussion of fabrication techniques. We then present experimental characterization of the resonator impedance, introduce a model to optimize impedance with respect to resistivity and geometry, and compare model predictions with measurements. The performance of the devices, internal quality factors, and frequency noise will also be analyzed. Finally, we conclude with simulations that suggest design parameters for achieving even higher impedance circuits for future implementations.

2.2 Design Considerations

2.2.1 Meandered Trace Ring Design

As discussed in the introductory chapter, grAl is a nanocomposite consisting of Al grains embedded in an aluminum oxide matrix, forming a self-assembled three-dimensional network of Josephson junctions (see Fig. 1.3(b)). It exhibits superconductivity over a broad range of normal-state resistivities ρ spanning from 1 to 10 000 $\mu\Omega \cdot$ cm [108]. The resistivity can be adjusted by varying the oxygen partial pressure during deposition of grAl, enabling control over the kinetic inductance L_k. This tunability allows the realization of inductors dominated by kinetic inductance with a kinetic inductance fraction $\alpha = L_\mathrm{k}/(L_\mathrm{k} + L_\mathrm{g})$ approaching unity, where L_g represents the geometric inductance.

To achieve high characteristic impedance, the resonator design must be optimized to minimize stray capacitance and maximize the number of squares in the kinetic inductance trace. This can be realized using a meandered ring resonator (see Fig. 2.1(a)), where the capacitance is reduced by decreasing the outer radius of the ring (r_out) and selecting the smallest possible meander pitch p. The number of squares in the kinetic inductance trace increases with the length ℓ and decreases with the width w of the resonator. Additionally, the kinetic inductance increases with the sheet resistance $R_\mathrm{n}^{\square}$, which can be controlled by using higher-resistivity films or reducing the film thickness.

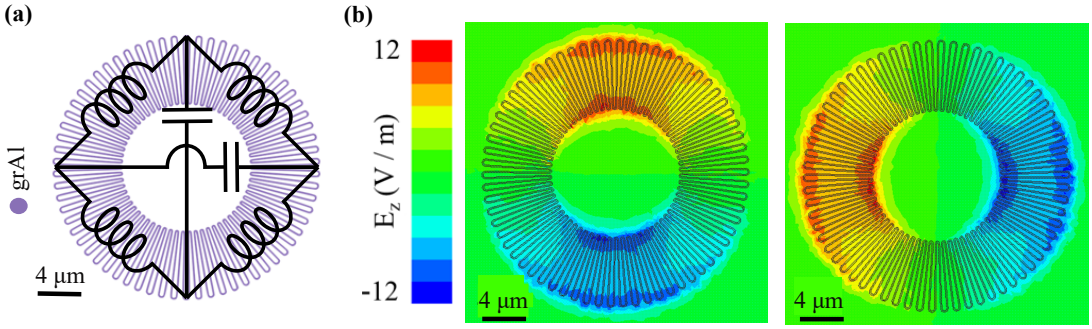

Figure 2.1: Granular Aluminum Ring Resonators Design. (a) Design of the ring resonator and its equivalent circuit. The densely packed meander trace maximizes the ratio of inductance to self-capacitance. The resonator's symmetric design results in two degenerate modes, each involving one effective capacitor shunted by two parallel inductors. (b) Rendering of the electric field distribution to illustrate the charge distribution within the resonator. The modes are similar to dual modes in aluminum ring resonators in Ref. [119].

As shown in Fig. 2.1(b), when the ring is closed, the symmetric design of this distributed resonator gives rise to two fundamental modes. The effective circuit model for each mode consists of a capacitor shunted by two parallel inductors with total inductance of $L/4$, L represents the total inductance of the ring. The degeneracy of these modes can be lifted by modifying the external coupling, introducing a gap to break the symmetry of the design.

2.2.2 Ring Resonators in Coplanar Waveguide Architecture

The resonators are capacitively coupled to a shared 50 Ω CPW for reflection measurements, as depicted in Fig. 2.2. The entire structure is enclosed within a silver ground plane, which helps suppress parasitic modes and maintain a uniform magnetic field across the chip. In addition, it might help in reducing the density of non-equilibrium quasiparticles by acting as a phonon trap [120, 121]. To minimize dissipation, the ground plane near the ends of each CPW is shifted away from the central pin. Close to the resonators, the ground plane consists of narrow superconducting lines connected to the normal conducting plane, effectively preventing the formation of superconducting loops that could trap magnetic flux.

The configuration of the CPW feed line allows for flexible coupling to the small rings, intentionally breaking the symmetry and lifting the degeneracy of the two fundamental modes. Positioning the ring near the semicircular structure at the end of the feed line (see

Fig. 2.2(c)) results in strong coupling for both modes, while placing it within the square structure at the center of Fig. 2.2(b) leads to asymmetric coupling of the modes to the feed line. The compact design accommodates three separate CPW sets on a single chip, each isolated by the ground plane, enabling the measurement of multiple ring resonators with different design parameters.

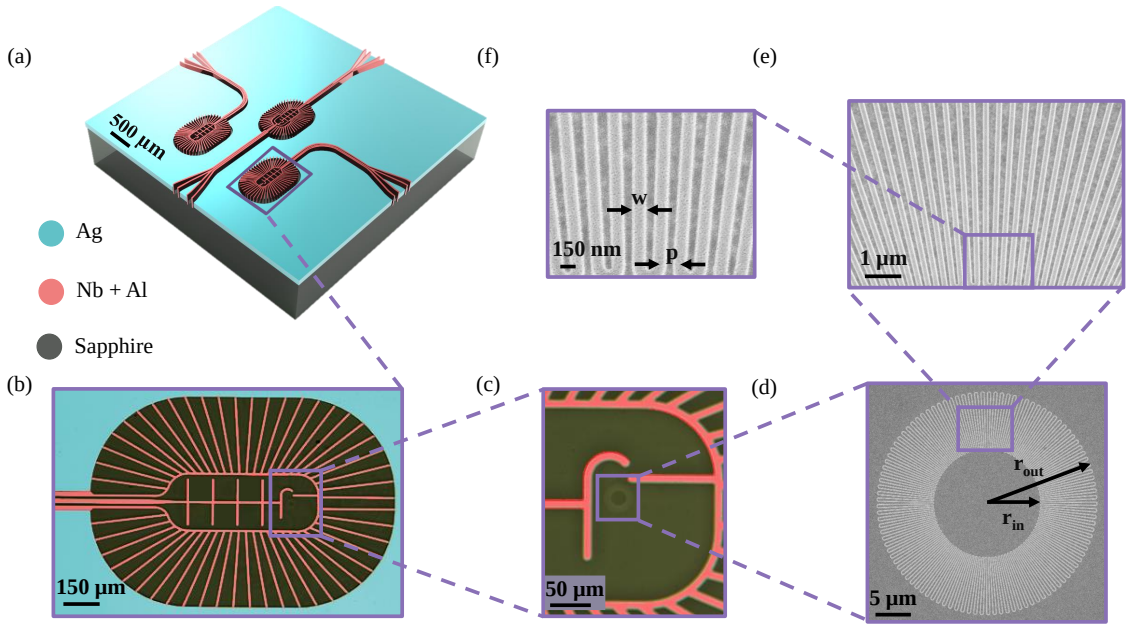

Figure 2.2: Ring Resonators in CPW Architecture. (a) Three-dimensional rendering of the chip layout on a sapphire substrate featuring multiple CPWs, enabling the measurement of various devices, and a surrounding ground plane to suppress parasitic modes and ensure a uniform magnetic field. The ground plane mostly consists of silver, which avoids flux trapping and damps microwave slot modes and phonons [120]. The central line of the CPW and the regions close to it consist of thin films of 15 nm niobium capped by 5 nm of aluminum. The 5 nm Al capping layer is used to enable clean galvanic contact with the ground in overlapping regions, leveraging the argon milling recipe introduced and tested in Ref. [122]. (b) Optical false color image of the end section of the CPW coupled to several ring resonators. The central line splits into either rectangular coupling strips or (c) a semicircle at its end. Both the central line and the ground plane in this region consist of 10 µm wide superconducting strips of Nb + Al (see panel (a)), to minimize flux trapping. (d) Scanning Electron Microscope (SEM) images of a granular aluminum ring resonator, highlighting the densely packed meander traces achieved through a single-step e-beam lithography process followed by lift-off. (e, f) SEM images of the meandering lines at increasing magnification.

2.3 Finite Element Modeling of Resonators

To determine the intrinsic resonant frequencies of the ring resonators, we performed eigenmode simulations using the finite element solver Ansys HFSS. The resonator geometry

was modeled on a sapphire substrate and enclosed in a rectangular airbox with dimensions large enough to mitigate boundary truncation effects. On the ring resonators, kinetic inductance was included as a reactive impedance boundary condition. The ground plane and feed line are modeled with lossless, ideal conductive (Perfect E) boundary conditions. The schematic of the simplified 2D architecture used in the simulation is shown in Fig. 2.3(a). It includes a matched load termination, which allows us to determine the coupling quality factor from the simulation.

In addition to the global mesh refinement applied by the simulation to ensure convergence, two local mesh refinements were introduced to facilitate convergence of the eigenfrequencies: a customized mesh refinement box around the resonator-CPW interface, and a more intense meshing applied in the small ring resonator area to enhance resolution in critical regions, as shown in Fig. 2.3(b).

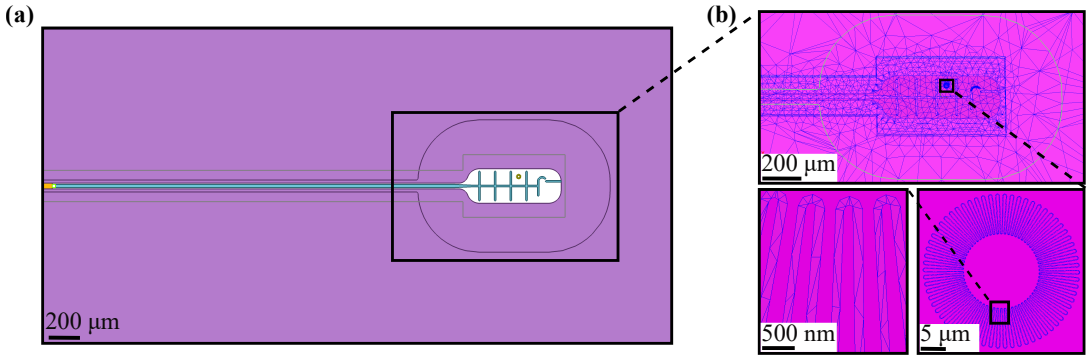

Figure 2.3: Simulation Setup and Meshing for Electromagnetic Finite Element Simulations with ANSYS. (a) Schematic of the 2D architecture used for ANSYS finite-element simulations, which approximates the actual fabricated design. In the simulation, the ground plane and feed line are shown in purple and blue, respectively, with ideal conductive (Perfect E) boundary conditions. The ring is placed in one of the square cutouts, and the green square represents the matched load termination (50 Ω). (b) Zoomed-in views of the simulation mesh. The mesh is automatically generated and refined to aid convergence. A customized denser mesh is applied around the resonator-CPW interface region to ensure accuracy in areas critical to the electromagnetic response. Smaller features, such as the ring resonator, are assigned even finer meshing to support convergence.

2.4 Fabrication Details

2.4.1 Fabrication of Granular Aluminum Ring Resonators

The fabrication of grAl ring resonators begins with spin-coating a 200 nm thick PMMA resist layer on a double-polished c-plane sapphire substrate with a diameter of 2 inches and

a thickness of 330 µm. The resist is baked at 150 °C for 3 min to ensure uniform adhesion. To prevent charging effects during e-beam exposure, a conductive coating (Electra 92) is applied over the resist. This conductive layer is removed prior to development.

The resonator patterns are defined using a 50 kV e-beam lithography system, enabling high-resolution features with pitches p ranging from 200 nm to 520 nm and wire widths w between 150 nm and 170 nm. Following exposure, the resist is developed, defining the ring-resonator patterns, and the sample is then transferred to a Plassys deposition chamber. GrAl films are deposited by e-beam evaporation of pure aluminum in a controlled oxygen environment, forming granular films with resistivities used here ranging from 800 µΩ cm to 2500 µΩ cm. After deposition, the resist is removed via lift-off, leaving behind the grAl structures precisely defined according to the desired design specifications. The fabrication steps are summarized in Table 2.1. The resulting compactness, pitch, linewidth, and thickness achieved using this process are shown in Fig. 2.4.

Table 2.1: Summary of Fabrication Details for the Ring Resonators. The process includes resist spinning, e-beam lithography for patterning, plasma cleaning, and aluminum evaporation in a dynamic oxygen environment. The resistivity of the resulting grAl films ranges from 800 µΩ cm to 2500 µΩ cm.

Resist Coating	
Substrate	C-plane sapphire
E-beam resist	PMMA A4 (thickness = 200 nm)
Acceleration	1000 rpm/s
Spread cycle	300 rpm for 4 s
Spin speed	5000 rpm for 60 s
Baking temperature	150 °C for 3 min
Conductive coating	Electra 92 (AR-PC 5090)
Acceleration	1000 rpm/s
Spread cycle	500 rpm for 1 s
Spin speed	2000 rpm for 60 s
Baking temperature	85 °C for 2 min

E-Beam Exposure	
Acceleration voltage	50 kV
Beam current	100 pA
Step size	10 nm
Development	
Conductive coating removal	Water (RT) for 30 s
Developer	MIBK 1:3 IPA at 0 °C for 30 s
Deposition Process	
Plasma Cleaning	
Mass flows	O_2/Ar (10 sccm/5 sccm)
Beam parameters	$U_{\text{beam}} = 200\,\text{V}$ $I_{\text{beam}} = 10\,\text{mA}$
Gettering	
Ti evaporation rate	0.2 nm/s for 2 min
grAl Deposition	
Al evaporation rate	1 nm/s
O_2 pressure	10^{-5} to 10^{-4} mbar

2.4.2 Fabrication of Coplanar Waveguide and Ground Plane

The CPW structure and the Ag ground plane are fabricated in two consecutive optical lithography steps, each including a lift-off process. Each process begins with spin-coating a layer of photoresist (AZ 5214E) onto the substrate. After the resist is applied, the desired patterns are written using UV lithography, followed by development to form the pattern. The metallization process for the CPW structure involves the sequential deposition of Nb and Al films via e-beam evaporation. The specific steps for resist coating, UV exposure, and development are detailed in Table 2.2. To ensure proper galvanic contact between the Ag and the CPW structure, an Ar milling step is performed before deposition. In order to remove any oxide layers on the underlying Al, enhancing the electrical connectivity

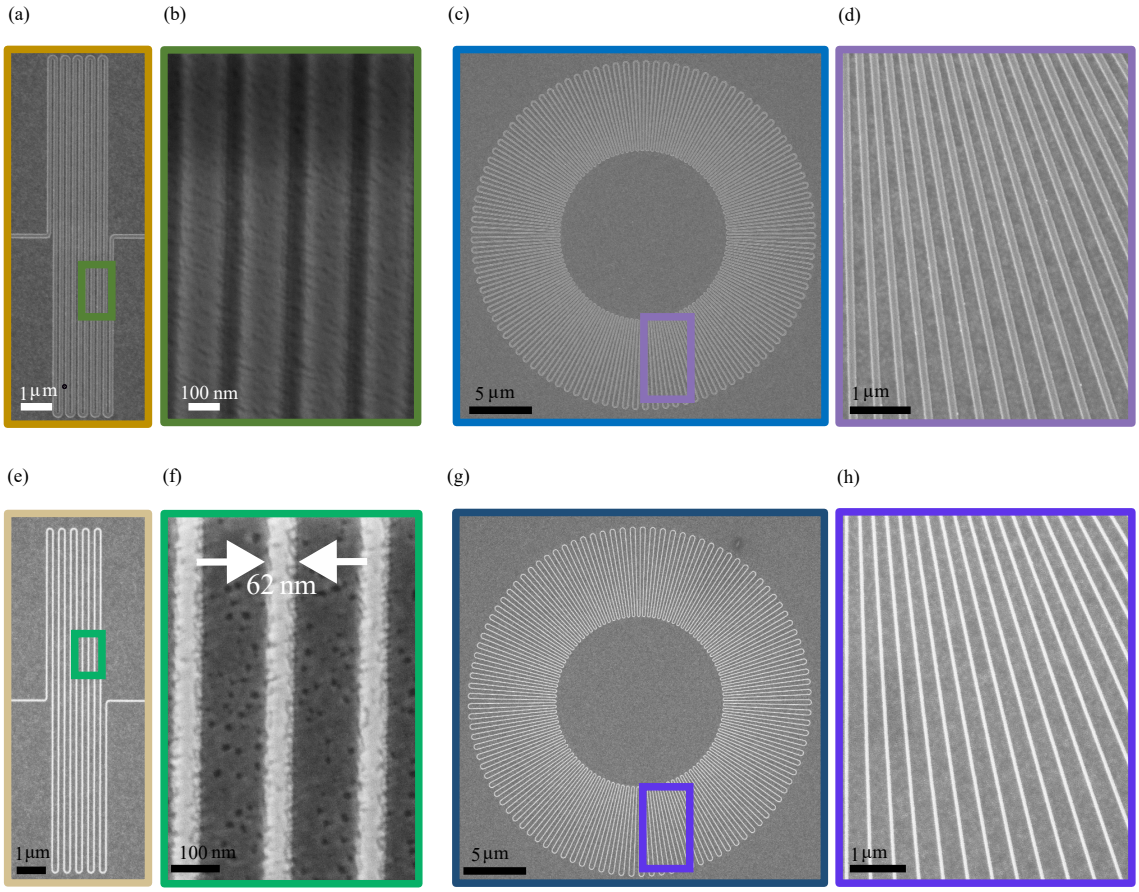

Figure 2.4: Packed and Narrow Meandering GrAl Lines. SEM images of grAl meandering lines with a thickness of 30 nm, patterned using electron beam lithography. (a, b) Test structures with meandering lines matching the width of those in ring resonators. These simpler designs were used to optimize the fabrication recipe, achieving a packing density with a pitch of less than 200 nm. (c, d) Ring resonators fabricated with the same packing density as the test structures, showing results over longer lines with a greater number of meanders. (e, f) Test structures highlighting the minimum reproducible linewidth of about 60 nm.
(g, h) Ring resonators incorporate the same narrow lines as the test structures, indicating the possibility of making narrow widths in more complex geometries.

between the Ag ground plane and the CPW structure. After the fabrication steps are completed, the devices are protected with a thin resist layer to prevent contamination. The chips are then diced into individual pieces with dimensions of 6 mm by 6 mm, making them ready for integration into the experimental setup.

Table 2.2: Summary of Fabrication Details for the Coplanar Waveguide and Ag Ground Plane. The process includes resist spinning, UV lithography for patterning, plasma cleaning, and Nb + Al metallization. The Ag ground plane was deposited using an additional optical lithography step with a preceding Ar milling process to remove Al oxide, ensuring galvanic contact between overlapping Ag and Nb + Al structures.

Resist Coating	
Substrate	C-plane sapphire
Photoresist	AZ 5214E
Acceleration	2000 rpm/s
Spin speed	4000 rpm for 60 s
Baking temperature	110 °C for 50 s
UV Exposure	
1st Exposure	
Exposure power	2 mW for 12 s
Baking	
Baking temperature	120 °C for 60 s
2nd Exposure	
Exposure type	Flood exposure for 30 s
Development	
Developer	AZ developer 3:2 water for 30 s
Deposition Process	
Plasma Cleaning	
Mass flows	O_2/Ar (10 sccm/5 sccm)
Beam parameters	$U_{\text{beam}} = 200\,\text{V}$ $I_{\text{beam}} = 10\,\text{mA}$
Gettering	
Ti evaporation rate	0.2 nm/s for 2 min
Nb + Al Deposition	
Nb evaporation rate	1 nm/s

Al evaporation rate	1 nm/s
Ag Deposition	
Ag evaporation rate	1 nm/s

2.5 Setup

This section describes the experimental setup and sample box used for measuring the ring resonators. As shown in Fig. 2.5, the chip is mounted inside a non-magnetic, oxygen-free high-conductivity (OFHC) copper sample box. The CPW is connected via aluminum wire bonds to a 50 Ω transmission line, while the ground plane is bonded directly to the copper enclosure. The box is sealed with a tightly screwed lid to minimize radiation leakage. It is mounted on a copper rod connected to the mixing chamber (MXC) stage of a dilution refrigerator.

The sample box is enclosed within magnetic shields, similar to the configuration used by Grünhaupt et al. [122]. These include a copper/aluminum bilayer shield and a mu-metal shield to suppress external magnetic fields.

The input signal, generated by a vector network analyzer (VNA), is sent through cables. Attenuators are installed at various cryogenic stages (as detailed in Fig. 2.5) to reduce thermal noise before the signal reaches the sample. For reflection measurements, a cryogenic circulator is used to separate the input and output paths. The reflected signal passes through a two-stage isolator that blocks thermal radiation from the 4 K stage, followed by a low-pass filter. It is then amplified by a low-noise high electron mobility transistor (HEMT) amplifier at 4 K, and again at room temperature, before returning to the VNA.

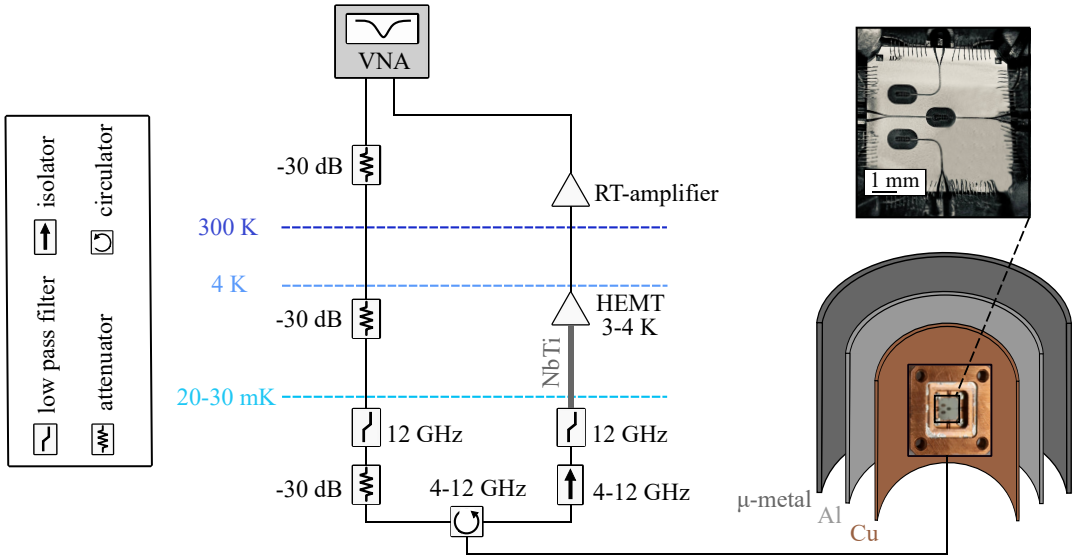

Figure 2.5: Experimental Setup. The setup includes a sample box containing the device under test, placed at the 20 mK MXC stage of a dilution cryostat. The device is enclosed in multiple layers of magnetic shielding. A signal from the VNA is sent through coaxial cables with attenuators at each cryogenic stage. Reflection measurements are performed using a cryogenic circulator, and the reflected signal is amplified by both cryogenic and room-temperature amplifiers before returning to the VNA.

2.6 Resonator Impedance

2.6.1 Resonator Impedance Measurements

In Fig. 2.6(a), we present a typical phase response of a ring resonator measured in microwave reflection. The two fundamental modes are clearly distinguishable, separated by approximately 25 MHz, with their respective coupling quality factors Q_c differing by a factor of four.

A summary of the measured fundamental mode frequencies for eleven rings is shown in Fig. 2.6(b), covering grAl resistivities between 800 μΩ cm and 2500 μΩ cm. Finite element simulations were performed for rings with varying ℓ, and by matching the simulated and measured frequencies, we extracted the inductance per square for each grAl film, which ranges from 180 to 670 pH/□.

The characteristic impedance up to the first fundamental mode f_0 is determined using the expression

$$Z = 2\pi f_0 L, \tag{2.1}$$

where L represents the total inductance of the ring [75, 78], as shown in Fig. 2.6(c).

The highest measured impedance, 127 kΩ, corresponds to a ring with a sheet inductance of 670 pH/□ and specific geometric parameters: a pitch of 325 nm, an inner radius of $r_{\text{in}} = 6.7\,\mu\text{m}$, an outer radius given by $r_{\text{out}} = 2r_{\text{in}}$, and a thickness of 20 nm. A complete summary of all measured devices is provided in Table 2.3.

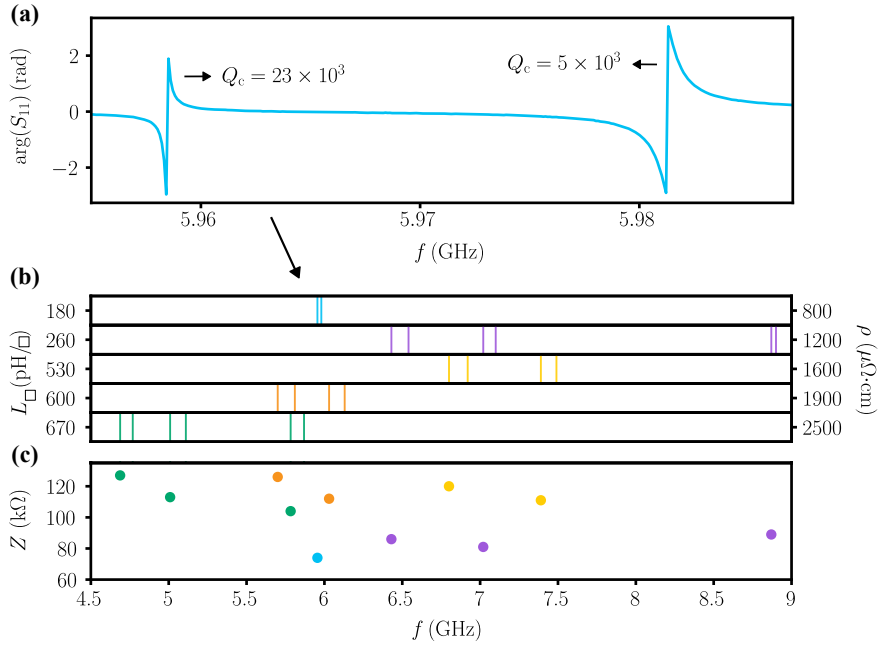

Figure 2.6: Frequency and Impedance of Granular Aluminum Superinductors. (a) The graph shows the phase response of one of the doublet ring resonances with the frequency separations of approximately 25 MHz, pointing to the asymmetry due to the difference in coupling capacitance of the two modes and fabrication imperfections. (b) The frequency spectra of the fabricated and measured granular aluminum ring resonators. Each row corresponds to an inductance per square and the corresponding resistivity as determined from Eq. (1.54). (c) The graph determines the impedance of each ring resonator up to the first fundamental mode. The filled circular markers represent the measured impedance of the fabricated and characterized rings, with the highest impedance recorded at 127 kΩ at a resonance frequency of 4.6 GHz. These values are obtained using Eq. (2.1).

Table 2.3: Summary of Ring Resonator Parameters. Included are geometrical dimensions, $L_\square$, L, Z, and f_0 extracted from both measurements and simulations. Q_c were determined using the circle fitting method. This table outlines the key design parameters influencing resonator performance, providing a basis for optimization in various applications.

Resonator	r_{in} (µm)	w (nm)	l (µm)	p (nm)	t (nm)	f_0 (GHz)	$L_\square$ (pH/□)	L (µH)	C (fF)	Z (kΩ)	Q_c ($\times 10^3$)
1	9.1	170	1849	300	30	5.95	180	1.95	1.46	72.9	23
2	9.1	170	1849	300	30	5.98	180	1.95	1.45	72.9	5
3	7.4	150	1239	300	30	6.43	260	2.14	1.14	86.45	5
4	7.4	150	1239	300	30	6.54	260	2.14	1.10	86.45	600
5	7.4	150	1066	355	30	7.02	260	1.84	1.11	81.15	150
6	7.4	150	1066	355	30	7.10	260	1.84	1.09	81.15	20
7	5.2	150	928	200	30	8.87	260	1.60	0.80	89.17	25
8	5.2	150	928	200	30	8.9	260	1.60	0.79	89.17	22
9	4.8	150	796	200	20	6.80	530	2.81	0.78	120.05	50
10	4.8	150	796	200	20	6.92	530	2.81	0.75	120.05	30
11	4.8	150	681	240	20	7.39	530	2.40	0.77	111.43	230
12	4.8	150	681	240	20	7.49	530	2.40	0.75	111.43	130
13	5.6	150	875	300	20	5.70	600	3.50	0.89	125.35	200
14	5.6	150	875	300	20	5.81	600	3.50	0.85	125.35	130
15	5.6	150	741	253	20	6.03	600	2.96	0.94	112.14	60
16	5.6	150	741	253	20	6.13	600	2.96	0.91	112.14	6
17	6.7	150	966	325	20	4.68	670	4.31	1.07	126.7	140
18	6.7	150	966	325	20	4.76	670	4.31	1.03	126.7	50
19	6.7	150	806	400	20	5.00	670	3.60	1.12	113.09	8
20	6.7	150	806	400	20	5.11	670	3.60	1.07	113.09	6
21	6.7	150	646	518	20	5.78	670	2.88	1.05	104.59	260
22	6.7	150	646	518	20	5.86	670	2.88	1.02	104.59	30

2.6.2 Impedance Model Based on Geometric Parameters

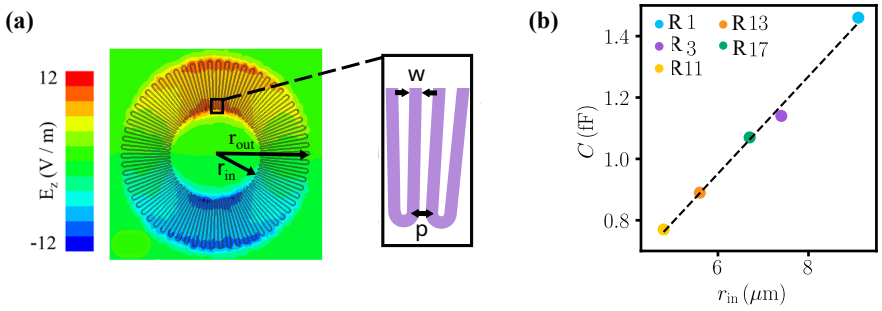

Figure 2.7: Geometric Design and Capacitance Scaling in Ring Superinductors. (a) Electric field distribution of the ring superinductor, highlighting the capacitor plates and the remaining sections of the ring acting as inductors. We define r_{in} and r_{out} of the ring resonator as indicated, the outer radius is fixed at twice the inner radius, $r_{\text{out}} = 2r_{\text{in}}$. The schematic next to the plot illustrates how we define wire width w and pitch p. (b) Capacitance as a function of r_{in} for rings with varying inductance per square and resistivity. Each data point corresponds to a specific resonator, with details listed in Table 2.3. The dashed line acts as a guide to the eye and confirms the linear dependence of capacitance on r_{in} for the range of design parameters used here.

To understand the scaling behavior of the impedance and resonance frequency in meandered ring resonators, we begin by analyzing their inductive and capacitive components based on simple geometric approximations in ring resonators. It helps to understand the scaling behavior of the impedance and resonance frequency in terms of geometric properties. Ignoring the contributions from the curved sections, which can be approximated as the sum of πr_{in} and πr_{out}. The total inductance of the structure can be expressed as:

$$L \approx N L_{\square} \frac{r_{\text{in}}}{w}, \tag{2.2}$$

where $L_{\square}$ is the inductance per square, w is the linewidth, and r_{in} is the inner radius of the ring. As illustrated in Fig. 2.7(a), the outer radius follows $r_{\text{out}} = 2r_{\text{in}}$. The number of meanders N is proportional to $2\pi r_{\text{in}}/p$, with p being the pitch (i.e., the sum of the wire width and the spacing between lines). Substituting this relation leads to a quadratic scaling of the inductance with the ring radius:

$$L \propto \frac{r_{\text{in}}^2 L_{\square}}{pw}.$$

The capacitance C of the ring can be approximated by considering it as a coplanar capacitor with square electrodes of side length r_{in}, separated by a distance of approximately $2r_{\text{in}}$. The capacitance scales linearly with r_{in}, i.e., $C \propto r_{\text{in}}$ [123]. This linear scaling is confirmed using HFSS, as shown in Fig. 2.7(b), validating this simplification.

Combining the expressions for L and C, the resonance frequency f_0 of the circuit can be derived from the harmonic oscillator relation:

$$f_0 = \frac{1}{2\pi\sqrt{LC}} \propto \sqrt{\frac{pw}{r_{\text{in}}^3 L_\square}}.$$

The characteristic impedance Z of the resonator is obtained from the ratio $Z = \sqrt{L/C}$. Using the previous scaling relations, the impedance can be approximated as:

$$Z \propto \sqrt{\frac{r_{\text{in}} L_\square}{pw}}. \tag{2.3}$$

As shown in Fig. 2.8, the measured impedance of our resonators agrees with the predicted scaling. In particular, the product of the impedance and the resonance frequency is inversely proportional to the inner radius. This means that, to maximize impedance at a given frequency, the inner radius should be minimized. We can compensate the resulting change in frequency by decreasing the ratio $pw/L_\square$. The lowest achievable value for the ratio $pw/L_\square$ depends on the grAl material properties and the finesse of the lithography. The maximum value for $L_\square$ is limited by the resistivity threshold for the grAl superconducting-to-insulating transition [108, 124], in the range of 10 m$\Omega \cdot$ cm, and by the thinnest continuous and stable films. For grAl films below 20 nm, we observe significant fluctuations in their resistivity between different cooldowns, indicating that structural inhomogeneities and instabilities play a dominant role. We found that structures with $w \geq 150$ nm always resulted in stable devices, which was not the case for $w \approx 60$ nm, likely due to inhomogeneities in the wires. The smallest pitch we could achieve with our current electron-beam lithography (see Fig. 2.4) was 200 nm. Taking these considerations into account, we believe that a fine-tuned optimal grAl device operational in the 4-8 GHz range can reach impedance values in the range of 200 kΩ on silicon or sapphire substrates (the simulation result, as a guide how to get to this value, is presented in the next section), and this value can be increased by a factor of ≈ 3, to exceed 0.5 MΩ for suspended devices.

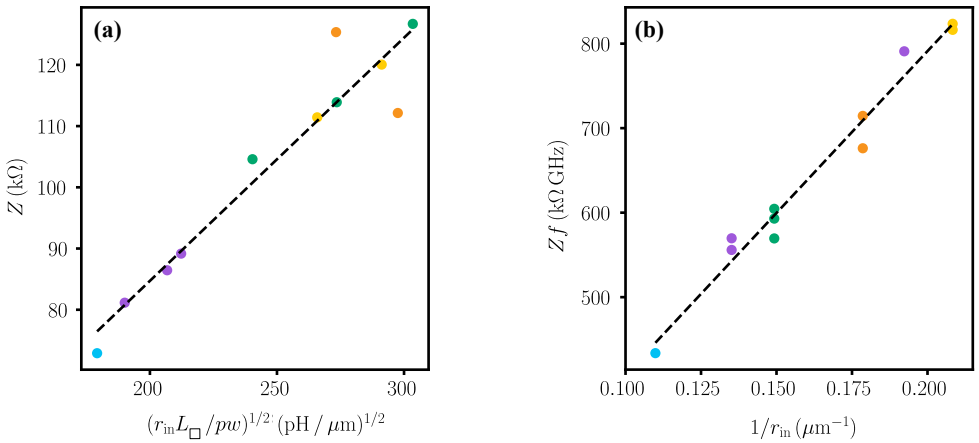

Figure 2.8: Measured Impedance Scaling with Geometry and Resistivity. Plot of measured Z in panel (a) and Zf in panel (b) as a function of $(r_{\mathrm{in}}L_{\square}/pw)^{1/2}$ and $1/r_{\mathrm{in}}$, respectively, confirming their linear dependence (cf. dashed lines), consistent with Eq. (2.3). At high-impedance, in panel (a), we note a larger spread between the points, which could be explained by film and patterning inhomogeneities. The color code in both panels is consistent with Fig. 2.6. Details for each resonator are given in the Table 2.3.

2.7 Simulating High-Resistivity GrAl Resonators

To investigate how grAl resonators perform in the high-resistivity regime, we do a series of simulations. In this regime, the sheet inductance becomes larger, directly influencing both the resonance frequency and characteristic impedance of the resonator.

We simulated grAl ring resonators with $L_{\square}$ values ranging from 1200 to 1800 pH/□, corresponding to resistivities between 4338 μΩ · cm and 6490 μΩ · cm; these values remain within a range where superconductivity is preserved.

The simulations are performed using the eigenmode solver in ANSYS HFSS, which estimates resonance frequencies based on the device geometry and material parameters. From these results, we extracted the corresponding impedance values for each simulated configuration.

A detailed summary of all simulated parameters, resonator dimensions, inductance, resonance frequencies, and impedances, is presented in Table 2.4. The impedance values as a function of frequency are plotted in Fig. 2.9, illustrating how higher resistivity enables higher impedance in the frequency range of 4 to 8 GHz.

These results serve as a guide for extending the design of grAl resonators toward higher impedance.

Table 2.4: Summary of Simulated Ring Resonator Parameters. It includes geometrical dimensions, $L_\square$, L, Z, and f_0. The parameters were derived using eigenmode simulations in ANSYS HFSS, focusing on the higher resistivity regime of grAl below SIT. These results provide guidelines for designing resonators within the 4–8 GHz frequency range by optimizing impedance and frequency characteristics.

Resonator	r_{in} (µm)	w (nm)	l (µm)	p (nm)	t (nm)	f_0 (GHz)	$L_\square$ (pH/□)	L (µH)	C (fF)	Z (kΩ)
23	3.2	120	367	200	20	7.3	1200	3.67	0.518	170
24	3.69	120	469.8	200	20	6.07	1200	4.69	0.586	179
25	4.07	120	571.9	200	20	5.22	1200	5.71	0.651	187
26	4.77	120	775.7	200	20	4.14	1200	7.75	0.763	201
27	3.31	120	377	200	20	6.43	1500	4.7	0.521	190
28	3.62	120	459	200	20	5.53	1500	5.7	0.581	199
29	4.2	120	622	200	20	4.39	1500	7.7	0.683	214
30	2.9	120	316	200	20	6.7	1800	4.7	0.480	199
31	3.6	120	452	200	20	5.09	1800	6.7	0.584	217
32	4.13	120	588	200	20	4.1	1800	8.8	0.685	227

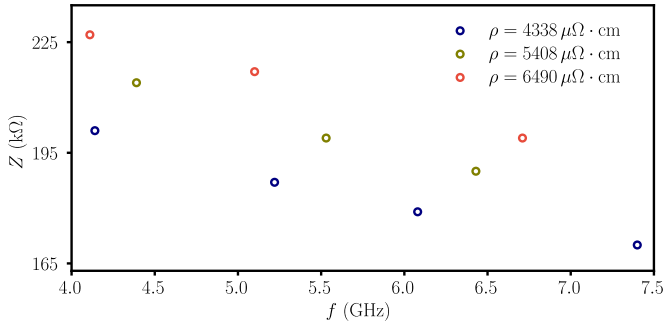

Figure 2.9: Prospective GrAl Impedance Optimization. Simulated impedances up to the fundamental mode, indicated by the x-axis, for the designs summarized in Table 2.4.

2.8 Resonator Performance

2.8.1 Noise Spectral Density

To evaluate the phase and frequency stability of the grAl resonators, the noise spectral density $S(f)$, measured in units of $\mathrm{Hz}/\sqrt{\mathrm{Hz}}$, was calculated by monitoring the resonance frequency over time. We applied the method used in Ref. [125]. As shown in Fig. 2.10(a), the noise spectrum shows a $1/f$ dependence at low frequencies. This behavior is mainly attributed to intrinsic loss mechanisms in the resonators and can be described by a model where $S_{1/f^\alpha} \propto f^{-\alpha}$, with α close to 1. In our measurements, α ranges from approximately 0.8 to 0.97, which may reflect contributions from other noise sources.

At higher frequencies, the noise spectrum typically flattens, resulting in a frequency-independent white noise background. The overall behavior can therefore be modeled as

$$S(f) = S_0 + S_{1/f^\alpha}, \tag{2.4}$$

where S_0 represents the white noise floor.

Notably, in some resonators with higher resistivity, deviations from the pure $1/f$ model are observed. In these cases, the noise spectrum is better described by including a Lorentzian component, which suggests the presence of random telegraph noise (RTN). RTN, characterized by an exponential decay with a specific correlation time, has been reported in other superconducting resonators. However, in our grAl devices, RTN appears less prominent than in similar studies, such as Ref. [126].

2.8.2 Quality Factor

The internal quality factor and the coupling quality factor were extracted from the complex reflection coefficient S_{11} using a circle-fitting procedure, as described in Ref. [129]. To minimize systematic errors from Fano interference, the resonators were designed so that Q_c is comparable to Q_i.

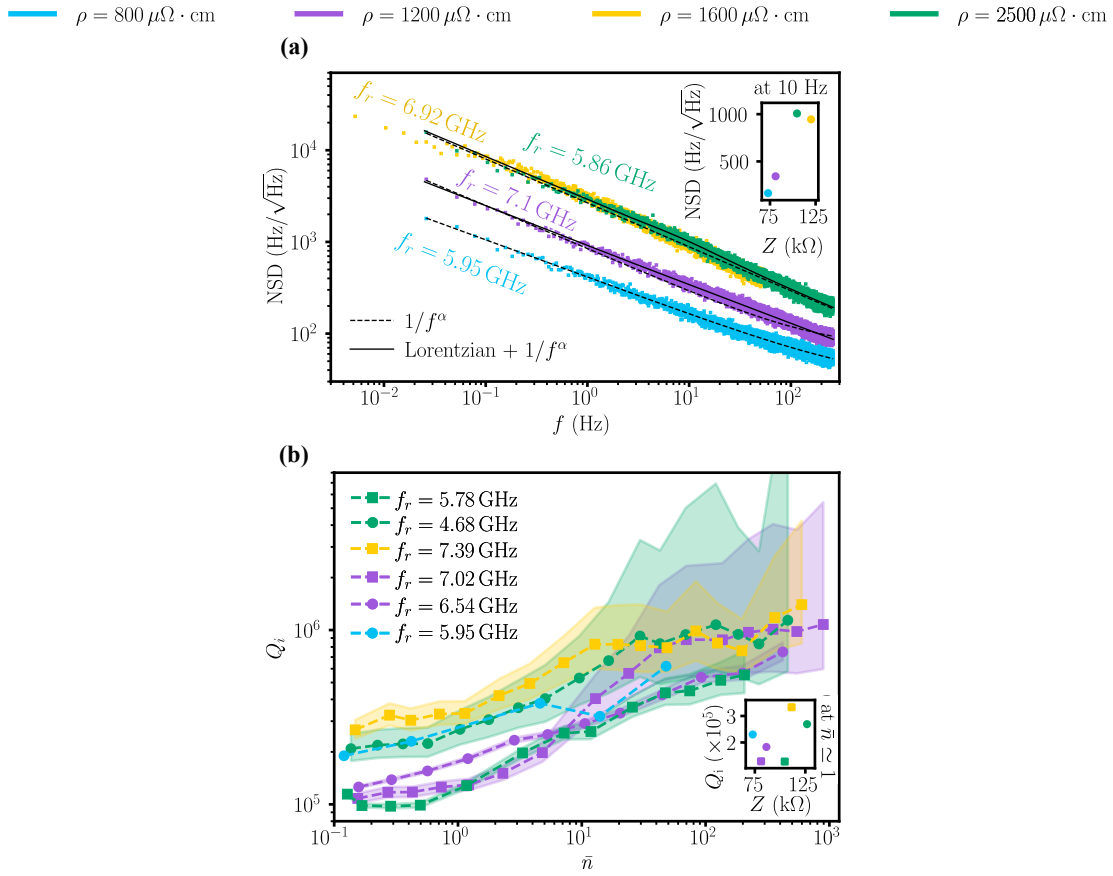

Figure 2.10: Resonator Performance: Internal Quality Factors and Noise Spectra. (a) Noise spectral density $S(f)$ as a function of frequency f for grAl resonators. The spectra were computed from time traces and are shown for four different resistivity values. The data fit the model $S(f) = S_0 + S_{1/f^\alpha}$, with α ranging from 0.8 to 0.97. The two curves corresponding to resistivity values $\rho = 2500\,\mu\Omega \cdot$ cm and $\rho = 1200\,\mu\Omega \cdot$ cm plotted in green and purple, respectively, exhibit behavior that is better described by a Lorentzian model combined with a $1/f^\alpha$ dependence at higher frequencies. The inset displays the impedance values corresponding to the frequency noise spectral densities measured at 10 Hz. (b) Intrinsic quality factors Q_i plotted against average photon numbers in the granular aluminum resonators up to the bifurcation threshold $\bar{n}_\mathrm{max}$. The average number of photons is given by $\bar{n} = 4Q_l^2 P_\mathrm{cold}/(Q_c \hbar \omega_0^2)$, where P_cold is the incident microwave power at the device [127]. The shaded intervals indicate the uncertainty range due to Fano interference [128]. For better visibility, we do not show this uncertainty range for the dataset in blue, as it approximately corresponds to an order of magnitude. The inset presents impedance values derived from single-photon Q_i measurements.

Figure 2.10(b) presents Q_i as a function of average photon number. In the single-photon regime, Q_i reaches 10^5, with no significant dependence on the resistivity or impedance of the grAl films. This is consistent with previous results for granular aluminum resonators

fabricated using similar techniques [64]. Notably, although the compact resonator geometries used here have a higher participation ratio, the observed quality factors remain high, indicating that surface dielectric loss is not the dominant limiting factor. Further improvements in fabrication and increased film thickness, as shown in Ref. [97], can reach $Q_i > 10^6$ at similar resistivities, but lower impedance. In our devices, at higher drive powers, Q_i saturates near 10^6, suggesting that the dominant loss mechanism, possibly dielectric loss [130, 131] or quasiparticle bursts [132, 133], is saturable, as commonly observed in other superconducting materials.

2.8.3 Kerr Nonlinearity

To evaluate the nonlinearity of the resonators, the self-Kerr coefficient K_{11}, representing the frequency shift of the fundamental mode per added photon, was measured. As shown in Fig. 2.11(a), K_{11} was determined by performing a linear fit to the frequency shift as a function of photon number in the high-photon-number regime. The measured K_{11} values are in the range of tens of Hz, several orders of magnitude smaller than the Kerr coefficients observed in Josephson junction arrays. This small nonlinearity highlights the suitability of grAl resonators for applications requiring a highly linear response.

The data also reveals a dependence of K_{11} on the resistivity and thickness of the grAl films. Higher resistivity and thinner films lead to larger K_{11} values, consistent with theoretical expectations that $K_{11} \propto \rho/V$, where ρ is the resistivity and V is the volume of grAl [106]. This relationship suggests that careful optimization of resistivity and film thickness can tune the Kerr nonlinearity for specific applications.

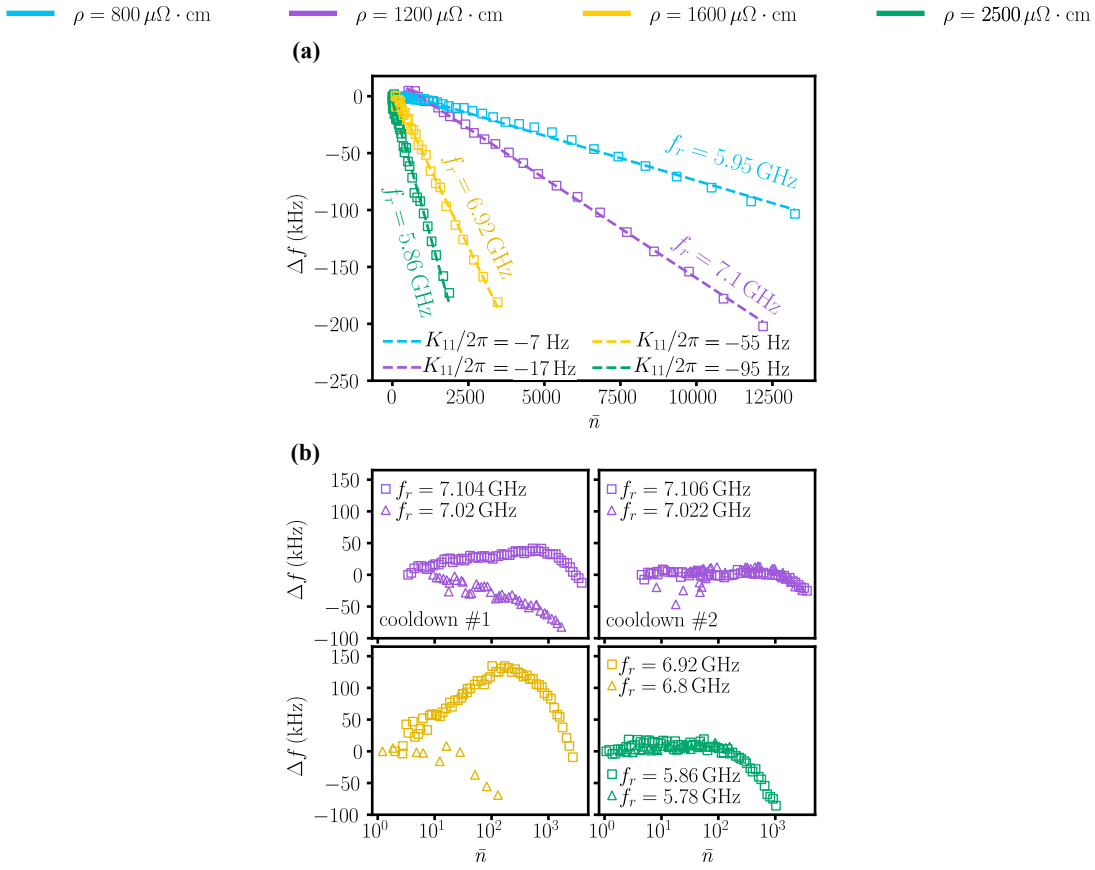

Figure 2.11: Resonator Performance: Kerr Nonlinearity and Anomalous Frequency Shifts. (a) The shift in resonance frequency as a function of the average photon number for four different rings with varying resistivity is shown. The self-Kerr coefficient K_{11} was determined by fitting the frequency shift data to a linear model. Higher resistivity grAl samples exhibit higher K_{11}, consistent with theoretical expectations that K_{11} is proportional to ρ/V, where ρ is resistivity and V is the volume [106]. (b) Anomalous shifts in resonance frequency with photon number. In some ring resonators, we observe an exponential shift to higher frequency at low photon numbers. In the top two panels, the purple data points show the two modes of the same ring resonator measured during two different cooldowns: In the first, we observe the exponential shift to a higher frequency for the higher frequency mode, while the lower frequency mode almost symmetrically shifts, but to a lower frequency. This occurs before the usual Kerr nonlinearity at higher photon numbers documented in (a). In the second cooldown, the exponential shifts are no longer observed. In the bottom left panel, a similar anomalous shift is observed for a resonator with higher resistivity grAl. Next to it, we show an example of a high-resistivity grAl resonator that does not show this anomalous shift.

2.9 Challenges in Narrow-Line Resonator Performance

Fabrication of resonators with 60 nm linewidth does not reliably produce the expected resonator behavior observed in wider-line resonators. In wider-line resonators, we observe

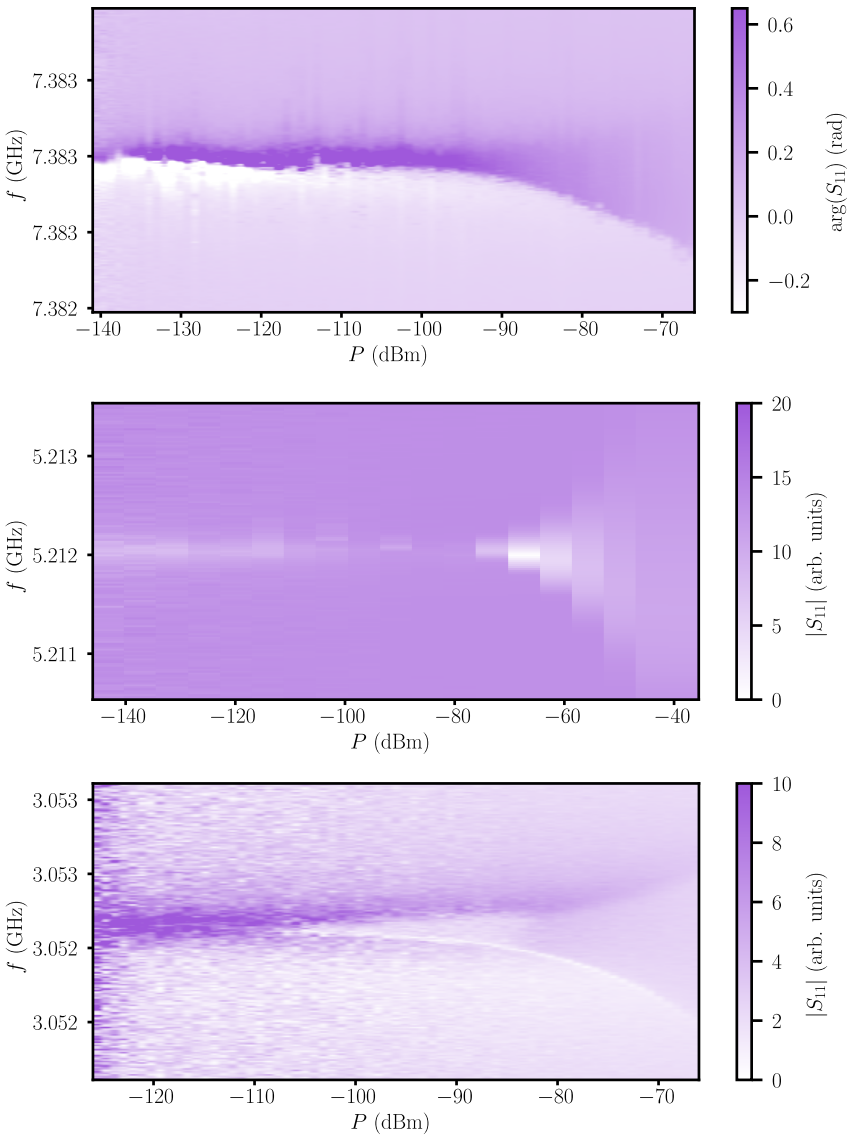

Figure 2.12: Power-Dependent Behavior of Narrow-Line Resonators. The top panel shows the phase response of a resonator near 7.383 GHz as a function of microwave power P. The color scale represents the phase of the reflection coefficient, $\arg(S_{11})$. The middle and bottom panels present the amplitude response $|S_{11}|$ of resonators near 5.212 GHz and 3.05 GHz, respectively, as a function of P. At higher powers, resonators exhibit broadening and splitting effects, indicating power-dependent anomalies. These effects are likely due to fabrication-induced imperfections. In these measurements, the unusual behavior was more clearly observed in the phase response for the 7.383 GHz resonator, while the amplitude response provided better clarity for the 5.212 GHz and 3.05 GHz resonators.

predictable features such as two closely spaced modes, each bifurcating at its respective bifurcation powers. However, for the narrow-line resonators, although some show normal responses, some have unusual features in their reflection coefficient measurements in

terms of phase and magnitude. Specifically, at high power levels, we see broadening or splitting of the resonance as shown in Fig. 2.12.

This behavior is likely due to fabrication imperfections. For instance, the edges of the narrow lines can be rough compared to the linewidth, suggesting localized discontinuities. There might be cuts or deformations caused by strain during cooldown due to differing thermal expansion coefficients of sapphire and granular aluminum. These might produce weak links, which might explain the splitting observed in power-dependent sweeps, potentially due to phenomena like resonance fluorescence, in which increasing the incident microwave power leads to a monotonic decrease in reflection magnitude and a transition to an elliptical trajectory in the Smith chart. Overall, the exact mechanism underlying this behavior remains unclear, and further investigation is required to understand and address these inconsistencies. Further optimization of the fabrication process may mitigate these issues.

2.10 Test Resonators for Reference Characterization

In addition to the high-impedance granular aluminum ring resonators studied throughout this work, we propose a complementary set of test resonators with a simpler, lumped-element geometry, as shown in Fig. 2.13(a). These resonators consist of two square parallel-plate capacitors connected by a central meandered inductor. The test resonators also provide a practical geometry for enhanced capacitive coupling to the feed line. Their capacitive elements are asymmetrically positioned, such that one plate sits closer to the CPW than the other (see Fig. 2.13(b,c)). This spatial asymmetry creates a non-uniform electric potential, resulting in a dipole moment that couples strongly to the transmission line. The inductor's geometric parameters, including wire width, pitch, and thickness, are deliberately matched to those of the ring resonators, and the test structures can be placed on the same chip as the ring resonators. This design ensures that both types of resonators have identical sheet kinetic inductance properties, enabling the test resonators to serve as reliable reference devices.

The main purpose of these test resonators is to provide a practical and independent means of extracting film parameters such as the sheet inductance $L_{\mathrm{k}}^{\square}$ and normal-state sheet resistance $R_{\mathrm{n}}^{\square}$, particularly in cases where multiple ring resonators with varying lengths are not available on the same chip. By designing several test resonators with different inductor lengths, but keeping the capacitor geometry fixed, the capacitance C remains constant, so the resonance frequency f_0 depends only on the inductance L according to the

standard relation, $f_0 = 1/2\pi\sqrt{LC}$, fitting the measured resonance frequencies of these test structures to this model enables the determination of the inductance per unit length, and thus the sheet inductance. From there, the sheet resistance can also be calculated using Eq. (1.54).

However, in this study, we did not use this method to determine $L_\square$ for the chip on which these test resonators were fabricated. Instead, we followed the approach described in Section 2.6, where the sheet inductance was extracted by fitting the measured resonance frequencies of ring resonators with different lengths to simulated values. This method was used consistently for all chips in the study.

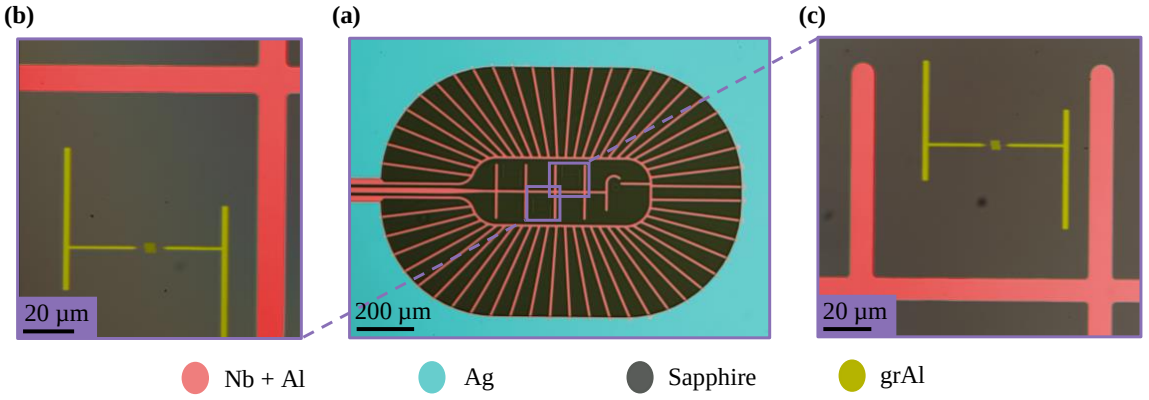

Figure 2.13: Design of the Lumped-Element Test Resonators Proposed for Sheet Inductance Extraction. (a) False-color optical image showing three lumped-element test resonators patterned near the end of the coplanar waveguide on the chip. Each resonator features a different meandered inductor length and is placed within an individual rectangular enclosure to minimize crosstalk and interference. (b,c) Zoomed-in optical image of two test resonators with a central meandered inductor and two square parallel-plate capacitors. The inductor has identical width, pitch, and thickness to those used in the granular aluminum ring resonators, ensuring comparable sheet inductance. The asymmetric placement of the capacitor plates in the design achieves stronger capacitive coupling to the transmission line.

The internal quality factors of two of the test resonators were extracted as a function of average photon number (see Fig. 2.14). In the single-photon regime, both resonators have $Q_\mathrm{i} \sim 10^5$, which is comparable to the performance observed in the ring resonators. This result suggests that the more complex distributed geometry of the ring does not inherently introduce extra loss relative to simpler lumped-element designs. The coupling quality factors for these devices ranged from approximately 21×10^3 to 27×10^3. Given the strong coupling, errors due to Fano interference were not included, as the errors diverge in some areas at higher photon numbers.

It is worth mentioning again that these test resonators were fabricated and measured only on one of the chips in the study and were not replicated across chips with different

resistivity values. Accordingly, while the test resonator design is proposed as a useful fallback strategy for parameter extraction in the absence of ring resonators with varying lengths, all values of $L_\square$ reported in this thesis were derived from the ring-based method.

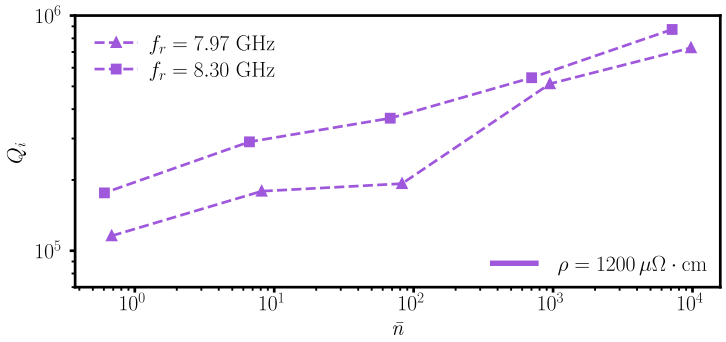

Figure 2.14: Internal Quality Factors of Test Resonators. This plot shows the intrinsic quality factor as a function of average photon number for two lumped-element test resonators fabricated on the same chip as the granular aluminum ring resonators. Both devices exhibit approximately $Q_\mathrm{i} \sim 10^5$ in the single-photon regime, which is comparable to the values observed in the ring-based designs. The data corresponds to a grAl film with resistivity $\rho = 1200\ \mu\Omega \cdot$ cm, and resonance frequencies of 7.97 GHz and 8.30 GHz, respectively. Fano interference errors are not plotted for these strongly coupled resonators, because such errors become too large and infinite in some high-photon-number regimes.

2.11 Qubit Design Based on Ring Superinductor

In this section, we explore how the ring resonators could be adapted to make a superconducting qubit. The idea is to cut a section of the ring to include a Josephson junction (JJ) as a nonlinear element, as shown in Fig. 2.15(a). To reduce sensitivity to flux noise, the qubit spectrum should be flattened with respect to flux, which can be achieved by adding a high impedance component to the circuit. An example of a junction, fabricated via three-angle shadow evaporation, is shown in Fig. 2.15(b).

One appealing aspect of the design is that the ring can serve as a superinductor but also as a readout resonator. As described previously, the symmetric ring supports two fundamental modes. Inserting the junction breaks the symmetry, one mode would be related to the qubit (usually with a lower frequency due to added capacitance), and the other can be used as the readout.

The coupling between the qubit and the readout mode comes from an intentional asymmetry in the design, by making the left and right inductive segments of the ring have slightly different lengths, this allows the readout mode to couple inductively to the qubit.

Importantly, the amount of length difference between the segments directly determines the coupling strength, enabling tunability without additional circuit elements. This mechanism has a similar strategy to Ref. [134].

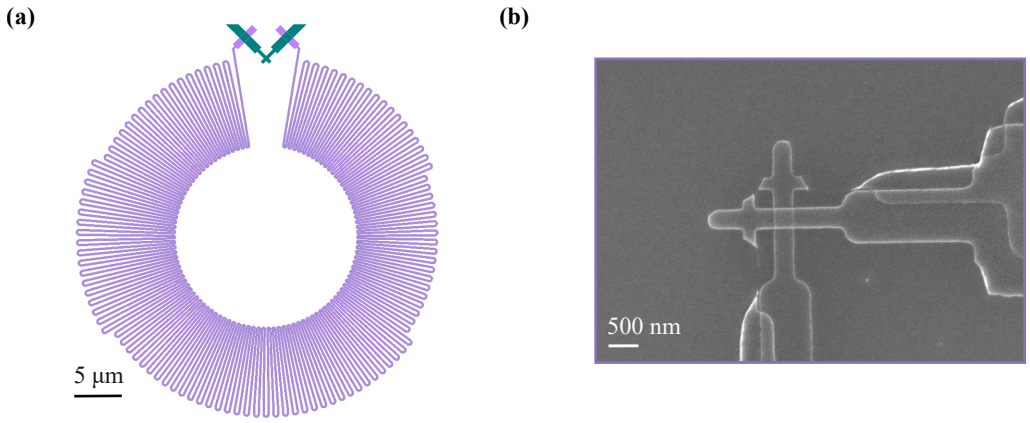

Figure 2.15: Design for a Ring-Based Qubit. (a) Design of a ring superinductor with a nonlinear Josephson junction added. The asymmetry between the left and right arms enables the inductive coupling to the readout mode. (b) SEM image of the Josephson junction part with approximate dimensions of 350 nm × 350 nm, fabricated using a three-angle shadow evaporation technique.

Summary

In this chapter, we present the design, fabrication, and characterization of compact, high-impedance meandered ring resonators made from granular aluminum. We use a single-step lift-off e-beam lithography process to fabricate the ring resonators. The resulting devices operate in the microwave regime (4–8 GHz), exhibiting characteristic impedances exceeding 100 kΩ, about 16 times the resistance quantum R_Q, and kinetic inductances as high as 4 µH.

We introduced a model to predict the impedance and frequency based on resistivity and geometric parameters, within practical lithographic and material limits. The model's validity is tested by measured results from multiple devices, showing good agreement.

Depending on the grAl resistivity, we measure frequency noise spectral densities in the range of 10^2 to 10^3 Hz/$\sqrt{\text{Hz}}$ at 10 Hz. The resonators have internal quality factors on the order of 10^5 in the single-photon regime and self-Kerr nonlinearities in the tens of Hz, making them suitable for quantum information processing.

Finally, we propose new design parameters to further increase the impedance and mention here that impedance values above 0.5 MΩ could be achieved by reducing the effective

dielectric constant through substrate modifications such as backside etching or full release of the film from the substrate.

3 DC-Tunable Granular Aluminum Resonators

DC-tunable resonators based on high-kinetic-inductance materials enable frequency tuning in superconducting quantum circuits, with applications in parametric amplification, phase shifting, tunable coupling, and two-level system (TLS) spectroscopy. In this work, conducted in collaboration with the Swedish company, Low Noise Factory (LNF) under the supervision of David Niepce and Sumedh Mahashabde, the tunability of granular aluminum (grAl) resonators is investigated under direct current (DC) biasing. Tunable fractal resonators from grAl are fabricated and characterized, using a $3\lambda/4$ tuning fork geometry with galvanic ground connections to allow direct current injection. By applying a DC bias, in-situ frequency tunability through the nonlinear kinetic inductance of grAl is achieved, observing tunabilities between 2.85% and 4.54% before reaching the critical current. Noise spectral density measurements show values between 100 and 300 Hz/$\sqrt{\text{Hz}}$ at 10 Hz. The intrinsic quality factor Q_i is measured to be on the order of 10^4 in the single-photon regime.

3.1 Introduction

Tuning the inductance in microwave superconducting resonators enables a wide range of applications, for example, Parametric Amplifiers (PAs) [135–139] and Traveling Wave Parametric Amplifiers (TWPAs) [88, 111, 140–144], which achieve signal amplification through parametric pumping of a nonlinear medium with current-dependent inductance. Other applications include phase shifters (due to the phase dependence on inductance) [145–147], two-level system (TLS) spectroscopy [148], magnetometry [149], and microwave storage [150].

A widely used approach to achieve such tunability is through Josephson junction (JJ) arrays and superconducting quantum interference devices (SQUIDs) [55, 147, 151–159].

Josephson junctions, owing to their strong intrinsic nonlinearity [142, 160], can provide a tunability range of up to approximately 50% [136]. However, Josephson junction-based parametric amplifiers are limited by low saturation power [161] and restricted dynamic range [162], primarily due to their relatively low critical current I_c on the order of μA [160, 161, 163] and low critical temperature T_c [161, 164]. Additionally, their low critical magnetic field B_c [165] makes them unsuitable for applications that benefit from stronger magnetic fields, such as electron spin resonance (ESR) [166, 167], resonator-spin ensemble coupling [168] and spin qubits [169].

An alternative approach for implementing tunable resonators and parametric amplifiers is the use of high kinetic inductance superconducting materials such as granular aluminum (grAl), NbN, TiN, or NbTiN [88, 111, 137–140, 145, 146, 149, 160, 163, 170–173]. These materials typically exhibit higher B_c, I_c, and T_c compared to JJs, resulting in enhanced saturation power and dynamic range [89, 160, 161, 163, 165] and enabling operation at higher temperatures and magnetic fields. In general, the fabrication is simplified when replacing Josephson junction arrays with traces of high kinetic inductance material. To implement tunability across both Josephson junction-based systems and high kinetic inductance materials, common control methods include applying a direct current (DC) bias or an external magnetic field.

Knowing the advantages of using disordered superconductors in applications requiring kinetic inductance tuning, we study the tunability of grAl, a particularly compelling choice due to its high and tunable kinetic inductance, low microwave loss, and compatibility with standard nanofabrication techniques. In the following, we will present a resonator design and fabrication method for DC-tunable grAl resonators. Finally, the results of tuning resonators composed of grAl with three different sheet inductances by a direct current are presented.

3.2 DC Tunable Fractal Resonators Design

The device under study is a distributed $3\lambda/4$ fractal resonator made entirely from granular aluminum and is shown in Fig. 3.1(a). The design suitable for tunable operation under direct current biasing is adapted from reference [174]. The resonator is patterned in a tuning fork geometry. It consists of a central grAl strip of width $W = 15\,\mu m$, patterned from a 25 nm-thick evaporated film, separated from the grAl ground by a gap of 36 μm and an interdigitated capacitor (see Fig. 3.1(d)). The whole compact design helps to minimize the dipole moment, ensuring that coupling to parasitic resonances from the ground plane is

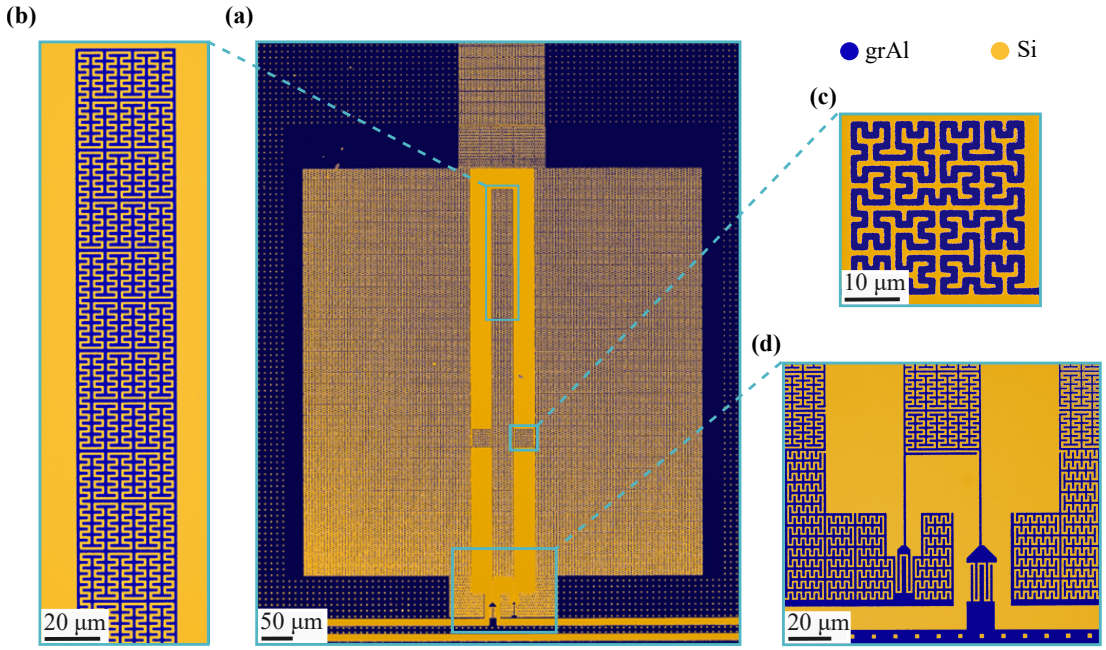

Figure 3.1: Design of DC-Tunable GrAl Fractal Resonators. (a) Optical image of a resonator with a $3\lambda/4$ tuning fork geometry fabricated from granular aluminum (grAl). The resonator is capacitively coupled to a microwave transmission line and includes galvanic ground connections at both voltage nodes to allow direct current injection. (b) Zoom-in of the resonator's U-turn section showing the path for the DC bias current, which flows along the outer trace. This current modulates the kinetic inductance, enabling frequency tunability, while the central portion primarily contributes to the capacitive response. (c) High-impedance RF filters are placed between the resonator and ground to suppress RF leakage and preserve the internal quality factor Q_i. (d) Capacitive coupling of the resonator to the transmission line is implemented using an interdigitated structure in a coplanar waveguide (CPW) geometry.

reduced in the tuning range. DC biasing can thus be applied without degrading the internal quality factor Q_i. The narrow strip width is also chosen to minimize flux trapping [168]: below a threshold cooling field $B_{th} \approx \Phi_0/W^2$, magnetic flux is expelled from the strip, maintaining a clean superconducting state [175–177].

The resonator incorporates galvanic connections to a separate ground plane on either side at the voltage nodes of the $3\lambda/4$ resonator. The DC bias current then flows predominantly through the outer trace of the resonator's U-turn section (see Fig. 3.1(b)), corresponding to the $\lambda/2$ region between two voltage nodes. Along this current path, the kinetic inductance is modulated by the bias current and thereby tunes the resonance frequency, while the central part of the structure mainly contributes to the capacitive response. To prevent signal leakage and avoid associated losses, the resonator is connected to ground through a high-impedance filter, as shown in Fig. 3.1(c) that blocks RF signals but allows DC current flow.

For resonance characterization and tunability measurements, the resonator is capacitively coupled to a transmission line using an interdigitated capacitor. The grAl ground plane integrates two functional regions: first, a fractalized structure similar to that of the resonator, and second, a web-like mesh designed to pin vortices [168, 175].

3.3 Chip and Sample Box Design

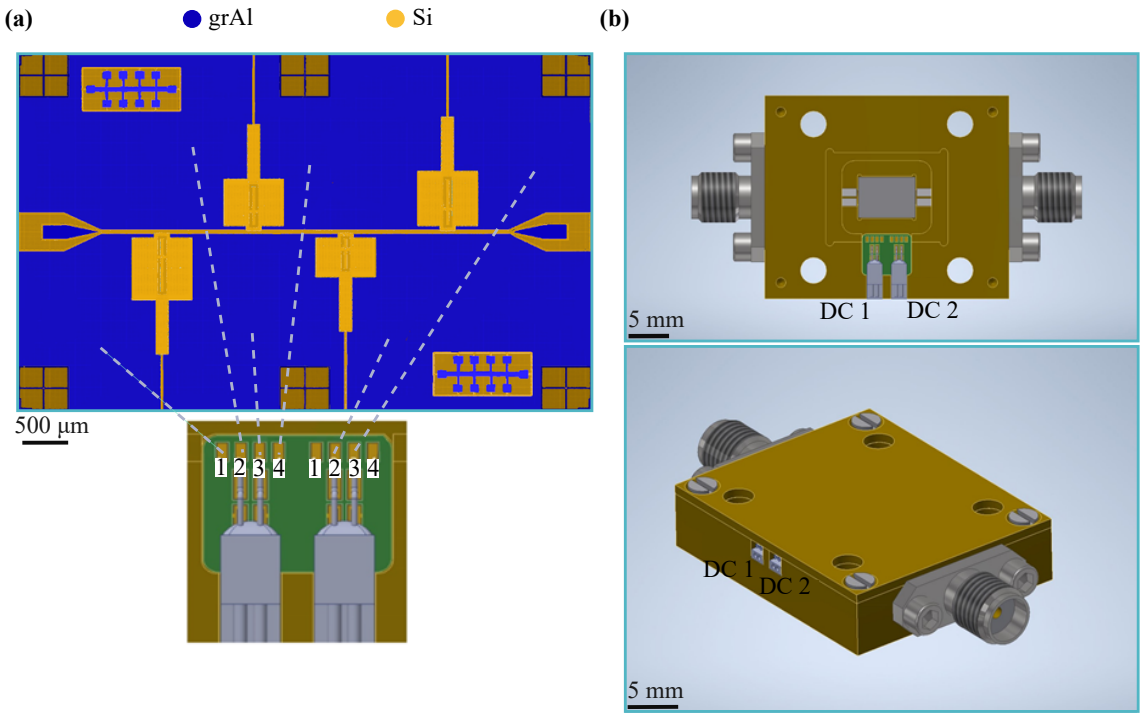

Figure 3.2: Chip and Sample Box for DC-Tunable Fractal Resonators. (a) Optical image of the chip showing four DC-tunable fractal resonators made of granular aluminum on a high-resistivity silicon substrate. Each resonator is designed with a different number of fractal sections to achieve distinct resonance frequencies. DC is injected through aluminum wire bonds connected to the ground planes surrounding each resonator. (b) Image of the sample box made from gold-plated oxygen-free high-conductivity (OFHC) copper, providing good thermal conductivity. A printed circuit board (PCB) inside the box includes two 4-pin DC connectors. These connectors allow DC current to be injected into the chip's ground plane via wire bonds, enabling current injection into the resonators for frequency tuning.

Each chip consists of four grAl resonators fabricated on a high-resistivity silicon substrate (Fig. 3.2(a)). By adjusting the number of fractalized sections, we design the resonators to resonate at different frequencies within a target range suited to the experimental setup.

The chip is mounted inside a sample box (see Fig. 3.2(b), the image is provided by LNF) made of gold-plated oxygen-free high-conductivity (OFHC) copper, providing good thermal anchoring and electromagnetic shielding. For DC biasing, the sample box integrates a printed circuit board (PCB) with two 4-pin DC connectors, which interface with the chip's ground plane via aluminum wire bonds, allowing current biasing of the resonators.

This design provides a flexible platform for exploring the kinetic inductance nonlinearity of grAl, enabling frequency tunability through current biasing. By adjusting the film resistivity and geometry, the device performance, including tunability, characteristic current I^*, and critical current, can be optimized for applications such as broadband phase shifters and parametric amplifiers.

3.4 Fabrication Process

To deposit grAl, a 2-inch silicon wafer is transferred to a UHV Plassys e-beam evaporator in the KIT cleanroom. After plasma cleaning with an Ar/O_2 descum process, titanium is first evaporated as a getter material to improve vacuum conditions, with the shutter being closed to shield the sample during this step. A grAl film with 25 nm thickness is then deposited at room temperature by e-beam evaporation of pure aluminum, while a small oxygen flow is introduced into the chamber to control the aluminum oxidation and tune the kinetic inductance.

Two fabrication approaches are explored, wet etching and lift-off. The wet-etched sample, for which a grAl film with inductance per square of approximately 90 pH/□ was used, suffered from rough edges and limited reproducibility. To address these issues, we shift to a lift-off process for the remaining samples. Lift-off devices have smoother edges and better-defined geometries. For these samples, we use grAl films with an inductance per square of around 41 and 50 pH/□. Notably, the fabricated resonators have a linewidth of 1 μm.

3.5 Measurement Setup and Results

All measurements are done during an internship at Low Noise Factory (LNF) in Gothenburg. The experiments are installed in a dilution refrigerator operating with a base temperature of approximately 20 mK. A vector network analyzer (VNA) generates the input signal, which is transmitted to the device through cables attenuated at various cryogenic stages. The

transmitted output passes through a high-pass filter, a low-pass filter, a circulator/isolator for direction control, and two isolators before reaching a low-noise high electron mobility transistor (HEMT) amplifier mounted at the 4 K stage. The amplified signal is then sent to a room-temperature amplifier before returning to the VNA. For DC biasing, DC wires are attached to the device via two 4-pin DC connectors mounted on the sample box. This configuration allows independent control of the DC, connected externally to the current supply.

To examine how the resonance frequency of the grAl tuning fork resonators change with current, we measure S_{21} of the transmission line as a function of DC for three different samples with inductance values of 41, 50, and 92 pH/□. The resonance frequency f_0 shifts to lower values with increasing current, and above certain I values, the resonance vanishes, indicating the transition out of the superconducting regime. We assume that this current is the critical current I_c.

3.6 Theoretical Modeling of Kinetic Inductance Versus Current Using Ginzburg-Landau Theory

As a first step, to understand nonlinearity and theoretically investigate the behavior of kinetic inductance L_k as a function of current, we consider a model derived from Ginzburg-Landau (GL) theory. Note that it is strictly only valid under the assumption that the temperature T is sufficiently near the critical temperature T_c [28], which is not really the case in the measurements presented in this chapter. Nevertheless, the derived expression for $L_k(I)$ still captures the functional dependence and turns out to fit experiments quite well. The following equations are extracted from Ref. [178], providing an analytical framework under the assumption of a thin-film geometry, where the thickness and width are both smaller than the magnetic penetration depth λ and the coherence length ξ, resulting in a uniform supercurrent density in the wire.

The following expression for the supercurrent density j_s can be derived from GL theory by minimizing the free energy with respect to the supercurrent velocity [28, 178]

$$j_s = 2en_0 \left(1 - \left(\frac{\xi(T) m v_s}{\hbar}\right)^2\right) v_s, \tag{3.1}$$

where n_0 is the Cooper pair density at $I = T = 0$, $\xi(T)$ is the coherence length, $2m$ is the Cooper pair mass, $\hbar$ is the reduced Planck constant, and v_s is the Cooper pairs velocity.

From $v_s = \hbar k/2m$ and $\gamma = kl$, where k is the magnitude of the Cooper pair wave vector and γ is the total phase difference along the nanowire, the supercurrent I_s can be expressed as

$$I_s = \frac{e\hbar}{m}\left(\frac{A}{l}\right) n_0 \left(\gamma - \frac{\xi^2\gamma^3}{l^2}\right), \tag{3.2}$$

where A is the cross-sectional area, l is the device length.

For low frequencies when the signal is slow enough for Cooper pairs and quasiparticles to stay near equilibrium, we can use the second Josephson relation in the form $2eV/\hbar = d\gamma/dt$, to relate the γ to L_k using the relation $V = L_k dI_s/dt$ and Eq. (3.2). The kinetic inductance derived in this way is

$$L_k = \mu_0\lambda^2\left(\frac{l}{A}\right)\left(\frac{1}{1-3k^2\xi^2}\right), \tag{3.3}$$

where

$$\lambda^2(T) = \frac{m}{2\mu_0 n_s(T)e^2}, \tag{3.4}$$

with $n_s(T)$ as the Cooper pair density at temperature T. As derived in Ref. [28], the following equation relates the bias current to ξ and k

$$\frac{I}{I_c} = \frac{3\sqrt{3}}{2}(k\xi - k^3\xi^3). \tag{3.5}$$

Eqs. (3.3) and (3.5) can be solved numerically to give L_k as a function of I. Assuming small bias currents, $I \ll I_c$, the normalized bias current is

$$\frac{I}{I_c} \approx \frac{3\sqrt{3}}{2}(\xi k). \tag{3.6}$$

This expression can be directly substituted into the kinetic inductance expression. By applying a Taylor expansion, we get

$$\frac{L_k(I)}{L_k(0)} \approx 1 + \left(\frac{I}{1.5I_c}\right)^2 + \left(\frac{I}{1.32I_c}\right)^4 + \ldots, \tag{3.7}$$

where $L_k(0)$ is the zero-current kinetic inductance. This is similar to the result for L_k in Ref. [179].

The frequency shift Δf of the resonator, assuming a high kinetic inductance ratio,

$$\Delta f(I) \approx \frac{1}{2\pi\sqrt{(L_g + L_k(I))C}} - \frac{1}{2\pi\sqrt{(L_g + L_k(0))C}} \approx \frac{1}{2\pi\sqrt{L_k(I)C}} - \frac{1}{2\pi\sqrt{L_k(0)C}} \tag{3.8}$$

can thus be modeled with the following equation

$$\Delta f(I) \approx f_0 \left(\frac{1}{\sqrt{1 + \frac{I^2}{(1.5I_c)^2} + \frac{I^4}{(1.32I_c)^4}}} - 1 \right). \tag{3.9}$$

3.7 Theoretical Modeling of Kinetic Inductance Versus Current Using Mattis–Bardeen–BCS

The previous approach relied on assumptions, particularly T close to T_c, which are not fully valid under our measurement conditions. Therefore, we proceed with a more general approach based on BCS theory. The following equations are taken from Ref. [180].

To start, according to Mattis–Bardeen theory [28] at low frequency ($hf \ll k_B T_c$), the normalized imaginary conductivity is given by

$$\frac{\sigma_2}{\sigma_n} = \frac{\pi\Delta}{hf} \tanh\left(\frac{\Delta}{2k_B T}\right), \tag{3.10}$$

where σ_2 is the imaginary conductivity, σ_n the normal-state conductivity, Δ the superconducting energy gap, h Planck's constant, f the frequency, k_B Boltzmann's constant, and T the temperature [28].

Knowing that the imaginary part of the surface impedance is

$$\Im(Z) = \frac{1}{\sigma_2 t} = \omega L_k^{\square}, \tag{3.11}$$

where t is the thickness, we can write the kinetic inductance as

$$L_k = \left(\frac{l}{w}\right) \frac{R_n^{\square} h}{2\pi^2 \Delta} \frac{1}{\tanh\left(\frac{\Delta}{2k_B T}\right)}, \tag{3.12}$$

where l and w are the length and width of the superconducting line, and $R_{\mathrm{n}}^{\square}$ is the sheet resistance.

The dependence of Δ on bias current is complicated in general. In the zero temperature limit we can deduce from Eq. (3.12) that [180]

$$\frac{L_{\mathrm{k}}(I)}{L_{\mathrm{k}}(0)} = \frac{\Delta_{00}}{\Delta}, \tag{3.13}$$

where Δ_{00} is the energy gap at zero temperature and zero bias current. Additionally, assuming that we are in the dirty limit, the energy gap and normalized current are expressed as [180, 181]

$$\Delta = \Delta_{00} e^{-\pi\zeta/4}, \tag{3.14}$$

$$\frac{I}{I_{\mathrm{c}}} = 1.897 e^{-3\pi\zeta/8}\sqrt{\zeta}\left(\frac{\pi}{2} - \frac{2}{3}\zeta\right), \tag{3.15}$$

where

$$\zeta = \frac{Dk^2}{2\Delta}, \tag{3.16}$$

and D is the diffusion coefficient.

Assuming $\zeta \ll 1$ (valid at low currents), and performing a Taylor expansion of Eq. (3.15) around $\zeta = 0$, we can invert the equation keeping only the leading order term

$$\zeta \approx \left(\frac{I}{2.98\ I_c}\right)^2. \tag{3.17}$$

Substituting Eq. (3.17) back into Eq. (3.14) and Eq. (3.13), and then again applying a Taylor expansion, we can express the bias current-dependent kinetic inductance as

$$\frac{L_{\mathrm{k}}(I)}{L_{\mathrm{k}}(0)} \approx 1 + \frac{\pi}{4}\left(\frac{I}{2.98 I_{\mathrm{c}}}\right)^2 + \frac{\pi^2}{32}\left(\frac{I}{2.98 I_{\mathrm{c}}}\right)^4 + \dots. \tag{3.18}$$

or

$$\frac{L_{\mathrm{k}}(I)}{L_{\mathrm{k}}(0)} \approx 1 + \left(\frac{I}{3.36 I_{\mathrm{c}}}\right)^2 + \left(\frac{I}{4 I_{\mathrm{c}}}\right)^4 + \dots. \tag{3.19}$$

Note that the coefficient of the critical current predicted here with BCS is more than double the value predicted by GL. Although derived under the small-current approximation, the general quadratic dependence on bias current reasonably fits reported experimental data in the literature [111, 149, 161, 172, 174].

3.8 Theoretical Modeling of Kinetic Inductance Versus Current Using a Josephson Junction Array Model

A simpler way to estimate how the kinetic inductance of granular aluminum depends on current is to model the material as a one-dimensional array of Josephson junctions. This approach, used in Ref. [106], assumes that grAl behaves like a chain of weakly coupled superconducting grains, where each junction obeys the standard Josephson current-phase relation

$$I = I_c \sin(\phi). \tag{3.20}$$

Here, I is the current through the junction, I_c is the critical current, and ϕ is the phase difference across the junction. Taking the time derivative and comparing it to the second Josephson equation $d\phi/dt = 2\pi/\Phi_0 V$, where V is the voltage across the junction, reveals the nonlinear inductance L_J of the Josephson Junction

$$\frac{dI}{dt} = I_\mathrm{c}\cos(\phi)\frac{d\phi}{dt} = I_\mathrm{c}\cos(\phi)\frac{2\pi}{\Phi_0}V = \frac{1}{L_\mathrm{J}}V. \tag{3.21}$$

The inductance of a single Josephson Junction is

$$L_\mathrm{J}(I) = \frac{\Phi_0}{2\pi I_\mathrm{c}\cos(\phi)} = \frac{\Phi_0}{2\pi I_\mathrm{c}}\frac{1}{\sqrt{1-\sin^2(\phi)}} = \frac{\Phi_0}{2\pi I_\mathrm{c}}\frac{1}{\sqrt{1-(I/I_\mathrm{c})^2}}. \tag{3.22}$$

Assuming the applied current is much smaller than the critical current ($I \ll I_\mathrm{c}$), we can apply a Taylor expansion to obtain

$$\frac{L_\mathrm{J}(I)}{L_\mathrm{J}(0)} \approx \frac{L_\mathrm{J}(I)}{\frac{\Phi_0}{2\pi I_\mathrm{c}}} = 1 + \left(\frac{I}{\sqrt{2}\,I_\mathrm{c}}\right)^2 + \left(\frac{I}{\sqrt[4]{8/3}\,I_\mathrm{c}}\right)^4 + \dots. \tag{3.23}$$

This is the result for a single Josephson junction, but this approximates well also the dynamics of a 1D array of junctions in the case of small bias currents. The simplified equation of motion for such a 1D array was derived in reference [106],

$$I_c \frac{\pi^2}{2} \frac{a}{l} \phi(t) + \frac{\hbar}{4e} \left(\frac{l}{a} C_0 + \frac{\pi^2 a}{l} C_J \right) \frac{d^2\phi}{dt^2} = I, \tag{3.24}$$

where here I_c is the critical current of a single junction in the array, a is superconducting section length, l is the total length of the junction array, C_0 the capacitance of each island between junctions to ground and C_J the capacitance of a junction in the array. Comparing this equation to the RCSJ Model in Eq. (1.23), one can deduce (assuming $R = 0$ and $\sin(\phi) \approx \phi$) that the 1D junction array behaves similarly to a single junction but of reduced effective critical current.

The result in Eq. (3.23) shows, to leading order, a quadratic dependence of kinetic inductance on current, similar to the expressions derived using the Mattis–Bardeen–BCS theory in Eq. (3.19) and GL theory in Eq. (3.7).

We can compare the three models by defining characteristic currents I^* and I^{**}, that scale with I_c and determine nonlinearity, in a generalized fitting model

$$\frac{L_k(I)}{L_k(0)} \approx 1 + \left(\frac{I}{I^*} \right)^2 + \left(\frac{I}{I^{**}} \right)^4 + \dots \tag{3.25}$$

leading to

$$\Delta f = f_0 \left(\frac{1}{\sqrt{1 + \left(\frac{I}{I^*}\right)^2 + \left(\frac{I}{I^{**}}\right)^4 + \cdots}} - 1 \right). \tag{3.26}$$

We use this model to fit the frequency shift versus current data (Fig. 3.3) and extract I^* for each resonator (Fig. 3.4(a)), yielding I^* values in the range 109.6 to 414.4 µA for samples with different L_k. Including the second-order term in the fit, the extracted ratio $I^{**}/I^* \approx 0.65$ (see Fig. 3.4(b)). Additionally, we find the highest tunability of 4.54% (see Fig. 3.4(c)) for a sample with $L_k = 41$ pH/□.

As expected from the low-current assumption in deriving $L_k(I)$, the model shows reduced accuracy at higher currents. Including higher-order terms in L_k improves the fit at larger bias currents, consistent with findings in Refs. [138, 163, 182].

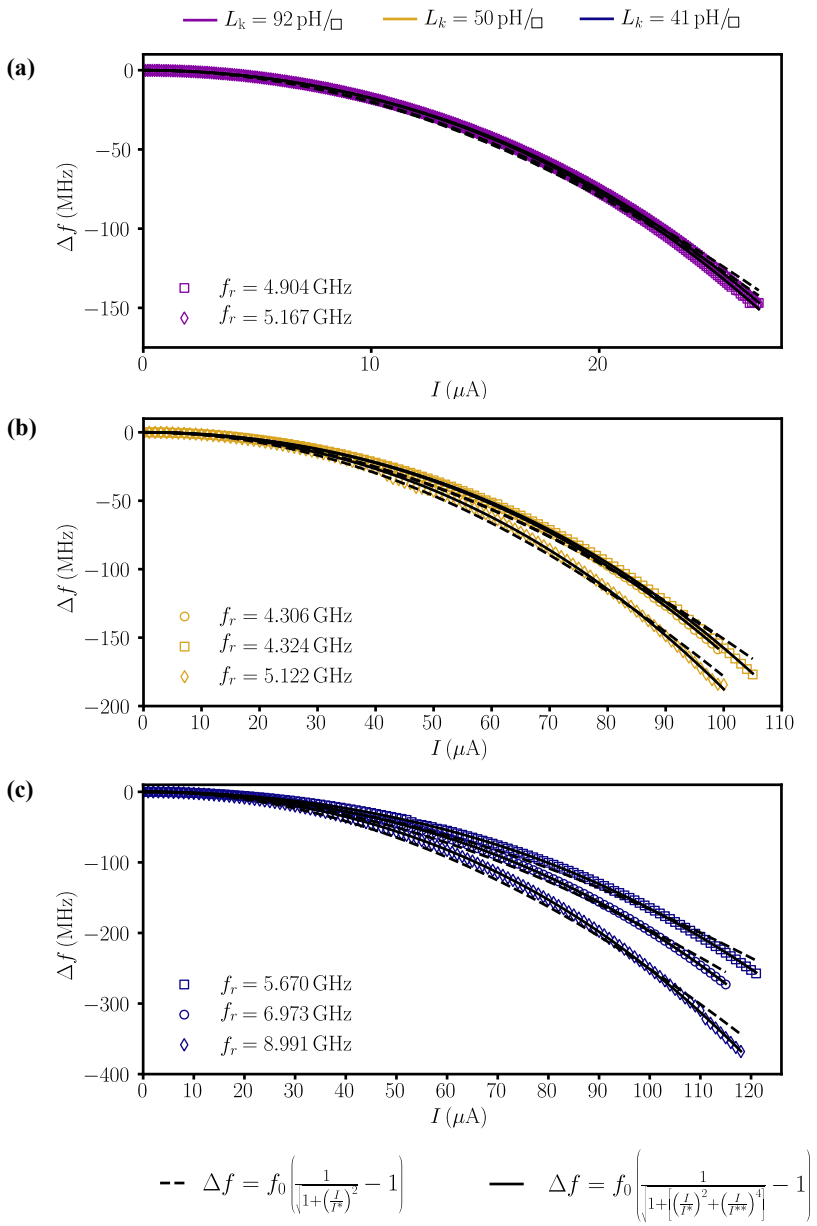

Figure 3.3: Frequency Shift of DC-Biased GrAl Fractal Resonators. (a) Measured frequency shift Δf as a function of applied DC current for fractal resonators with different kinetic inductance per square: $L_{\mathrm{k}}^{\square} = 92$ pH/□ (purple), 50 pH/□ (yellow), and 41 pH/□ (blue). The data are fitted with a nonlinear kinetic inductance model including first-order (dashed lines) and second-order (solid lines) expansions. The first-order model fits well at low currents but deviates at higher currents, consistent with the low-current assumption. The second-order fit improves the agreement at higher currents by introducing an additional fitting parameter.

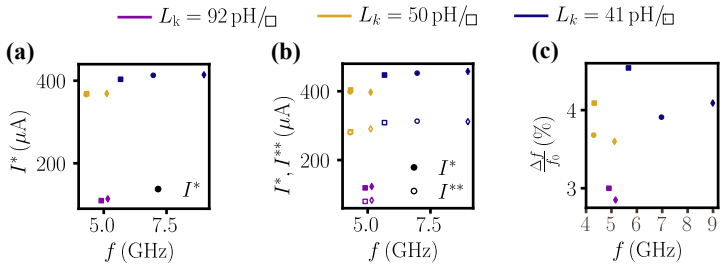

Figure 3.4: Nonlinearity Characterization of DC-Biased GrAl Fractal Resonators. (a) Extracted characteristic current I^* as a function of resonance frequency, obtained from fitting to the first-order model, Eq. (3.26). We observe I^* values ranging from 109.6 to 414.4 μA, with I^* increasing as $L_\square$ decreases. However, a more solid interpretation of the relationship between I^* and $L_\square$ requires an additional dataset across more devices. (b) Extracted I^* (filled symbols) and I^{**} (open symbols) as a function of resonance frequency from the second-order model, with I^* ranging from 119.1 to 457.6 μA and I^{**} ranging from 79.9 to 331.3 μA across the different $L_\square$. (c) Measured fractional frequency tunability $\Delta f/f_0$ for each resonator. We observe maximum tunability values up to 4.54%, with resonators having lower $L_\square$ exhibiting larger tunability and higher critical currents. Although resonators with lower $L_\square$ achieve larger total tunability, devices with higher $L_\square$ provide stronger tuning efficiency in the low-current regime.

3.9 Noise Spectral Density

We measured the noise spectral density $S(f)$, in units of $\mathrm{Hz}/\sqrt{\mathrm{Hz}}$, for two DC-tunable grAl fractal resonators with different inductance values, as shown in Fig. 3.5(a). The measurements were obtained from time-domain traces of the resonator frequency, following the method described in Ref. [125] to extract $S(f)$.

The noise level at 10 Hz is found to be in the range of 100–300 $\mathrm{Hz}/\sqrt{\mathrm{Hz}}$, comparable to the values observed for ring resonators in the second chapter of this thesis for the sample with the lowest resistivity ($\rho = 800\,\mu\Omega \cdot \mathrm{cm}$). At higher frequencies, the spectrum flattens, corresponding to a white noise floor dominated by instrumental noise.

3.10 Quality Factor

The intrinsic quality factor Q_i of the resonators is measured as a function of the average photon number $\bar{n}$, as shown in Fig. 3.5(b). We tested four resonators with two different kinetic inductance per square values and coupling strengths. The internal quality factors are around 10^4 in the single-photon regime. This is about one order of magnitude lower than typical values reported for grAl films [127]. We observe that Q_i increases with photon number, suggesting power-dependent loss mechanisms are involved. Overall, these results

show that while added design complexity, such as additional DC bias lines, galvanic connections to ground, DC-induced currents, and compact fractal geometries, slightly reduces the quality factor, the resonators remain suitable for nonlinear quantum circuits and parametric amplification.

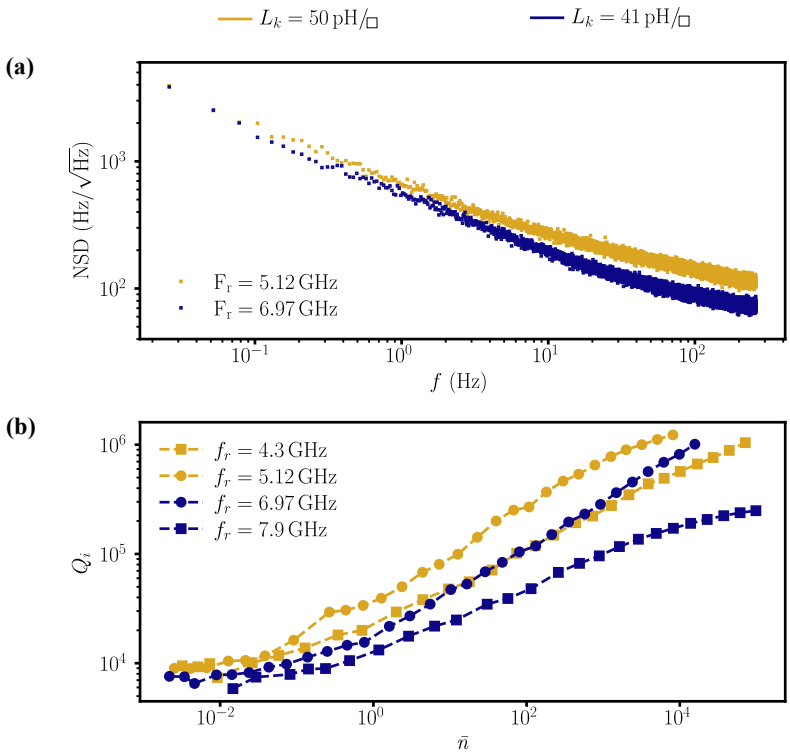

Figure 3.5: Noise Performance and Quality Factor of DC-Tunable GrAl Fractal Resonators. (a) Frequency noise spectral density $S(f)$ as a function of Fourier frequency f, extracted from time-domain traces of the resonator frequency. The noise level at 10 Hz is measured between 100–300 Hz/$\sqrt{\mathrm{Hz}}$. (b) Intrinsic quality factor Q_i as a function of average photon number $\bar{n}$ for resonators with $L_\square = 41$ pH/$\square$ (blue) and $L_\square = 50$ pH/$\square$ (yellow). The average photon number is calculated using $\bar{n} = 2Q_l^2 P_\mathrm{cold}/(Q_c \hbar \omega_0^2)$ where P_cold is the incident microwave power at the device. The error from Fano interference [128] for these strongly coupled resonators is not plotted here because the Fano error becomes large and diverges at higher photon numbers.

3.11 Design of $\lambda/4$ Resonators to Find Sheet Inductance

This section explains how we extract the sheet inductance of the grAl film used in our devices.

We use a chip that has six $\lambda/4$ (quarter-wave) CPW resonators with different lengths. The chip is fabricated on a silicon substrate and includes a grAl ground plane and a CPW transmission line, as shown in Fig. 3.6(a,b).

By measuring the resonators, we extract the resonance frequency of each one. Since the physical lengths of the resonators are different, each one resonates at a different frequency. By comparing the measured frequencies to the known resonator lengths, we fit the data to determine the effective inductance per square.

The $\lambda/4$ resonators are fabricated on the same wafer as the main DC-tunable resonator chips. This ensures that both chips have nearly identical grAl film properties, including resistivity and sheet inductance.

The design and calculations used in this method were initially done by David Niepce and are presented in Ref. [183].

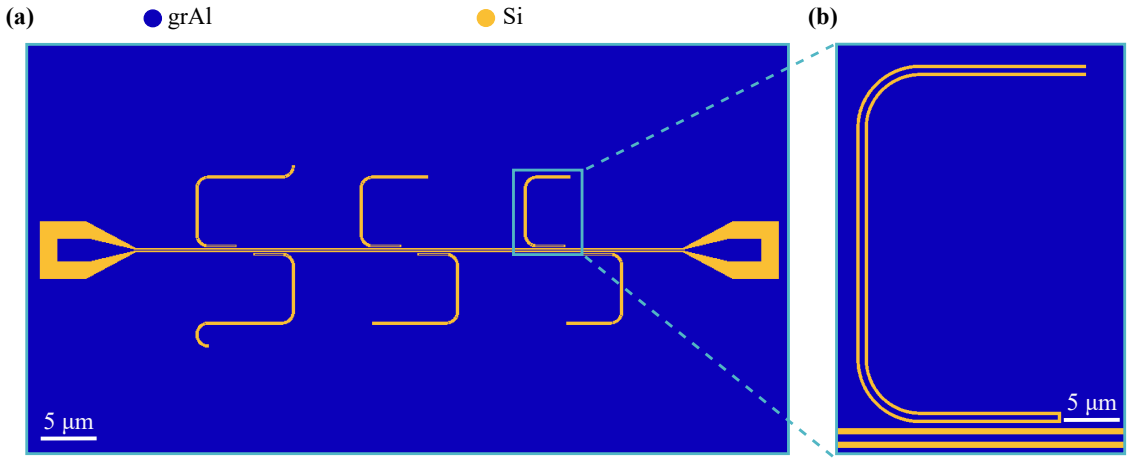

Figure 3.6: Images of the $\lambda/4$ Resonators Chip Used for Sheet Inductance Extraction. (a) Image of the chip showing multiple $\lambda/4$ CPW resonators of varying lengths coupled to a common transmission line. The chip is fabricated on a silicon substrate with a grAl ground plane. (b) Magnified view of one resonator, showing the CPW geometry. These resonators are used to extract the inductance of the grAl film.

To further characterize the performance of the $\lambda/4$ test resonators fabricated for sheet inductance extraction, we measure both their noise spectral density and intrinsic quality factor Q_i, and compare these to those of the DC-tunable $3\lambda/4$ fractal resonators. While a direct comparison is limited due to significant differences in geometry and design, both devices share the same fabrication recipe, the same coplanar waveguide (CPW) architecture, ground plane layout, and measurement setup. This allows for a qualitative insight into how the added complexity in the tunable design may influence performance.

At a frequency of 10 Hz, the $\lambda/4$ resonators exhibit frequency noise spectral density values in the range of 40–80 Hz/$\sqrt{\text{Hz}}$ (as shown in Fig.3.7(a)). These values are lower than the 100–300 Hz/$\sqrt{\text{Hz}}$ measured for the DC-tunable resonators. The precise reason for this reduction in noise remains unclear. However, very likely it is the simpler design of the $\lambda/4$ structures, which lack DC bias lines and additional wire bonds, all of which are required to enable current injection in the tunable devices.

In terms of intrinsic quality factor, the $\lambda/4$ resonators show Q_i values roughly 4 times higher (around 4×10^4, see Fig.3.7(b)) than those of the DC-tunable counterparts (around 1×10^4) in the single-photon regime. Again, this difference could be attributed to the added design elements in the DC-tunable resonators, including more complex geometries, which may introduce additional loss.

We can only hypothesize about the origins of these performance differences: the strong variation in resonator geometry, coupling strength, DC bias circuitry, and mode confinement could all contribute and hence make it difficult to draw firm conclusions. Nevertheless, these observations provide a useful benchmark, suggesting that the special design features required for tunability do not drastically degrade resonator performance, but they result in more noise and a lower quality factor.

Summary

In this work, carried out at Low Noise Factory, we study the tunability of DC-current-biased fractal resonators made from granular aluminum. These resonators exploit the high kinetic inductance and nonlinear properties of grAl to enable frequency tuning via DC bias. We use the design from Ref. [174] and fabricate and test resonators with different inductance-per-square values. The resonators follow a $3\lambda/4$ tuning fork geometry with galvanic ground connections to allow direct current injection.

We measure how the resonance frequency shifts with DC current. We achieve tunability between 2.85% and 4.54% before reaching the critical current. We extract characteristic currents I^*, obtained from the first-order nonlinear model, in the range 109.6 to 414.4 µA for different resonators.

We also measure the noise spectral density $S(f)$. The noise level at 10 Hz ranges from 100 to 300 Hz/$\sqrt{\text{Hz}}$, comparable to the noise measured in Chapter 2 for a ring resonator sample with $\rho = 800\,\mu\Omega \cdot \text{cm}$, and higher than the 40–80 Hz/$\sqrt{\text{Hz}}$ achieved in $\lambda/4$ resonators for similar grAl films. We attribute this increased noise to the design modifications required to enable DC injection into the resonator.

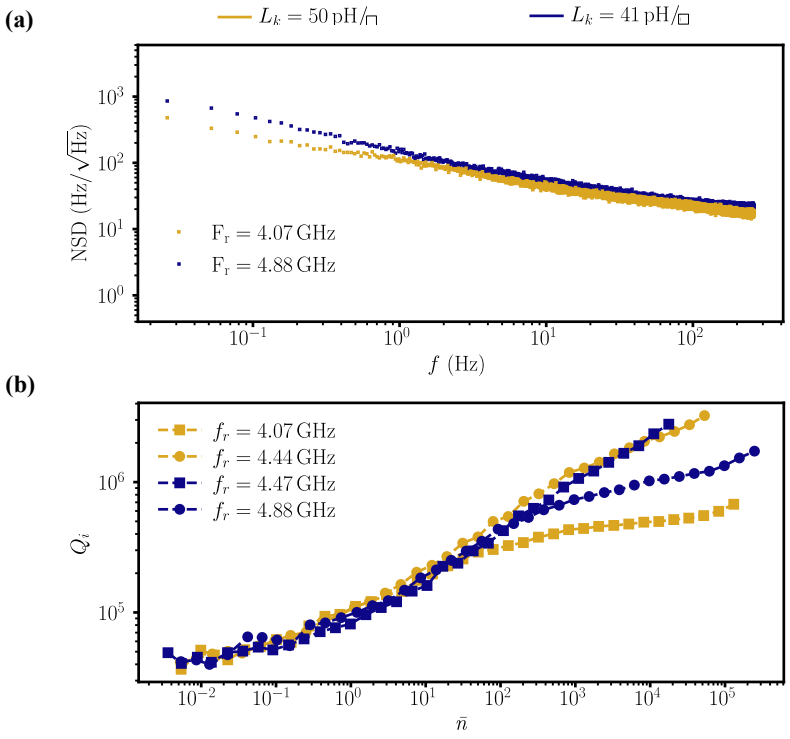

Figure 3.7: Noise Performance and Quality Factor of $\lambda/4$ Test Resonators. (a) Frequency noise spectral density $S(f)$ as a function of frequency f, extracted from time-domain traces of the resonator frequency. The noise level at 10 Hz is between 40–80 Hz/$\sqrt{\mathrm{Hz}}$, which is lower than that observed in the DC-tunable resonators (100–300 Hz/$\sqrt{\mathrm{Hz}}$). These comparisons suggest that the simpler geometry of the $\lambda/4$ resonators may help to reduce noise and improve quality factor, although geometric differences prevent direct conclusions. (b) Intrinsic quality factor Q_i as a function of average photon number $\bar{n}$ for $\lambda/4$ resonators fabricated with $L_\square = 41$ pH/$\square$ (blue) and $L_\square = 50$ pH/$\square$ (yellow), on the same wafer as the DC-tunable devices. The Q_i values are approximately 4×10^4 in the single-photon regime—roughly four times higher than those measured for the DC-tunable resonators.

Finally, we characterize the intrinsic quality factor Q_i as a function of average photon number. We observe $Q_\mathrm{i} \sim 10^4$ in the single-photon regime, about one order of magnitude lower than typical values for grAl films. Even so, the quality factor remains sufficient for applications requiring frequency tunability through DC, such as parametric amplification and nonlinear quantum circuits.

4 Conclusion & Outlook

In this chapter, we summarize the main results of the thesis, which centers on two experimental investigations leveraging the high kinetic inductance of granular aluminum (grAl) for superconducting quantum circuits. The first project focused on the development of compact meandered ring resonators with impedance values exceeding 100 kΩ, achieved through a single-step lift-off e-beam lithography process. The noise and quality factor characterization demonstrates their suitability for use in high-impedance quantum hardware. In the second project, we studied DC-tunable fractal resonators capable of in-situ modulation of resonance frequency via injected direct current. Adapting a $3\lambda/4$ tuning fork design, we achieved tunability of up to 4.54% before reaching the critical current. We used theoretical models to extract characteristic currents and compared them with the observed nonlinear behavior. Noise spectral density and internal quality factor of devices were characterized. The results show that these devices are suitable for applications in three-wave mixing amplifiers and broadband phase shifters.

High-Impedance Meandered Ring Resonators

We utilized the high kinetic inductance of grAl and a compact meandered ring design to make superinductors with characteristic impedances exceeding 100 kΩ—about 16 times the resistance quantum. The design strategy involved maximizing inductance while minimizing self-capacitance. Fabrication was done in a single-step e-beam lithography and lift-off process on sapphire substrates, with characterization performed using a coplanar waveguide (CPW) reflection measurement setup. From finite element simulations and measurements, we extracted inductance per square. We performed measurements across grAl films with different resistivities ranging from 800 μΩ · cm to 2500 μΩ · cm, and for the sample with 670 pH/□ we got total inductance values up to 4 μH, with the highest achieved impedance reaching 127 kΩ. We proposed a compact scaling model showing that impedance scales as $Z \propto \sqrt{r_{\text{in}} L_{\square}/(pw)}$, in agreement with our experimental data.

The ring resonators exhibit internal quality factors $Q_i \sim 10^5$ at the single-photon regime, frequency noise spectral densities between 10^2 to $10^3\,\mathrm{Hz}/\sqrt{\mathrm{Hz}}$ at 10 Hz, and self-Kerr nonlinearities on the order of tens of Hz. The compact design, high impedance, and low dissipation make them highly suitable for use in superconducting circuits.

These properties open up several applications. The large impedance enables large zero-point voltage fluctuations, which are applicable for coupling to systems such as spins in quantum dots or molecular qubits. The large inductive reactance makes them useful in circuits exploring coherent quantum phase slips, such as for observing dual Shapiro steps. The ring design could also be adapted into noise-protected qubit designs. Finally, we observed an unexpected positive frequency shift at low photon numbers in some devices. This effect, possibly caused by interactions with strongly coupled two-level systems, is an interesting direction for further study.

Direct Current Tunable GrAl Resonators

In the second part of this thesis, we introduced a modified resonator geometry based on a $3\lambda/4$ structure that allows direct current injection through the device. The tunable resonators have a fractalized design, resembling a tuning fork, with connections to two separated ground planes via galvanic contact. There, high impedance elements served as filters to suppress RF leakage. The structure allows current biasing of the resonators through wire bonds attached to the two ground planes. The resonators were characterized in transmission via their coupling to a CPW feedline.

By using the current-tunable kinetic inductance of grAl, we achieved in-situ tuning of the resonance frequency up to 4.54% with more than one hundred microamperes of direct current. We compared different analytical models from the literature and used them to fit the measured frequency shifts. The value of I^* was extracted for several devices with different inductance per square, ranging from approximately 41 pH/□ to 92 pH/□.

These tunable resonators exhibit internal quality factors around $Q_i \sim 10^4$ at single-photon regime with noise levels between 100 and $300\,\mathrm{Hz}/\sqrt{\mathrm{Hz}}$ at 10 Hz, indicating that their performance is sufficient for applications requiring frequency tunability, such as phase shifters and three-wave mixing parametric amplifiers.

Future improvements could include the implementation of transmission lines and coupling elements from standard superconductors such as Nb or Al instead of grAl. This would reduce the effect of current-induced resistivity changes in grAl and allow characterization of power-dependent loss and nonlinearity at different currents. Additionally, exploring

grAl fabricated via sputtering and using films with different resistivity ranges may offer new insights into the tunability of kinetic inductance in grAl.

Appendix

A Wet Etching Fabrication Process

The process of e-beam lithography followed by wet etching is tested as a first approach to fabricate 100 nm resolution granular aluminum (grAl) structures. The etching recipe is learned from Carlo Ciaccia and is based on techniques developed in the group of Christian Schönenberger.

The process begins with the deposition of the grAl film. First, the substrate undergoes plasma cleaning in an Ar/O_2 environment (10 sccm/5 sccm) using a Kaufman ion source with beam parameters of $U_{\text{beam}} = 200\,\text{V}$ and $I_{\text{beam}} = 10\,\text{mA}$. Titanium is then evaporated at a rate of 0.2 nm/s for 2 min, with the shutter closed, to work as a getter and improve vacuum conditions. Subsequently, pure aluminum is evaporated at room temperature at a rate of 1 nm/s under a dynamic oxygen atmosphere with pressure ranging from 10^{-5} to 10^{-4} mbar, forming the disordered granular aluminum film.

After deposition, the negative resist ma-N 2403 is spin-coated onto the grAl-coated substrate. The resist is spun at 3000 rpm for 65 s with an acceleration of 1000 rpm/s, followed by baking at 90 °C for 60 s. After e-beam exposure, the resist is developed in ma-D377 for (10 ± 3) s. Patterning is done using a wet etching step. The sample is immersed in heated Transene D etchant at 50 °C for a controlled time, followed by a stop bath in water at 50 °C and rinsing in room-temperature water for 40 s.

SEM images of the resulting structures show that for 100 nm wide lines, the process leads to rough edges (see Fig. A.1a and b). As a result, this method is not used for fabricating the high-resolution grAl resonators discussed in Chapter 2. However, for larger features—especially at the micrometer scale—the process gives smooth and well-defined edges.

Table A.1: Summary of Fabrication Parameters for the E-Beam Lithography Followed by Wet Etching Process of GrAl. The process includes initial plasma cleaning, titanium gettering, aluminum evaporation in a dynamic oxygen environment, and wet etching after e-beam lithography using negative resist.

Substrate and Film Deposition	
Substrate	C-plane sapphire (330 µm, double-side polished)
Plasma Cleaning	
Gas flow	O_2/Ar (10 sccm/5 sccm)
Beam parameters	$U_{\text{beam}} = 200\,\text{V}$, $I_{\text{beam}} = 10\,\text{mA}$
Gettering	
Ti evaporation rate	0.2 nm/s for 2 min (shutter closed)
grAl Deposition	
Al evaporation rate	1 nm/s
O_2 pressure	10^{-5} to 10^{-4} mbar
Resist Coating and E-Beam Lithography	
Resist	ma-N 2403
Spin speed	3000 rpm for 65 s
Acceleration	1000 rpm/s
Bake	90 °C for 60 s
Development	
Developer	ma-D377 for (10 ± 3) s
Etching	
Etchant	Transene D
Etch temperature	50 °C
Stop bath	Water at 50 °C (a few seconds)
Rinse	Water at room temperature for 40 s

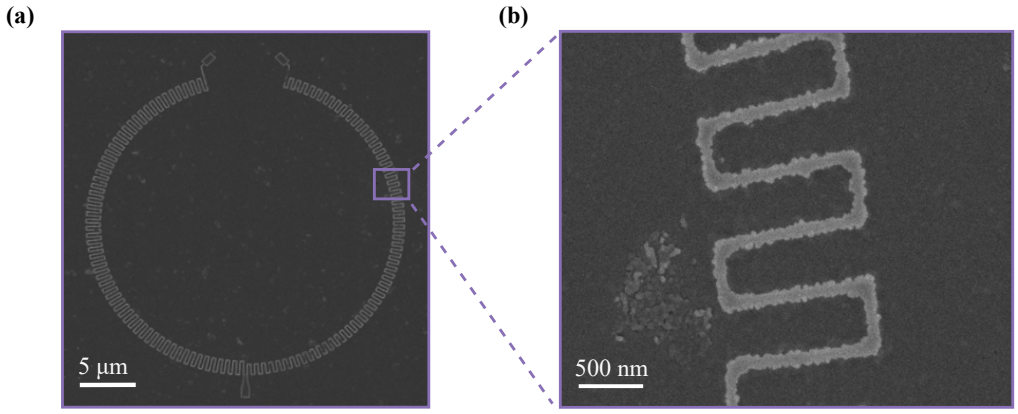

Figure A.1: Etched GrAl Ring Resonators. SEM images of granular aluminum ring resonators fabricated using the wet etching process described in Appendix A. (a) Overview of a full ring structure with a linewidth of approximately 100 nm. (b) Zoomed-in view of a smaller segment showing the edge roughness from the etching process, which is a limiting factor for applications requiring sub-100 nm precision.

B Dry Etching Fabrication Process

We test a dry etching approach using inductively coupled plasma (ICP) and reactive ion etching (RIE) to explore alternatives to lift-off lithography for fabricating 100 nm resolution grAl structures. The resist coating and aluminum deposition steps follow the same procedure described in Appendix A, using ma-N 2403 as the negative e-beam resist and grAl deposition by e-beam evaporation.

The resist is developed in ma-D377 for approximately (10 ± 3) seconds, followed by a stop bath in water and nitrogen blow-drying. Etching is performed in an ICP chamber using a chlorine-based recipe (HR-Ar-Cl, Cl_2/Ar = 20/1 sccm), which enables anisotropic etching of the grAl film.

While the process successfully removes unmasked grAl and defines the pattern, we observe the appearance of "fences"—residual edge build-ups—along the etched lines in several structures (Fig. B.1(a)). These fences are likely caused by aluminum redeposition or the formation of compounds involving aluminum, chlorine, and potentially resist material. Although clean structures are occasionally observed—such as the example on the right in Fig. B.1(b)—it remains unclear whether these results are from over-etching (which may also remove resist and film underneath) or a fortunate suppression of fence formation. In its current state, the presence of fences limits the reliability and reproducibility of this method.

Further optimization is needed to improve the process. Potential strategies include:

- Regulating the substrate temperature during etching,
- Identifying the chemical origin of the fence material,
- Testing alternative masking materials,
- Finding post-etch cleaning steps that selectively remove fences without damaging the grAl film.

Moreover, the resist itself is etched during the chlorine-based ICP process. This poses a challenge in terms of aspect ratios: if the resist is too thin, it erodes quickly and fails to adequately protect the grAl underneath. For instance, a 20 nm-thick grAl layer remains unetched when covered by a 100 nm resist cap prior to resist removal.

We also test RIE using a fluorocarbon-based recipe (CF_4/CHF_3 = 30/20 sccm, 250 W, 25 mTorr chamber pressure), but it fails to etch the grAl while rapidly removing the resist, leaving the metal layer largely intact.

We hope that future studies will build on these results and develop a reproducible dry etching process for high-resolution grAl nanostructures. Fingers crossed for the next generation of students.

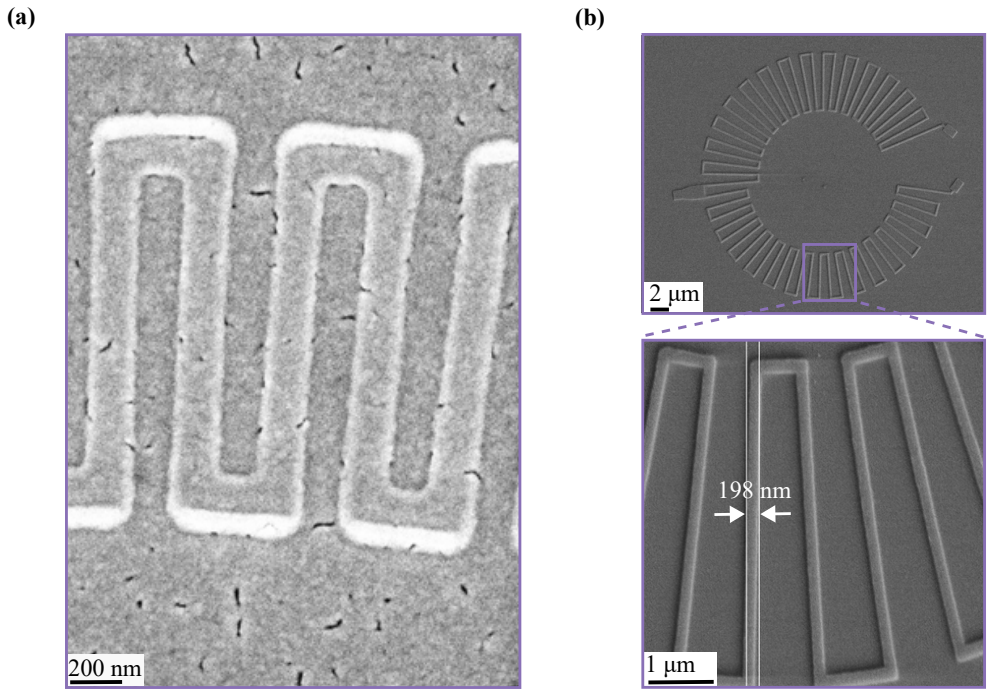

Figure B.1: SEM Images of GrAl Structures After ICP Dry Etching. (a) SEM image of a grAl line showing visible fences along the edges. The exact origin of these features is not yet fully understood. The linewidth measures approximately 200 nm, and irregular edge residues are clearly visible along both sidewalls. (b) SEM image of a different structure, along with its magnified view, showing a clean grAl pattern with no visible fence residues. However, such clean outcomes are not consistently reproducible.

Table B.1: Summary of Fabrication Parameters for the ICP Dry Etching Process Applied to GrAl Structures. The process shows promise but is currently limited by edge fences and etch-resist compatibility.

Resist Coating and Development	
Resist	ma-N 2403
Spin speed	3000 rpm for 65 s
Acceleration	1000 rpm/s
Bake	90 °C for 60 s
Developer	ma-D377 for (10 ± 3) s
Stop bath	Water, blow-dry with nitrogen
ICP Etching Process	
Etch chemistry	Cl_2/Ar = 20/1 sccm (HR-Ar-Cl)
Chamber	ICP system
Issue	Fences along etched edges
Aspect ratio limitation	20 nm grAl not etched under 100 nm resist
Resist Removal	
Solvent	NEP (N-Ethyl-2-pyrrolidone)
Temperature	90 °C
Duration	2 hours
Alternative Etch Test (RIE)	
Recipe	CF_4/CHF_3 = 30/20 sccm, 250 W, 25 mTorr
Observation	Resist removed, grAl remained mostly intact

Bibliography

[1] M. Khorramshahi, M. Spiecker, P. Paluch, S. Geisert, N. Gosling, N. Zapata, L. Brauch, C. Kübel, S. Dehm, R. Krupke, W. Wernsdorfer, I. M. Pop, and T. Reisinger, "High Impedance Granular Aluminum Ring Resonators", Phys. Rev. Appl. **24**, 024066 (2025).

[2] M. De Lucia, M. Khorramshahi, T. Reisinger, I. M. Pop, and G. Ulbricht, "Measurement of Optical Absorption in Granular Aluminum Thin Films at Room Temperature", Appl. Phys. B **131**, 157 (2025).

[3] D. P. DiVincenzo, "The physical implementation of quantum computation", Fortschritte der Physik **48**, 771–783 (2000) (cit. on p. 2).

[4] J. Benhelm, G. Kirchmair, C. F. Roos, and R. Blatt, "Towards fault-tolerant quantum computing with trapped ions", Nature Physics **4**, 463–466 (2008) (cit. on p. 2).

[5] C. D. Bruzewicz, J. Chiaverini, R. McConnell, and J. M. Sage, "Trapped-ion quantum computing: Progress and challenges", Applied Physics Reviews **6**, 021314 (2019) (cit. on p. 2).

[6] C. Monroe, W. C. Campbell, L.-M. Duan, Z.-X. Gong, A. V. Gorshkov, P. W. Hess, R. Islam, K. Kim, N. M. Linke, G. Pagano, P. Richerme, C. Senko, and N. Y. Yao, "Programmable quantum simulations of spin systems with trapped ions", Reviews of Modern Physics **93**, 025001 (2021) (cit. on p. 2).

[7] M. V. G. Dutt, L. Childress, L. Jiang, E. Togan, J. Maze, F. Jelezko, A. S. Zibrov, P. R. Hemmer, and M. D. Lukin, "Quantum register based on individual electronic and nuclear spin qubits in diamond", Science **316**, 1312–1316 (2007) (cit. on p. 2).

[8] V. Gareyan and Zh. Gevorkian, "Impact of surface roughness on light absorption", Physical Review A **109**, 013515 (2024) (cit. on p. 2).

[9] B. E. Kane, "A silicon-based nuclear spin quantum computer", Nature **393**, 133–137 (1998) (cit. on p. 2).

[10] A. Chatterjee, P. Stevenson, S. De Franceschi, A. Morello, N. P. de Leon, and F. Kuemmeth, "Semiconductor qubits in practice", Nature Reviews Physics **3**, 157–177 (2021) (cit. on p. 2).

[11] L. Bogani and W. Wernsdorfer, "Molecular spintronics using single-molecule magnets", Nature Materials **7**, 179–186 (2008) (cit. on p. 2).

[12] M. Shiddiq, D. Komijani, Y. Duan, A. Gaita-Ariño, E. Coronado, and S. Hill, "Enhancing coherence in molecular spin qubits via atomic clock transitions", Nature **531**, 348–351 (2016) (cit. on p. 2).

[13] E. Moreno-Pineda and W. Wernsdorfer, "Measuring molecular magnets for quantum technologies", Nature Reviews Physics **3**, 645–659 (2021) (cit. on p. 2).

[14] Y. Nakamura, Yu. A. Pashkin, and J. S. Tsai, "Coherent control of macroscopic quantum states in a single-Cooper-pair box", Nature **398**, 786–788 (1999) (cit. on p. 2).

[15] F. Arute, K. Arya, R. Babbush, D. Bacon, J. C. Bardin, R. Barends, R. Biswas, S. Boixo, F. G. S. L. Brandao, D. A. Buell, B. Burkett, Y. Chen, Z. Chen, B. Chiaro, R. Collins, W. Courtney, A. Dunsworth, E. Farhi, B. Foxen, A. Fowler, C. Gidney, M. Giustina, R. Graff, K. Guerin, S. Habegger, M. P. Harrigan, M. J. Hartmann, A. Ho, M. Hoffmann, T. Huang, T. S. Humble, S. V. Isakov, E. Jeffrey, Z. Jiang, D. Kafri, K. Kechedzhi, J. Kelly, P. V. Klimov, S. Knysh, A. Korotkov, F. Kostritsa, D. Landhuis, M. Lindmark, E. Lucero, D. Lyakh, S. Mandrà, J. R. McClean, M. McEwen, A. Megrant, X. Mi, K. Michielsen, M. Mohseni, J. Mutus, O. Naaman, M. Neeley, C. Neill, M. Y. Niu, E. Ostby, A. Petukhov, J. C. Platt, C. Quintana, E. G. Rieffel, P. Roushan, N. C. Rubin, D. Sank, K. J. Satzinger, V. Smelyanskiy, K. J. Sung, M. D. Trevithick, A. Vainsencher, B. Villalonga, T. White, Z. J. Yao, P. Yeh, A. Zalcman, H. Neven, and J. M. Martinis, "Quantum supremacy using a programmable superconducting processor", Nature **574**, 505–510 (2019) (cit. on p. 2).

[16] P. Krantz, M. Kjaergaard, F. Yan, T. P. Orlando, S. Gustavsson, and W. D. Oliver, "A quantum engineer's guide to superconducting qubits", Applied Physics Reviews **6**, 021318 (2019) (cit. on p. 2).

[17] M. Kjaergaard, M. E. Schwartz, J. Braumüller, P. Krantz, J. I.-J. Wang, S. Gustavsson, and W. D. Oliver, "Superconducting Qubits: Current State of Play", Annual Review of Condensed Matter Physics **11**, 369–395 (2020) (cit. on p. 2).

[18] A. Blais, S. M. Girvin, and W. D. Oliver, "Quantum information processing and quantum optics with circuit quantum electrodynamics", Nature Physics **16**, 247–256 (2020) (cit. on p. 2).

[19] M. McEwen, K. C. Miao, J. Atalaya, A. Bilmes, A. Crook, J. Bovaird, J. M. Kreikebaum, N. Zobrist, E. Jeffrey, B. Ying, A. Bengtsson, H.-S. Chang, A. Dunsworth, J. Kelly, Y. Zhang, E. Forati, R. Acharya, J. Iveland, W. Liu, S. Kim, B. Burkett, A. Megrant, Y. Chen, C. Neill, D. Sank, M. Devoret, and A. Opremcak, "Resisting High-Energy Impact Events through Gap Engineering in Superconducting Qubit Arrays", Physical Review Letters **133**, 240601 (2024) (cit. on p. 3).

[20] Y. S. Weinstein and C. S. Hellberg, "Energetic suppression of decoherence in exchange-only quantum computation", Physical Review A **72**, 022319 (2005) (cit. on p. 3).

[21] P. Winkel, "Design and realization of superconducting circuits for quantum information processing", PhD thesis (Karlsruher Institut für Technologie (KIT), 2020) (cit. on p. 4).

[22] M. Bhattacharya, K. D. Osborn, and A. Mizel, "Jaynes-Cummings treatment of superconducting resonators with dielectric loss due to two-level systems", Physical Review B **84**, 104517 (2011) (cit. on p. 6).

[23] M. H. Devoret, B. Huard, R. Schoelkopf, and L. F. Cugliandolo, *Quantum Machines: Measurement and Control of Engineered Quantum Systems* (Oxford University Press, 2014) (cit. on p. 6).

[24] S. M. Girvin, "Circuit QED: superconducting qubits coupled to microwave photons", in *Quantum Machines: Measurement and Control of Engineered Quantum Systems*, edited by M. Devoret, B. Huard, R. Schoelkopf, and L. F. Cugliandolo, 1st ed. (Oxford University PressOxford, June 12, 2014), pp. 113–256 (cit. on p. 6).

[25] D. M. Pozar, *Microwave engineering*, 4th ed. (Wiley, Chichester, England, UK, Dec. 2011) (cit. on p. 7).

[26] R. Ferraiuolo, G. Serpico, L. Parlato, H. G. Ahmad, D. Massarotti, and D. Montemurro, "Superconducting resonators: a path towards advanced quantum circuits", in 2022 IEEE 15th Workshop on Low Temperature Electronics (WOLTE) (June 2022), pp. 1–4 (cit. on p. 7).

[27] B. Josephson, "Possible new effects in superconductive tunnelling", Physics Letters **1**, 251–253 (1962) (cit. on p. 8).

[28] M. Tinkham, *Introduction to superconductivity* (2004) (cit. on pp. 8, 10, 18, 56–58).

[29] A. A. Golubov, M. Yu. Kupriyanov, and E. Il'ichev, "The current-phase relation in Josephson junctions", Reviews of Modern Physics **76**, 411–469 (2004) (cit. on p. 8).

[30] K. K. Likharev, "Superconducting weak links", Reviews of Modern Physics **51**, 101–159 (1979) (cit. on p. 8).

[31] D. Rieger, S. Günzler, M. Spiecker, P. Paluch, P. Winkel, L. Hahn, J. K. Hohmann, A. Bacher, W. Wernsdorfer, and I. M. Pop, "Granular aluminium nanojunction fluxonium qubit", Nature Materials **22**, 194–199 (2023) (cit. on p. 8).

[32] P. J. Koppinen, T. Kühn, and I. J. Maasilta, "Effects of Charging Energy on SINIS Tunnel Junction Thermometry", Journal of Low Temperature Physics **154**, 179–189 (2009) (cit. on p. 8).

[33] I. Petković, N. M. Chtchelkatchev, and Z. Radović, "Resonant amplification of the Andreev process in ballistic Josephson junctions", Physical Review B **73**, 184510 (2006) (cit. on p. 8).

[34] B. K. Nikolić, J. K. Freericks, and P. Miller, "Equilibrium properties of double-screened dipole-barrier *SINIS* Josephson junctions", Physical Review B **65**, 064529 (2002) (cit. on p. 8).

[35] F. Born, D. Cassel, K. Ilin, A. Klushin, M. Siegel, A. Brinkman, A. Golubov, M. Yu. Kupriyanov, and H. Rogalla, "Transport properties of SINIS junctions with high-current density", IEEE Transactions on Applied Superconductivity **13**, 1079–1084 (2003) (cit. on p. 8).

[36] A. K. Feofanov, V. A. Oboznov, V. V. Bol'ginov, J. Lisenfeld, S. Poletto, V. V. Ryazanov, A. N. Rossolenko, M. Khabipov, D. Balashov, A. B. Zorin, P. N. Dmitriev, V. P. Koshelets, and A. V. Ustinov, "Implementation of Superconductor/Ferromagnet/Superconductor π-Shifters in Superconducting Digital and Quantum Circuits", Nature Physics **6**, 593–597 (2010) (cit. on p. 8).

[37] V. V. Ryazanov, V. A. Oboznov, A. Yu. Rusanov, A. V. Veretennikov, A. A. Golubov, and J. Aarts, "Coupling of Two Superconductors through a Ferromagnet: Evidence for a π Junction", Physical Review Letters **86**, 2427–2430 (2001) (cit. on p. 8).

[38] G. A. Bobkov, I. V. Bobkova, and A. M. Bobkov, "Long-range interaction of magnetic moments in a coupled system of superconductor-ferromagnet-superconductor Josephson junctions with anomalous ground-state phase shift", Physical Review B **105**, 024513 (2022) (cit. on p. 8).

[39] V. M. Krasnov, O. Ericsson, S. Intiso, P. Delsing, V. A. Oboznov, A. S. Prokofiev, and V. V. Ryazanov, "Planar SFS Josephson Junctions Made by Focused Ion Beam Etching", Physica C: Superconductivity **418**, 16–22 (2005) (cit. on p. 8).

[40] B. D. Josephson, "Coupled Superconductors", Reviews of Modern Physics **36**, 216–220 (1964) (cit. on p. 8).

[41] B. Josephson, "Supercurrents through barriers", Advances in Physics **14**, 419–451 (1965) (cit. on p. 8).

[42] M. H. Devoret and R. J. Schoelkopf, “Superconducting circuits for quantum information: An outlook”, Science **339**, 1169–1174 (2013) (cit. on p. 10).

[43] D. V. Averin and K. K. Likharev, “Coulomb blockade of single-electron tunneling, and coherent oscillations in small tunnel junctions”, Journal of Low Temperature Physics **62**, 345–373 (1986) (cit. on p. 10).

[44] W. C. Stewart, “Current-Voltage Characteristics of Josephson Junctions”, Applied Physics Letters **12**, 277–280 (1968) (cit. on p. 10).

[45] D. E. McCumber, “Effect of ac Impedance on dc Voltage-Current Characteristics of Superconductor Weak-Link Junctions”, Journal of Applied Physics **39**, 3113–3118 (1968) (cit. on p. 10).

[46] V. Ambegaokar and B. I. Halperin, “Voltage Due to Thermal Noise in the dc Josephson Effect”, Physical Review Letters **22**, 1364–1366 (1969) (cit. on p. 11).

[47] T. A. Fulton and L. N. Dunkleberger, “Lifetime of the zero-voltage state in Josephson tunnel junctions”, Physical Review B **9**, 4760–4768 (1974) (cit. on p. 11).

[48] J. Tang, M. T. Wei, A. Sharma, E. G. Arnault, A. Seredinski, Y. Mehta, K. Watanabe, T. Taniguchi, F. Amet, and I. Borzenets, “Overdamped phase diffusion in hBN encapsulated graphene Josephson junctions”, Physical Review Research **4**, 023203 (2022) (cit. on p. 11).

[49] V. Lacquaniti, C. Cagliero, S. Maggi, and R. Steni, “Overdamped Nb/Al–AlOx/Nb Josephson junctions”, Applied Physics Letters **86**, 042501 (2005) (cit. on p. 11).

[50] I. E. Tornes, “Topics in the physics of underdamped Josephson systems” (The Ohio State University, 2006) (cit. on p. 11).

[51] J. M. Kivioja, T. E. Nieminen, J. Claudon, O. Buisson, F. W. J. Hekking, and J. P. Pekola, “Observation of Transition from Escape Dynamics to Underdamped Phase Diffusion in a Josephson Junction”, Physical Review Letters **94**, 247002 (2005) (cit. on p. 11).

[52] A. Zazunov, N. Didier, and F. W. J. Hekking, “Quantum charge diffusion in underdamped Josephson junctions and superconducting nanowires”, Europhysics Letters **83**, 47012 (2008) (cit. on p. 11).

[53] H. Kim, G. Jang, S. Jin, D. Shin, H.-J. Shin, J. Luo, I. Siddiqi, Y. Kim, H. H. Yoon, and L. B. Nguyen, *Josephson Junctions in the Age of Quantum Discovery*, (May 19, 2025) `http://arxiv.org/abs/2505.12724` (visited on 05/25/2025) (cit. on p. 11).

[54] V. Lacquaniti, N. De Leo, M. Fretto, and A. Sosso, "Perspectives of Overdamped Josephson Junctions in Voltage Standard Applications", The Open Superconductors Journal **2**, 1–11 (2010) (cit. on p. 11).

[55] M. Devoret, S. Girvin, and R. Schoelkopf, "Circuit-QED: how strong can the coupling between a josephson junction atom and a transmission line resonator Be?", Ann. Phys. **519**, 767–779 (2007) (cit. on pp. 12, 23, 51).

[56] G. Burkard, T. D. Ladd, A. Pan, J. M. Nichol, and J. R. Petta, "Semiconductor spin qubits", Rev. Mod. Phys. **95**, 025003 (2023) (cit. on pp. 12, 13, 23).

[57] P. Arrangoiz-Arriola, E. A. Wollack, M. Pechal, J. D. Witmer, J. T. Hill, and A. H. Safavi-Naeini, "Coupling a superconducting quantum circuit to a phononic crystal defect cavity", Phys. Rev. X **8**, 031007 (2018) (cit. on p. 12).

[58] A. Bozkurt, H. Zhao, C. Joshi, H. G. LeDuc, P. K. Day, and M. Mirhosseini, "A quantum electromechanical interface for long-lived phonons", Nat. Phys. **19**, 1326–1332 (2023) (cit. on p. 12).

[59] A. André, D. DeMille, J. M. Doyle, M. D. Lukin, S. E. Maxwell, P. Rabl, R. J. Schoelkopf, and P. Zoller, "A coherent all-electrical interface between polar molecules and mesoscopic superconducting resonators", Nat. Phys. **2**, 636–642 (2006) (cit. on p. 12).

[60] V. E. Manucharyan, N. A. Masluk, A. Kamal, J. Koch, L. I. Glazman, and M. H. Devoret, "Evidence for coherent quantum phase slips across a Josephson junction array", Phys. Rev. B **85**, 024521 (2012) (cit. on pp. 12, 13, 23).

[61] N. A. Masluk, I. M. Pop, A. Kamal, Z. K. Minev, and M. H. Devoret, "Microwave characterization of josephson junction arrays: implementing a low loss superinductance", Phys. Rev. Lett. **109**, 137002 (2012) (cit. on pp. 12, 13, 23).

[62] V. E. Manucharyan, J. Koch, L. I. Glazman, and M. H. Devoret, "Fluxonium: single cooper-pair circuit free of charge offsets", Science **326**, 113–116 (2009) (cit. on pp. 12, 23).

[63] I. M. Pop, K. Geerlings, G. Catelani, R. J. Schoelkopf, L. I. Glazman, and M. H. Devoret, "Coherent suppression of electromagnetic dissipation due to superconducting quasiparticles", Nature **508**, 369–372 (2014) (cit. on pp. 12, 23).

[64] L. Grünhaupt, M. Spiecker, D. Gusenkova, N. Maleeva, S. T. Skacel, I. Takmakov, F. Valenti, P. Winkel, H. Rotzinger, W. Wernsdorfer, A. V. Ustinov, and I. M. Pop, "Granular aluminium as a superconducting material for high-impedance quantum circuits", Nat. Mater. **18**, 816–819 (2019) (cit. on pp. 12, 13, 21, 23, 42).

[65] M. Pita-Vidal, A. Bargerbos, C.-K. Yang, D. J. Van Woerkom, W. Pfaff, N. Haider, P. Krogstrup, L. P. Kouwenhoven, G. De Lange, and A. Kou, "Gate-tunable field-compatible fluxonium", Phys. Rev. Appl. **14**, 064038 (2020) (cit. on pp. 12, 23).

[66] L. B. Nguyen, G. Koolstra, Y. Kim, A. Morvan, T. Chistolini, S. Singh, K. N. Nesterov, C. Jünger, L. Chen, Z. Pedramrazi, B. K. Mitchell, J. M. Kreikebaum, S. Puri, D. I. Santiago, and I. Siddiqi, "Blueprint for a high-performance fluxonium quantum processor", PRX Quantum **3**, 037001 (2022) (cit. on pp. 12, 23).

[67] M. Peruzzo, F. Hassani, G. Szep, A. Trioni, E. Redchenko, M. Žemlička, and J. M. Fink, "Geometric superinductance qubits: controlling phase delocalization across a single josephson junction", PRX Quantum **2**, 040341 (2021) (cit. on pp. 12, 23).

[68] K. Kalashnikov, W. T. Hsieh, W. Zhang, W.-S. Lu, P. Kamenov, A. Di Paolo, A. Blais, M. E. Gershenson, and M. Bell, "Bifluxon: fluxon-parity-protected superconducting qubit", PRX Quantum **1**, 010307 (2020) (cit. on pp. 12, 23).

[69] P. Brooks, A. Kitaev, and J. Preskill, "Protected gates for superconducting qubits", Phys. Rev. A **87**, 052306 (2013) (cit. on pp. 12, 23).

[70] P. Groszkowski, A. D. Paolo, A. L. Grimsmo, A. Blais, D. I. Schuster, A. A. Houck, and J. Koch, "Coherence properties of the 0- π qubit", New J. Phys. **20**, 043053 (2018) (cit. on pp. 12, 23).

[71] A. Gyenis, P. S. Mundada, A. Di Paolo, T. M. Hazard, X. You, D. I. Schuster, J. Koch, A. Blais, and A. A. Houck, "Experimental realization of a protected superconducting circuit derived from the $0-\pi$ qubit", PRX Quantum **2**, 010339 (2021) (cit. on pp. 12, 23).

[72] R. S. Shaikhaidarov, K. H. Kim, J. W. Dunstan, I. V. Antonov, S. Linzen, M. Ziegler, D. S. Golubev, V. N. Antonov, E. V. Il'ichev, and O. V. Astafiev, "Quantized current steps due to the a.c. coherent quantum phase-slip effect", Nature **608**, 45–49 (2022) (cit. on pp. 12, 23).

[73] N. Crescini, S. Cailleaux, W. Guichard, C. Naud, O. Buisson, K. W. Murch, and N. Roch, "Evidence of dual shapiro steps in a josephson junction array", Nat. Phys. **19**, 851–856 (2023) (cit. on pp. 12, 23).

[74] F. Kaap, C. Kissling, V. Gaydamachenko, L. Grünhaupt, and S. Lotkhov, "Demonstration of dual shapiro steps in small josephson junctions", Nat. Commun. **15**, 8726 (2024) (cit. on pp. 12, 23).

[75] I. V. Pechenezhskiy, R. A. Mencia, L. B. Nguyen, Y.-H. Lin, and V. E. Manucharyan, "The superconducting quasicharge qubit", Nature **585**, 368–371 (2020) (cit. on pp. 13, 34).

[76] C. Jünger, T. Chistolini, L. B. Nguyen, H. Kim, L. Chen, T. Ersevim, W. Livingston, G. Koolstra, D. I. Santiago, and I. Siddiqi, "Implementation of scalable suspended superinductors", Appl. Phys. Lett. **126**, 044003 (2025) (cit. on p. 13).

[77] S. Frasca, I. Arabadzhiev, S. B. De Puechredon, F. Oppliger, V. Jouanny, R. Musio, M. Scigliuzzo, F. Minganti, P. Scarlino, and E. Charbon, "NbN films with high kinetic inductance for high-quality compact superconducting resonators", Phys. Rev. Appl. **20**, 044021 (2023) (cit. on pp. 13, 23).

[78] M. Peruzzo, A. Trioni, F. Hassani, M. Zemlicka, and J. M. Fink, "Surpassing the resistance quantum with a geometric superinductor", Phys. Rev. Appl. **14**, 044055 (2020) (cit. on pp. 13, 34).

[79] M. Medahinne, Y. P. Kandel, S. T. Magar, E. Champion, J. M. Nichol, and M. S. Blok, *Magnetic field tolerant superconducting spiral resonators for circuit QED*, arXiv (2024), 2406.10386 (cit. on p. 13).

[80] M. Pita-Vidal, J. J. Wesdorp, L. J. Splitthoff, A. Bargerbos, Y. Liu, L. P. Kouwenhoven, and C. K. Andersen, "Strong tunable coupling between two distant superconducting spin qubits", Nat. Phys. **20**, 1158–1163 (2024) (cit. on p. 13).

[81] T. W. Larsen, K. D. Petersson, F. Kuemmeth, T. S. Jespersen, P. Krogstrup, J. Nygård, and C. M. Marcus, "Semiconductor-nanowire-based superconducting qubit", Phys. Rev. Lett. **115**, 127001 (2015) (cit. on p. 13).

[82] M. Valentini, F. Peñaranda, A. Hofmann, M. Brauns, R. Hauschild, P. Krogstrup, P. San-Jose, E. Prada, R. Aguado, and G. Katsaros, "Nontopological zero-bias peaks in full-shell nanowires induced by flux-tunable Andreev states", Science **373**, 82–88 (2021) (cit. on p. 13).

[83] F. Luthi, T. Stavenga, O. W. Enzing, A. Bruno, C. Dickel, N. K. Langford, M. A. Rol, T. S. Jespersen, J. Nygård, P. Krogstrup, and L. DiCarlo, "Evolution of nanowire transmon qubits and their coherence in a magnetic field", Phys. Rev. Lett. **120**, 100502 (2018) (cit. on p. 13).

[84] D. Niepce, J. Burnett, and J. Bylander, "High kinetic inductance NbN nanowire superinductors", Phys. Rev. Appl. **11**, 044014 (2019) (cit. on pp. 13, 23).

[85] M. Yang, X. He, W. Gao, J. Chen, Y. Wu, X. Wang, G. Mu, W. Peng, and Z. Lin, "Kinetic inductance compact resonator with nbtin micronwires", AIP Adv. **14**, 10.1063/5.0220296 (2024) (cit. on pp. 13, 23).

[86] A. Shearrow, G. Koolstra, S. J. Whiteley, N. Earnest, P. S. Barry, F. J. Heremans, D. D. Awschalom, E. Shirokoff, and D. I. Schuster, "Atomic layer deposition of titanium nitride for quantum circuits", Appl. Phys. Lett. **113**, 212601 (2018) (cit. on pp. 13, 23).

[87] K. R. Amin, C. Ladner, G. Jourdan, S. Hentz, N. Roch, and J. Renard, "Loss mechanisms in tin high impedance superconducting microwave circuits", Appl. Phys. Lett. **120**, 164001 (2022) (cit. on pp. 13, 23).

[88] M. R. Vissers, J. Gao, D. S. Wisbey, D. A. Hite, C. C. Tsuei, A. D. Corcoles, M. Steffen, and D. P. Pappas, "Low loss superconducting titanium nitride coplanar waveguide resonators", Appl. Phys. Lett. **97**, 232509 (2010) (cit. on pp. 13, 23, 51, 52).

[89] N. Samkharadze, A. Bruno, P. Scarlino, G. Zheng, D. P. DiVincenzo, L. DiCarlo, and L. M. K. Vandersypen, "High-kinetic-inductance superconducting nanowire resonators for circuit QED in a magnetic field", Phys. Rev. Appl. **5**, 044004 (2016) (cit. on pp. 13, 23, 52).

[90] J. G. Kroll, F. Borsoi, K. L. Van Der Enden, W. Uilhoorn, D. De Jong, M. Quintero-Pérez, D. J. Van Woerkom, A. Bruno, S. R. Plissard, D. Car, E. P. A. M. Bakkers, M. C. Cassidy, and L. P. Kouwenhoven, "Magnetic-field-resilient superconducting coplanar-waveguide resonators for hybrid circuit quantum electrodynamics experiments", Phys. Rev. Applied **11**, 064053 (2019) (cit. on pp. 13, 23).

[91] M. Müller, T. Luschmann, A. Faltermeier, S. Weichselbaumer, L. Koch, G. B. P. Huber, H. W. Schumacher, N. Ubbelohde, D. Reifert, T. Scheller, F. Deppe, A. Marx, S. Filipp, M. Althammer, R. Gross, and H. Huebl, "Magnetic field robust high quality factor nbtin superconducting microwave resonators", Mater. Quantum. Technol. **2**, 015002 (2022) (cit. on pp. 13, 23).

[92] O. Dupré, A. Benoît, M. Calvo, A. Catalano, J. Goupy, C. Hoarau, T. Klein, K. L. Calvez, B. Sacépé, A. Monfardini, and F. Levy-Bertrand, "Tunable sub-gap radiation detection with superconducting resonators", Superconductor Science and Technology **30**, 045007 (2017) (cit. on p. 13).

[93] T. Charpentier, D. Perconte, S. Léger, K. R. Amin, F. Blondelle, F. Gay, O. Buisson, L. Ioffe, A. Khvalyuk, I. Poboiko, M. Feigel'man, N. Roch, and B. Sacépé, "First-order quantum breakdown of superconductivity in an amorphous superconductor", Nature Physics **21**, 104–109 (2025) (cit. on p. 13).

[94] H. Rotzinger, S. T. Skacel, M. Pfirrmann, J. N. Voss, J. Münzberg, S. Probst, P. Bushev, M. P. Weides, A. V. Ustinov, and J. E. Mooij, "Aluminium-oxide wires for superconducting high kinetic inductance circuits", Supercond. Sci. Technol. **30**, 025002 (2016) (cit. on pp. 13, 23).

[95] P. Kamenov, W.-S. Lu, K. Kalashnikov, T. DiNapoli, M. T. Bell, and M. E. Gershenson, "Granular aluminum meandered superinductors for quantum circuits", Phys. Rev. Appl. **13**, 054051 (2020) (cit. on pp. 13, 21, 23).

[96] M. Janík, K. Roux, C. B. Espinosa, O. Sagi, A. Baghdadi, T. Adletzberger, S. Calcaterra, M. Botifoll, A. G. Manjón, J. Arbiol, D. Chrastina, G. Isella, I. M. Pop, and G. Katsaros, *Strong charge-photon coupling in planar germanium enabled by granular aluminium superinductors*, arXiv (2024), 2407.03079 (cit. on pp. 13, 23).

[97] V. Gupta, P. Winkel, N. Thakur, P. van Vlaanderen, Y. Wang, S. Ganjam, L. Frunzio, and R. J. Schoelkopf, *Low loss lumped-element inductors made from granular aluminum*, arXiv (2024), 2411.12611 (cit. on pp. 13, 19, 23, 42).

[98] M. Dressel, "Electrodynamics of Metallic Superconductors", Advances in Condensed Matter Physics **2013**, 104379 (2013) (cit. on p. 13).

[99] F. Ioffe and A. R. Regel, "Non-crystalline, amorphous, and liquid electronic semiconductors", Prog. Semicond. **4**, 237–291 (1960) (cit. on p. 13).

[100] R. C. Dynes, J. P. Garno, and J. M. Rowell, "Two-Dimensional Electrical Conductivity in Quench-Condensed Metal Films", Physical Review Letters **40**, 479–482 (1978) (cit. on p. 13).

[101] N. W. Ashcroft and N. D. Mermin, *Solid state physics* (Saunders College Publishing, 1976) (cit. on p. 14).

[102] C. J. Gorter and H. B. G. Casimir, "On supraconductivity i", Physica **1**, 306–320 (1934) (cit. on p. 15).

[103] J. Bardeen, "Two-fluid model of superconductivity", Physical Review Letters **1**, 399–400 (1958) (cit. on p. 15).

[104] D. C. Mattis and J. Bardeen, "Theory of the anomalous skin effect in normal and superconducting metals", Physical Review **111**, 412–417 (1958) (cit. on p. 16).

[105] F. London and H. London, "The electromagnetic equations of the superconductor", Proceedings of the Royal Society of London. Series A, Mathematical and Physical Sciences **149**, 71–88 (1935) (cit. on p. 18).

[106] N. Maleeva, L. Grünhaupt, T. Klein, F. Levy-Bertrand, O. Dupre, M. Calvo, F. Valenti, P. Winkel, F. Friedrich, W. Wernsdorfer, A. V. Ustinov, H. Rotzinger, A. Monfardini, M. V. Fistul, and I. M. Pop, "Circuit quantum electrodynamics of granular aluminum resonators", Nat. Commun. **9**, 3889 (2018) (cit. on pp. 19, 21, 24, 42, 43, 60).

[107] A. Deshpande, J. Pusskeiler, C. Prange, U. Rogge, M. Dressel, and M. Scheffler, "Tuning the superconducting dome in granular aluminum thin films", Journal of Applied Physics **137**, 013902 (2025) (cit. on p. 19).

[108] F. Levy-Bertrand, T. Klein, T. Grenet, O. Dupré, A. Benoît, A. Bideaud, O. Bourrion, M. Calvo, A. Catalano, A. Gomez, J. Goupy, L. Grünhaupt, U. V. Luepke, N. Maleeva, F. Valenti, I. M. Pop, and A. Monfardini, "Electrodynamics of granular aluminum from superconductor to insulator: observation of collective superconducting modes", Phys. Rev. B **99**, 094506 (2019) (cit. on pp. 19, 24, 37).

[109] F. Valenti, F. Henriques, G. Catelani, N. Maleeva, L. Grünhaupt, U. Von Lüpke, S. T. Skacel, P. Winkel, A. Bilmes, A. V. Ustinov, J. Goupy, M. Calvo, A. Benoît, F. Levy-Bertrand, A. Monfardini, and I. M. Pop, "Interplay between kinetic inductance, nonlinearity, and quasiparticle dynamics in granular aluminum microwave kinetic inductance detectors", Phys. Rev. Appl. **11**, 054087 (2019) (cit. on p. 21).

[110] I. Takmakov, P. Winkel, F. Foroughi, L. Planat, D. Gusenkova, M. Spiecker, D. Rieger, L. Grünhaupt, A. Ustinov, W. Wernsdorfer, I. Pop, and N. Roch, "Minimizing the Discrimination Time for Quantum States of an Artificial Atom", Physical Review Applied **15**, 064029 (2021) (cit. on p. 21).

[111] D. J. Parker, M. Savytskyi, W. Vine, A. Laucht, T. Duty, A. Morello, A. L. Grimsmo, and J. J. Pla, "Degenerate Parametric Amplification via Three-Wave Mixing Using Kinetic Inductance", Physical Review Applied **17**, 034064 (2022) (cit. on pp. 21, 51, 52, 60).

[112] M. Xu, R. Cheng, Y. Wu, G. Liu, and H. X. Tang, "Magnetic Field-Resilient Quantum-Limited Parametric Amplifier", PRX Quantum **4**, 010322 (2023) (cit. on pp. 21, 23).

[113] W.-C. Chien, Y.-H. Chang, C. X. Lu, Y.-Y. Ting, C.-S. Wu, S.-D. Lin, and W. Kuo, "Large parametric amplification in kinetic inductance dominant resonators based on 3 nm-thick epitaxial superconductors", Materials for Quantum Technology **3**, 025005 (2023) (cit. on p. 21).

[114] P. Winkel, K. Borisov, L. Grünhaupt, D. Rieger, M. Spiecker, F. Valenti, A. V. Ustinov, W. Wernsdorfer, and I. M. Pop, "Implementation of a Transmon Qubit Using Superconducting Granular Aluminum", Physical Review X **10**, 031032 (2020) (cit. on pp. 21, 24).

[115] K. Borisov, D. Rieger, P. Winkel, F. Henriques, F. Valenti, A. Ionita, M. Wessbecher, M. Spiecker, D. Gusenkova, I. M. Pop, and W. Wernsdorfer, "Superconducting granular aluminum resonators resilient to magnetic fields up to 1 Tesla", Applied Physics Letters **117**, 120502 (2020) (cit. on p. 21).

[116] R. Gao, H.-S. Ku, H. Deng, W. Yu, T. Xia, F. Wu, Z. Song, M. Wang, X. Miao, C. Zhang, Y. Lin, Y. Shi, H.-H. Zhao, and C. Deng, "Ultrahigh kinetic inductance superconducting materials from spinodal decomposition", Adv. Mater. **34**, 2201268 (2022) (cit. on p. 23).

[117] C. Joshi, W. Chen, H. G. LeDuc, P. K. Day, and M. Mirhosseini, "Strong kinetic-inductance kerr nonlinearity with titanium nitride nanowires", Phys. Rev. Applied **18**, 064088 (2022) (cit. on p. 24).

[118] C. Roy, S. Frasca, and P. Scarlino, *Study of Magnetic Field Resilient High Impedance High-Kinetic Inductance Superconducting Resonators*, (Mar. 17, 2025) `http://arxiv.org/abs/2503.13321` (visited on 04/24/2025), pre-published (cit. on p. 24).

[119] Z. K. Minev, I. M. Pop, and M. H. Devoret, "Planar superconducting whispering gallery mode resonators", Appl. Phys. Lett. **103**, 142604 (2013) (cit. on p. 25).

[120] F. Henriques, F. Valenti, T. Charpentier, M. Lagoin, C. Gouriou, M. Martínez, L. Cardani, M. Vignati, L. Grünhaupt, D. Gusenkova, J. Ferrero, S. T. Skacel, W. Wernsdorfer, A. V. Ustinov, G. Catelani, O. Sander, and I. M. Pop, "Phonon traps reduce the quasiparticle density in superconducting circuits", Appl. Phys. Lett. **115**, 212601 (2019) (cit. on pp. 25, 26).

[121] A. Bargerbos, L. J. Splitthoff, M. Pita-Vidal, J. J. Wesdorp, Y. Liu, P. Krogstrup, L. P. Kouwenhoven, C. K. Andersen, and L. Grünhaupt, "Mitigation of quasiparticle loss in superconducting qubits by phonon scattering", Phys. Rev. Appl. **19**, 024014 (2023) (cit. on p. 25).

[122] L. Grünhaupt, U. Von Lüpke, D. Gusenkova, S. T. Skacel, N. Maleeva, S. Schlör, A. Bilmes, H. Rotzinger, A. V. Ustinov, M. Weides, and I. M. Pop, "An argon ion beam milling process for native alox layers enabling coherent superconducting contacts", Appl. Phys. Lett. **111**, 072601 (2017) (cit. on pp. 26, 32).

[123] F. R. Zypman, "Mathematical expression for the capacitance of coplanar strips", J. Electrostat. **101**, 103371 (2019) (cit. on p. 36).

[124] U. S. Pracht, N. Bachar, L. Benfatto, G. Deutscher, E. Farber, M. Dressel, and M. Scheffler, "Enhanced Cooper pairing versus suppressed phase coherence shaping the superconducting dome in coupled aluminum nanograins", Phys. Rev. B **93**, 100503 (2016) (cit. on p. 37).

[125] M. S. Bartlett, “Smoothing periodograms from time-series with continuous spectra”, Nature **161**, 686–687 (1948) (cit. on pp. 40, 63).

[126] M. Kristen, J. N. Voss, M. Wildermuth, H. Rotzinger, and A. V. Ustinov, “Random telegraph fluctuations in granular microwave resonators”, Appl. Phys. Lett. **122**, 202602 (2023) (cit. on p. 40).

[127] L. Grünhaupt, N. Maleeva, S. T. Skacel, M. Calvo, F. Levy-Bertrand, A. V. Ustinov, H. Rotzinger, A. Monfardini, G. Catelani, and I. M. Pop, “Loss mechanisms and quasiparticle dynamics in superconducting microwave resonators made of thin-film granular aluminum”, Phys. Rev. Lett. **121**, 117001 (2018) (cit. on pp. 41, 63).

[128] D. Rieger, S. Günzler, M. Spiecker, A. Nambisan, W. Wernsdorfer, and I. M. Pop, “Fano interference in microwave resonator measurements”, Phys. Rev. Appl. **20**, 014059 (2023) (cit. on pp. 41, 64).

[129] S. Probst, F. B. Song, P. A. Bushev, A. V. Ustinov, and M. Weides, “Efficient and robust analysis of complex scattering data under noise in microwave resonators”, Review of Scientific Instruments **86**, 024706 (2015) (cit. on p. 40).

[130] S. Hunklinger, W. Arnold, S. Stein, R. Nava, and K. Dransfeld, “Saturation of the ultrasonic absorption in vitreous silica at low temperatures”, Phys. Lett. A **42**, 253–255 (1972) (cit. on p. 42).

[131] B. Golding, J. E. Graebner, B. I. Halperin, and R. J. Schutz, “Nonlinear phonon propagation in fused silica below 1 k”, Phys. Rev. Lett. **30**, 223–226 (1973) (cit. on p. 42).

[132] E. M. Levenson-Falk, F. Kos, R. Vijay, L. Glazman, and I. Siddiqi, “Single-quasiparticle trapping in aluminum nanobridge josephson junctions”, Phys. Rev. Lett. **112**, 047002 (2014) (cit. on p. 42).

[133] S. Gustavsson, F. Yan, G. Catelani, J. Bylander, A. Kamal, J. Birenbaum, D. Hover, D. Rosenberg, G. Samach, A. P. Sears, S. J. Weber, J. L. Yoder, J. Clarke, A. J. Kerman, F. Yoshihara, Y. Nakamura, T. P. Orlando, and W. D. Oliver, “Suppressing relaxation in superconducting qubits by quasiparticle pumping”, Science **354**, 1573–1577 (2016) (cit. on p. 42).

[134] S. Geisert, S. Ihssen, P. Winkel, M. Spiecker, M. Fechant, P. Paluch, N. Gosling, N. Zapata, S. Günzler, D. Rieger, D. Bénâtre, T. Reisinger, W. Wernsdorfer, and I. M. Pop, “Pure kinetic inductance coupling for cQED with flux qubits”, Applied Physics Letters **125**, 064002 (2024) (cit. on p. 48).

[135] T. Yamamoto, K. Inomata, M. Watanabe, K. Matsuba, T. Miyazaki, W. D. Oliver, Y. Nakamura, and J. S. Tsai, "Flux-driven Josephson parametric amplifier", Applied Physics Letters **93**, 042510 (2008) (cit. on p. 51).

[136] M. A. Castellanos-Beltran and K. W. Lehnert, "Widely tunable parametric amplifier based on a superconducting quantum interference device array resonator", Applied Physics Letters **91**, 083509 (2007) (cit. on pp. 51, 52).

[137] S. Zhao, S. Withington, and C. N. Thomas, "Nonlinear characteristics of Ti, Nb, and NbN superconducting resonators for parametric amplifiers", Superconductor Science and Technology **36**, 105010 (2023) (cit. on pp. 51, 52).

[138] S. Shu, N. Klimovich, B. H. Eom, A. D. Beyer, R. B. Thakur, H. G. Leduc, and P. K. Day, "Nonlinearity and wide-band parametric amplification in a (Nb,Ti)N microstrip transmission line", Physical Review Research **3**, 023184 (2021) (cit. on pp. 51, 52, 61).

[139] M. Simoen, C. W. S. Chang, P. Krantz, J. Bylander, W. Wustmann, V. Shumeiko, P. Delsing, and C. M. Wilson, "Characterization of a multimode coplanar waveguide parametric amplifier", Journal of Applied Physics **118**, 154501 (2015) (cit. on pp. 51, 52).

[140] M. Malnou, M. Vissers, J. Wheeler, J. Aumentado, J. Hubmayr, J. Ullom, and J. Gao, "Three-Wave Mixing Kinetic Inductance Traveling-Wave Amplifier with Near-Quantum-Limited Noise Performance", PRX Quantum **2**, 010302 (2021) (cit. on pp. 51, 52).

[141] A. B. Zorin, "Josephson Traveling-Wave Parametric Amplifier with Three-Wave Mixing", Physical Review Applied **6**, 034006 (2016) (cit. on p. 51).

[142] M. T. Bell and A. Samolov, "Traveling-Wave Parametric Amplifier Based on a Chain of Coupled Asymmetric SQUIDs", Physical Review Applied **4**, 024014 (2015) (cit. on pp. 51, 52).

[143] C. Macklin, K. O'Brien, D. Hover, M. E. Schwartz, V. Bolkhovsky, X. Zhang, W. D. Oliver, and I. Siddiqi, "A near–quantum-limited Josephson traveling-wave parametric amplifier", Science **350**, 307–310 (2015) (cit. on p. 51).

[144] A. Ranadive, M. Esposito, L. Planat, E. Bonet, C. Naud, O. Buisson, W. Guichard, and N. Roch, "Kerr reversal in Josephson meta-material and traveling wave parametric amplification", Nature Communications **13**, 1737 (2022) (cit. on p. 51).

[145] J. Zhang, T. Li, R. Kokkoniemi, C. Yan, W. Liu, M. Partanen, K. Y. Tan, M. He, L. Ji, L. Grönberg, and M. Möttönen, "Broadband tunable phase shifter for microwaves", AIP Advances **10**, 065128 (2020) (cit. on pp. 51, 52).

[146] M. Zhdanova, I. Pologov, G. Svyatsky, V. Chichkov, and N. Maleeva, "Granular Aluminum Kinetic Inductance Nonlinearity", JETP Letters **119**, 439–443 (2024) (cit. on pp. 51, 52).

[147] R. Kokkoniemi, T. Ollikainen, R. E. Lake, S. Saarenpää, K. Y. Tan, J. I. Kokkala, C. B. Dağ, J. Govenius, and M. Möttönen, "Flux-tunable phase shifter for microwaves", Scientific Reports **7**, 14713 (2017) (cit. on p. 51).

[148] M. J. A. Stoutimore, M. S. Khalil, C. J. Lobb, and K. D. Osborn, "A Josephson junction defect spectrometer for measuring two-level systems", Applied Physics Letters **101**, 062602 (2012) (cit. on p. 51).

[149] J. Luomahaara, V. Vesterinen, L. Grönberg, and J. Hassel, "Kinetic inductance magnetometer", Nature Communications **5**, 4872 (2014) (cit. on pp. 51, 52, 60).

[150] M. Pierre, I.-M. Svensson, S. Raman Sathyamoorthy, G. Johansson, and P. Delsing, "Storage and on-demand release of microwaves using superconducting resonators with tunable coupling", Applied Physics Letters **104**, 232604 (2014) (cit. on p. 51).

[151] A. Palacios-Laloy, F. Nguyen, F. Mallet, P. Bertet, D. Vion, and D. Esteve, "Tunable Resonators for Quantum Circuits", Journal of Low Temperature Physics **151**, 1034–1042 (2008) (cit. on p. 51).

[152] N. Bergeal, F. Schackert, M. Metcalfe, R. Vijay, V. E. Manucharyan, L. Frunzio, D. E. Prober, R. J. Schoelkopf, S. M. Girvin, and M. H. Devoret, "Phase-preserving amplification near the quantum limit with a Josephson ring modulator", Nature **465**, 64–68 (2010) (cit. on p. 51).

[153] M. Sandberg, C. M. Wilson, F. Persson, G. Johansson, V. Shumeiko, T. Bauch, T. Duty, P. Delsing, H.-S. Goan, and Y.-N. Chen, "Fast tuning of superconducting microwave cavities", in AIP Conference Proceedings (2008), pp. 12–21 (cit. on p. 51).

[154] M. Sandberg, C. M. Wilson, F. Persson, T. Bauch, G. Johansson, V. Shumeiko, T. Duty, and P. Delsing, "Tuning the field in a microwave resonator faster than the photon lifetime", Applied Physics Letters **92**, 203501 (2008) (cit. on p. 51).

[155] Z. L. Wang, Y. P. Zhong, L. J. He, H. Wang, J. M. Martinis, A. N. Cleland, and Q. W. Xie, "Quantum state characterization of a fast tunable superconducting resonator", Applied Physics Letters **102**, 163503 (2013) (cit. on p. 51).

[156] B. Abdo, A. Kamal, and M. Devoret, "Nondegenerate three-wave mixing with the Josephson ring modulator", Physical Review B **87**, 014508 (2013) (cit. on p. 51).

[157] A. D. Smith, A. H. Silver, and C. M. Jackson, "Superconducting variable phase shifter using squid's to effect phase shift", U.S. pat. 5153171A (TRW Inc, Oct. 6, 1992) (cit. on p. 51).

[158] K. D. Osborn, J. A. Strong, A. J. Sirois, and R. W. Simmonds, "Frequency-Tunable Josephson Junction Resonator for Quantum Computing", IEEE Transactions on Applied Superconductivity **17**, 166–168 (2007) (cit. on p. 51).

[159] R. Kuzmin, N. Mehta, N. Grabon, and V. E. Manucharyan, "Tuning the inductance of Josephson junction arrays without SQUIDs", Applied Physics Letters **123**, 182602 (2023) (cit. on p. 51).

[160] M. Xu, X. Han, W. Fu, C.-L. Zou, and H. X. Tang, "Frequency-tunable high-Q superconducting resonators via wireless control of nonlinear kinetic inductance", Applied Physics Letters **114**, 192601 (2019) (cit. on p. 52).

[161] J. Li, P. Barry, T. Cecil, M. Lisovenko, V. Yefremenko, G. Wang, S. Kruhlov, G. Karapetrov, and C. Chang, "Flux-coupled tunable superconducting resonator", Physical Review Applied **22**, 014080 (2024) (cit. on pp. 52, 60).

[162] B. Ho Eom, P. K. Day, H. G. LeDuc, and J. Zmuidzinas, "A wideband, low-noise superconducting amplifier with high dynamic range", Nature Physics **8**, 623–627 (2012) (cit. on p. 52).

[163] M. R. Vissers, J. Hubmayr, M. Sandberg, S. Chaudhuri, C. Bockstiegel, and J. Gao, "Frequency-tunable superconducting resonators via nonlinear kinetic inductance", Applied Physics Letters **107**, 062601 (2015) (cit. on pp. 52, 61).

[164] X. Zhang, Z. Zhu, N. Ong, and J. Petta, "High-impedance superconducting resonators and on-chip filters for circuit quantum electrodynamics with semiconductor quantum dots", Phys. Rev. Appl. **21**, 014019 (2024) (cit. on p. 52).

[165] S. Frasca, C. Roy, G. Beaulieu, and P. Scarlino, "Three-wave-mixing quantum-limited kinetic inductance parametric amplifier operating at 6 T near 1 K", Physical Review Applied **21**, 024011 (2024) (cit. on p. 52).

[166] S. E. D. Graaf, A. V. Danilov, A. Adamyan, T. Bauch, and S. E. Kubatkin, "Magnetic field resilient superconducting fractal resonators for coupling to free spins", Journal of Applied Physics **112**, 123905 (2012) (cit. on p. 52).

[167] A. Bienfait, J. J. Pla, Y. Kubo, M. Stern, X. Zhou, C. C. Lo, C. D. Weis, T. Schenkel, M. L. W. Thewalt, D. Vion, D. Esteve, B. Julsgaard, K. Mølmer, J. J. L. Morton, and P. Bertet, "Reaching the quantum limit of sensitivity in electron spin resonance", Nature Nanotechnology **11**, 253–257 (2016) (cit. on p. 52).

[168] S. de Graaf, *Fractal superconducting resonators for the interrogation of two-level systems* (Chalmers University of Technology, Göteborg, 2014), 113 pp. (cit. on pp. 52–54).

[169] D. Loss and D. P. DiVincenzo, "Quantum computation with quantum dots", Physical Review A **57**, 120–126 (1998) (cit. on p. 52).

[170] S. Chaudhuri, D. Li, K. D. Irwin, C. Bockstiegel, J. Hubmayr, J. N. Ullom, M. R. Vissers, and J. Gao, "Broadband parametric amplifiers based on nonlinear kinetic inductance artificial transmission lines", Applied Physics Letters **110**, 152601 (2017) (cit. on p. 52).

[171] L. Ranzani, M. Bal, K. C. Fong, G. Ribeill, X. Wu, J. Long, H.-S. Ku, R. P. Erickson, D. Pappas, and T. A. Ohki, "Kinetic inductance traveling-wave amplifiers for multiplexed qubit readout", Applied Physics Letters **113**, 242602 (2018) (cit. on p. 52).

[172] A. A. Adamyan, S. E. Kubatkin, and A. V. Danilov, "Tunable superconducting microstrip resonators", Applied Physics Letters **108**, 172601 (2016) (cit. on pp. 52, 60).

[173] C. W. Zollitsch, J. O'Sullivan, O. Kennedy, G. Dold, and J. J. L. Morton, "Tuning high-Q superconducting resonators by magnetic field reorientation", AIP Advances **9**, 125225 (2019) (cit. on p. 52).

[174] S. Mahashabde, E. Otto, D. Montemurro, S. De Graaf, S. Kubatkin, and A. Danilov, "Fast Tunable High- Q -Factor Superconducting Microwave Resonators", Physical Review Applied **14**, 044040 (2020) (cit. on pp. 52, 60, 66).

[175] C. Song, T. W. Heitmann, M. P. DeFeo, K. Yu, R. McDermott, M. Neeley, J. M. Martinis, and B. L. T. Plourde, "Microwave response of vortices in superconducting thin films of Re and Al", Physical Review B **79**, 174512 (2009) (cit. on pp. 53, 54).

[176] G. Stan, S. B. Field, and J. M. Martinis, "Critical Field for Complete Vortex Expulsion from Narrow Superconducting Strips", Physical Review Letters **92**, 097003 (2004) (cit. on p. 53).

[177] H. Wang, M. Hofheinz, J. Wenner, M. Ansmann, R. C. Bialczak, M. Lenander, E. Lucero, M. Neeley, A. D. O'Connell, D. Sank, M. Weides, A. N. Cleland, and J. M. Martinis, "Improving the coherence time of superconducting coplanar resonators", Applied Physics Letters **95**, 233508 (2009) (cit. on p. 53).

[178] A. J. Annunziata, "Single-Photon Detection, Kinetic Inductance, and Non-Equilibrium Dynamics in Niobium and Niobium Nitride Superconducting Nanowires", (cit. on p. 56).

[179] S. Anlage, H. Snortland, and M. Beasley, "A current controlled variable delay superconducting transmission line", IEEE Transactions on Magnetics **25**, 1388–1391 (1989) (cit. on p. 58).

[180] A. J. Annunziata, D. F. Santavicca, L. Frunzio, G. Catelani, M. J. Rooks, A. Frydman, and D. E. Prober, "Tunable superconducting nanoinductors", Nanotechnology **21**, 445202 (2010) (cit. on pp. 58, 59).

[181] K. Maki, "The Behavior of Superconducting Thin Films in the Presence of Magnetic Fields and Currents", Progress of Theoretical Physics **31**, 731–741 (1964) (cit. on p. 59).

[182] A. T. Asfaw, A. J. Sigillito, A. M. Tyryshkin, T. Schenkel, and S. A. Lyon, "Multi-frequency spin manipulation using rapidly tunable superconducting coplanar waveguide microresonators", Applied Physics Letters **111**, 032601 (2017) (cit. on p. 61).

[183] D. Niepce, J. J. Burnett, M. G. Latorre, and J. Bylander, "Geometric scaling of two-level-system loss in superconducting resonators", Superconductor Science and Technology **33**, 025013 (2020) (cit. on p. 65).